Nano Vacuum Channel Devices for Electronics and Ultrafast Nanophotonics

by

Marco Turchetti

B.Sc., Polytechnic University of Turin (2014)
M.Sc., Polytechnic University of Turin (2016)
M.Sc., Massachusetts Institute of Technology (2019)

Submitted to the Department of Electrical Engineering and Computer Science
in partial fulfillment of the requirements for the degree of

Doctor of Philosophy

at the

MASSACHUSETTS INSTITUTE OF TECHNOLOGY

May 2022

Author .....
Department of Electrical Engineering and Computer Science
May 13, 2022

Certified by .....
Karl K. Berggren
Professor of Electrical Engineering and Computer Science
Thesis Supervisor

Certified by .....
Phillip D. Keathley
Principal Research Scientist
Thesis Supervisor

Accepted by .....
Leslie A. Kolodziejski
Professor of Electrical Engineering and Computer Science
Chair, Department Committee on Graduate Students

Nano Vacuum Channel Devices for Electronics and Ultrafast Nanophotonics

by

Marco Turchetti

Submitted to the Department of Electrical Engineering and Computer Science
on May 13, 2022, in partial fulfillment of the
requirements for the degree of
Doctor of Philosophy

Abstract

Recent years have seen a surge of interest in nano vacuum channel (NVC) devices due to their low power requirements, radiation hardness, integrability, and ultrafast switching times. Planar NVC devices are ideal candidates for electronics that need to operate in harsh environments such as space. Moreover, recent work, some of which is discussed in this thesis, has demonstrated a rectified, field driven current response from planar NVCs that extends to petahertz-scale frequencies. Such petahertz electronic devices enable field-resolved measurements of ultrafast phenomena and the capability to decode information stored directly on the optical field waveform. In this thesis, state of the art nanotechnology techniques are leveraged to develop a reliable nanofabrication process to pattern planar NVC devices using metallic and refractory materials. Their emission properties in response to both electrical and optical fields are investigated through simulation and testing. Finally, their use for electronics and optoelectronics applications is demonstrated and discussed. In particular, this thesis focuses on their use for building NVC devices for radiation-resistant logic, and for the development of novel optical-field processing techniques such as field sampling to perform time-domain spectroscopy with attosecond resolution. The results from this thesis have direct application in many fields, from metrology to communication to information processing, and represent an important contribution for the development of radiation resistant and petahertz electronics.

Thesis Supervisor: Karl K. Berggren
Title: Professor of Electrical Engineering and Computer Science

Thesis Supervisor: Phillip D. Keathley
Title: Principal Research Scientist

Acknowledgments

This thesis would not have been possible without the help of my mentors, colleagues, family, and friends. In particular, I would like to thank:

My advisors, Prof. Karl Berggren and Dr. Donnie Keathley for their encouragement, guidance and inspiration. Their advice has been invaluable to overcome all the many challenges in my research. It was an honor to work with them.

Prof. Tayo Akinwande and Prof. Luca Daniel for kindly agreeing to be on my thesis committee and giving me great advice about many aspects of my project.

Dr. Mina Bionta for her mentorship and friendship. Her knowledge and input have been fundamental for the success of my work and my growth as a researcher. I truly couldn't have done it without her.

Felix Ritzkowsky for being an amazing collaborator and a friend. His help and advice have been absolutely instrumental for my research.

Dr. Yujia Yang for his help and for sharing his knowledge with me.

All the external collaborators that helped me in this journey. In particular, Prof Franz Kaertner, Prof. William Putnam, Prof. Jim Browning, Dr. Ranajoy Bhattacharya, and Prof. Michael Flatté.

Murat Onen, Navid Abedzadeh and Marco Colangelo for their friendship and constant technical and moral support throughout my whole PhD and beyond. Graduate school wouldn't have been the same without them.

John Simonaitis, Owen Medeiros, Brenden Butters, Alberto Nardi for their advice, discussions and friendship.

Jim Daley and Mark Mondol for their technical assistance. Without them nanofabrication at MIT would stop.

All past and present members of the Quantum Nanostructures and Nanofabrication group for building an amazing place to do research and flourish.

And most importantly, my family, for believing in me and supporting me every step of the way. They made who I am.

Contents

List of Figures

List of Tables

Chapter 1

Introduction

Free-electron devices played an important role in the early days of electronic systems development. In fact, vacuum tubes constituted the main building blocks of the first electronic computers, including Colossus[1], used by the British to decipher German encrypted communication during the WWII, and ENIAC[2], the first general-purpose electronic computer, developed by the US Army to calculate ballistic trajectories. Vacuum tubes were then gradually substituted by semiconductor technology that could deliver faster switching times, lower power consumption, improved scalability, and integrability, and did not require vacuum packaging.[3, 4] The technology survived in a few niche applications. Notably microscopy, high-power electronics such as klystrons, photomultipliers tubes, cathode ray tubes, and a few others.[5, 6, 7] However, in the last few decades, the advancement in nanofabrication techniques allowed for the miniaturization of vacuum free-electron devices,[8] which have started to regain interest due to their interesting properties when shrunk to the nanoscale, especially in terms of speed and low-power operation.

Nano-vacuum channel (NVC) electronics promise fast switching times, and low power-delay product due to reduced turn-on voltages and high velocities. This is achieved thanks to ballistic transport across the channel free of phonon and charged impurity scattering. Also, since free electrons are effectively insensitive to ionizing radiation and temperature fluctuations, these devices are attractive for applications in harsh environments such as space technology [3, 9, 10]. Field-emitter devices

commonly use vertical geometries [11, 12] because with this approach it is easier to achieve sharp nanotips. However, it also makes them difficult to integrate with traditional electronics. On the other hand, planar NVC field-emitters could be easily incorporated into integrated circuits on a large scale. However, these devices are relatively recent and not fully understood in their emission mechanism. Moreover, it is more difficult to ensure they truly have a free-space channel and not leakage or tunneling through the substrate. Fig. 1-1 illustrates the evolution of vacuum devices throughout the years. This thesis focuses on the development of planar nano-vacuum channel devices, their characterization, and applications.

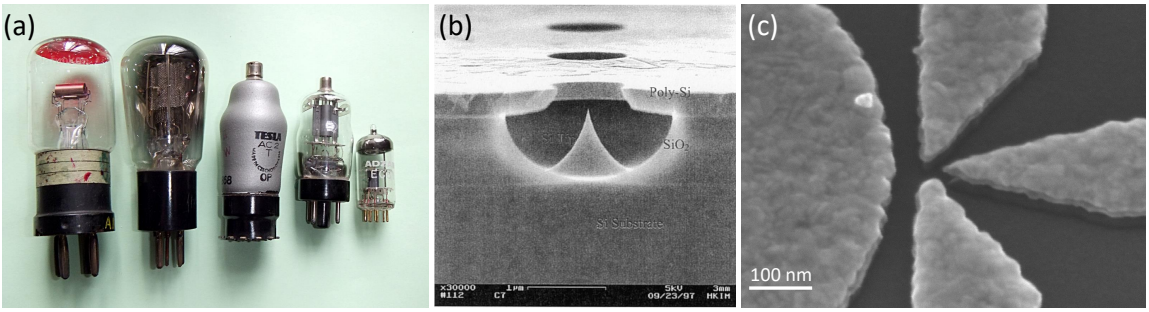

Figure 1-1: (a) Triode vacuum tubes throughout the years[13]. (b) Vertical emitters[12]. (c) planar NVCT from this work.

These planar nano-vacuum channel field-emitters can not only find a great application in radiation-resistant electronics but, thanks to their speed, are also a great candidate for optoelectronic applications. In fact, the free-electron tunneling emission into the channel can be initiated by both electrical and optical fields. While conventional solid-state optoelectronics generally rely on light intensity to be operated, nanomaterials and nanostructured solids could be used to build lightwave-based petahertz electronics[14, 15]. Moreover, nanostructured materials exhibit unique properties in terms of quantum confinement effects[16, 17, 18, 19, 20, 21, 22]. Field confinement and plasmonic effects can also be exploited to achieve strong field enhancements which allow low-power operation[23, 24]. To reach sufficient speed, the devices need to be small enough so that the electron motion happens on an attosecond time scale, and the transport has to be ballistic.[14]

NVC devices' geometry and material have been demonstrated to be tunable so

as to enhance optical field thanks to geometric and plasmonic enhancement. Their emission has also been demonstrated to have sub-cycle sensitivity with respect to the optical field [25, 26, 27]. These characteristics make NVC devices a natural candidate for petahertz-scale processing of optical fields such as lightwave electronics, ultrafast metrology, and time-resolved optical field microscopy.

This thesis addresses the nanofabrication challenges to reliably manufacture planar nano-vacuum channel devices using metallic and refractory materials; the design of useful electronics elements with this technology; the study of the different mechanisms of emission and the electrical and optical properties of NVC both through experimental testing and simulation; the use of NVC devices for electronics a applications; and the use of planar NVC devices use for petahertz-scale optical-field sampling.

This thesis is organized as follows:

Chapter 2 - Fabrication of Metallic and Refractory pNVC devices
In this chapter, the development of a reliable fabrication procedure for both metallic (Au) and refractory (TiN) planar nano vacuum channel devices is described. In particular, the different important obstacles, challenges, solutions, and critical parameters of each step are addressed. This process resulted in the nanofabrication of pNVC bowties, diodes, and transistors with sub-10 nm features.

Chapter 3 - Electrical Simulation of pNVC Devices
In this chapter, the important parameters for the design of devices to be used for NVC logic are explored. The electrical characteristics of these devices are analyzed through electrostatic and particle trajectory boundary element simulation, in order to assess the influence of the most critical geometrical parameters involved in the design of useful and reliable NVC devices. Particular attention was paid to the transistor performance in terms of the optimization of their transcharacteristic.

Chapter 4 - Electrical Characterization

In this chapter, the IV characteristics of planar NVC emitters are studied to extract information on their emission properties. A comparative analysis is conducted on Au and TiN devices in different environmental conditions. The devices are demonstrated to be operable with sub-10 V turn-on voltages and three main regimes of operation are identified: Schottky, Fowler-Nordheim, and saturation. Finally, the testing of a three-terminal gated device to demonstrate the feasibility of transistor-like devices is presented.

Chapter 5 - TDSE Optoelectronic Simulation

In this chapter, the optical-electrical mixed-mode operation of NVC devices is studied through the time-dependent Schrodinger equation simulation of the wavefunction evolution in a NVC nanoantenna. In particular, this work focuses on how the application of an external electrical bias can be leveraged to modify the optical properties of the nanoantenna. It is demonstrated that the DC bias can reduce the threshold of the transition between multiphoton emission to the optical-field-driven tunneling regime, therefore enabling sub-cycle sensitivity of the nanoantenna to an incident optical field, as well as more than 3 orders of magnitude increased photocurrent level, allowing for weak field detection. The influence of several parameters such as work function and field intensity on the photocurrent and background level is also analyzed.

Chapter 6 - PHz Processing of Optical Fields

In this chapter, the use of NVC devices to process petahertz optical fields is experimentally demonstrated. In particular, planar NVC nanoantenna arrays are used to develop a platform for on-chip optical field sampling with attosecond resolution. This detection scheme allows to extract both frequency and phase information from weak optical fields with unprecedented accuracy. In fact, this method is used to perform time-domain spectroscopy of a fJ-level mid-IR pulse, which is 6 orders of magnitude lower than the competing state-of-the-art techniques. More advanced designs are also explored to introduce polarization sensitivity, which is achieved through a meander-

ing configuration of the electrodes and using nanoantennas with different orientations. These NVC nanoantennas are also used to study carrier dynamics in Au such as plasmonic response and hot electrons generation.

Chapter 7 - Conclusion and Outlook

In this chapter, the central findings of this thesis are reviewed and some future avenues to continue the development of this technology are proposed.

Chapter 2

Fabrication of Metallic and Refractory NVC devices

The development of planar nano vacuum channel (NVC) electronic devices requires the development of a process that consistently achieves sub-10-nm feature sizes. We explored two different materials for these devices: Au and TiN. Au has a very strong plasmonic response and a fast carrier recombination so it is very suitable for peta-hertz electronics applications, but it is a very soft material, so not adapt to high-temperature applications. Instead, TiN has slower recombination times[28], so it is less suitable for optical applications that require sub-cycle response times. But on the other hand, it is a refractory material, hence much more resilient to harsh environments, which makes it the perfect candidate for building electronics able to sustain high temperatures or that need to be radiation-resistant. Therefore, two different fabrication techniques were developed for these materials. For the development of these processes the critical requirements are:

1. reduced size of the gap: given that the current is coming from an exponential field emission process, a small gap results in a higher current for the same applied potential, this allows to operate these devices at voltages comparable to common electronics, in opposition to vertical emitters that typically requires tens to hundreds of Volts;

2. large aspect ratio: to maximize the area of emission;

3. small radius of curvature: to maximize the field enhancement, hence decreasing the operating voltage;

4. undercut: to eliminate leakage through the substrate and charging effects resulting in hysteretic behavior;

The patterning process builds on the PMMA-based process developed by Yujia Yang[25]. The patterning of the Au devices is achieved through a lift-off procedure. Instead, the patterning of the TiN is achieved through etching using a hard mask. Each step was carefully characterized using SEM imaging, ellipsometry and reflectometry measurements, and/or feedback from the electrical characterization. In the following, we are going to illustrate the main steps of these fabrication processes.

2.1 Au Devices

This process was developed for Au devices but, in general, it can be extended to the patterning of any metallic material that can be e-beam evaporated.

2.1.1 Device Patterning

The first important step in this process is the patterning of structures having sharp features and very small gaps ($\sim$ 10 nm). This was done with electron beam lithography (EBL). The resist used for this process was 2% polymethyl methacrylate in anysol (PMMA A2), a high-resolution positive resist. Before spinning the resist the substrate should be cleaned from all impurities. This was done with a 5 min sonication in Acetone and then in IPA, followed by an Ashing step to get rid of any organic residue that could affect the result. The resist was then spun at 2.5 krpm for 1 min and then baked for 2 min at 180°C. This resulted in a resist thickness of $\sim$ 80 nm, which was measured with a reflectometer. A thin resist will yield better results in terms of resolution, but since it is going to be used for a lift-off process it needs to be at least $\sim$ 3 times thicker than the evaporated film.

These devices have to be patterned on an insulator to avoid a short circuit between the electrodes. If this is done on a thin oxide, charging due to the electron beam exposing the resist is not an issue because the substrate will carry away excess electrons. However, if this is not the case (i.e. the oxide is thick or the whole substrate is insulating), a conductive layer has to be added on top of the resist to get rid of the charges and avoid overexposure. Different conductive layers were used in this work, all with similar results:

1. spin Espacer™ at 2 krpm (1 min in DI water to remove after EBL);
2. spin Electra92™ at 2 krpm and bake for 2 min at 90°C (1 min in DI water to remove after EBL);
3. spin Discharge™ at 1 krpm (1 min under DI running water to remove after EBL);

The resist is then exposed with an Elionix EBL tool at 125 keV. To get very small gaps the resist is exposed with $\sim 5000\,\mu C/cm^2$, a larger dose than what is typically used with PMMA. If the devices are arrayed over large dense areas, it is appropriate to implement a proximity effect correction (PEC), where the dose is varied depending on the background dose of the surrounding structures in the layout. This correction was implemented in the Elionix exposure software, Beamer, after importing a Monte Carlo simulation of the electron beam interaction volume depending on the substrate stack, which can be performed using Tracer software. The exposure was performed with a current of 2 nA for the critical features and 40 nA for the rest, such as alignment marks and leads.

After exposure the resist is cold developed in a 3:1 IPA:MIBK solution for 1 min at 0 °C and then an adhesion layer of Cr or Ti (2-5 nm) was e-beam evaporated, followed by a 20-25 nm layer of Au. The speed of the evaporation is particularly important because determines the grain size and roughness of the film.[29] Evaporations that are either too fast or too slow can produce larger grain size. The optimal speed was found to be approximately 1 Å/s. Fig 2-1 illustrates the difference between two films evaporated at 0.2 Å/s and 1 Å/s

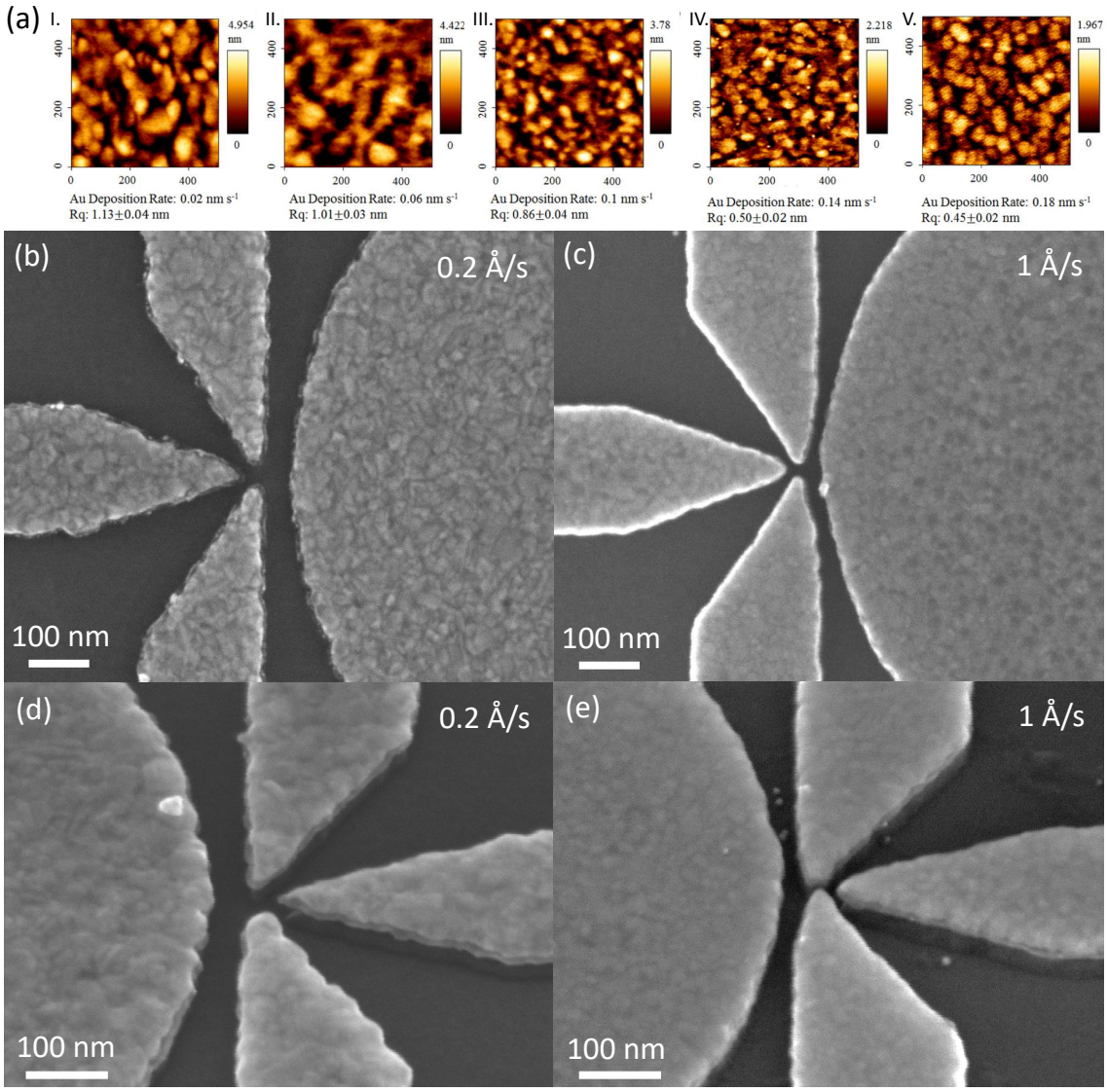

Figure 2-1: Deposition speed optimization. (a) AFM of a Au film deposited at different speeds, showing a smaller root mean square roughness R_q for higher speeds. Figure adapted from Ref. [29]; (b-e)SEM micrographs of planar nano vacuum channel transistors fabricated using 0.2 Å/s (b,d) and 1 Å/s (c,e) evaporation speeds, seen in top view (b,c) and from a 45° angle (d,e).

Finally, the lift-off of the resist is performed by immersing the sample in NMP for 1 h at 70 °C.

Fig 2-2 illustrates an example of different kinds of patterned devices. Fig 2-2a shows a bowtie architecture which should show IV symmetric behavior (i.e. emitter and collector are interchangeable); Fig 2-2b shows a diode design, where the IV char-

acteristic is expected to be rectified due to the asymmetry between the two electrodes; and Fig 2-2c shows a transistor design, which is similar to the diode one but two additional gate electrodes were added to control the potential between the emitter and collector.

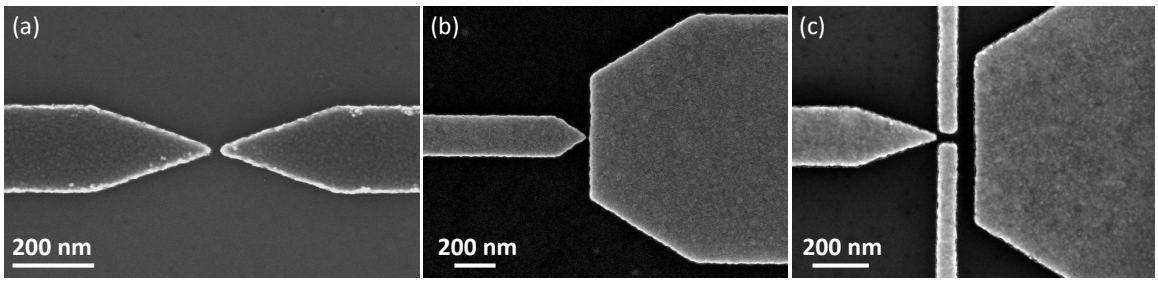

Figure 2-2: SEM micrographs of patterned planar nano vacuum channel devices. (a) bowtie; (b) diode; (c) transistor.

2.1.2 Contacts Photolithography

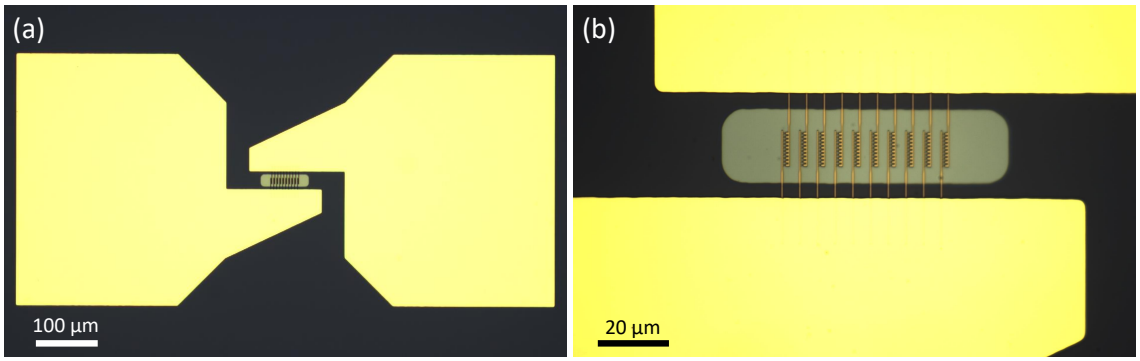

Figure 2-3: Contacts. (a) Optical microscope micrograph of the gold contact pads connected to an array of devices. (b) Enlarged detail illustrating the array region, highlighting the localized etched region.

In order to test the devices, we also need to fabricate pads for wire-bonding to external contacts. This was done using photolithography. To get better features a bilayer process was used.[30] In a bilayer process, the bottom layer is developed faster than the top layer generating an undercut. In a lift-off process, this undercut ensures that the evaporated layer in the developed region is disconnected from that on top of the resist (i.e. there is no contact through the sidewalls), which results in much

cleaner edges. In this process, first, a layer of PMGI SF9 is spun at 4.5 krpm, and baked at 180 °C for 90 s. Subsequently, a layer of S1813 is spun at 4.5krpm and baked 100 °C for 90 s. Then the resist is exposed using a Heidelberg direct-write photolithography system with 7 mW power, 365 nm, and 20% duty cycle laser. Then the resist was developed by immersing the chip for 80 s in CD26 and then for 1 min in DI water. Finally, a 40 nm Cr + 160 nm Au layer was e-beam evaporated and then lifted off by immersion in NMP for $\sim$ 5 h. Fig 2-3 shows a micrograph of patterned pads.

2.1.3 Substrate Etching

During preliminary testing, two-terminal planar nanoemitters exhibited very low current (fA) and hysteretic behavior in their IV characteristic. This behavior was identified to be caused by the charging of the oxide due to some emitted electrons not reaching the collectors and landing on the oxide. The repulsive force due to these electrons prevented further emission of electrons.

To solve this problem, an etch of the oxide around the tip was necessary to form an undercut. This undercut was achieved by introducing two etching steps in the fabrication process: a reactive ion etch (RIE) and a wet etch step. The first, being anisotropic, was used to cut a trench in between the tips. The second, being isotropic, was used to create an undercut, as illustrated in Fig. 2-4.

The reactive ion etching time and power need to be calibrated in order not to damage the gold surface. Gold is a soft material and we have to take into account that even if it is chemically inert it can be easily damaged by ion bombardment during RIE and softened by the temperature increase due to a long process. This is shown in Fig. 2-5, which illustrates the effect of an etching step that destroyed the gold film. The use of intermittent 100W CF4 RIE steps of 1 min and a half (correspondent to 30 nm oxide etching as shown in Table 2.1) with 3 min pauses to cool down the sample, didn't significantly damage the gold for up to 300 nm of etching (the maximum amount tested).

To produce the undercut, HF 7:1 buffered oxide etchant (BOE) was used. How-

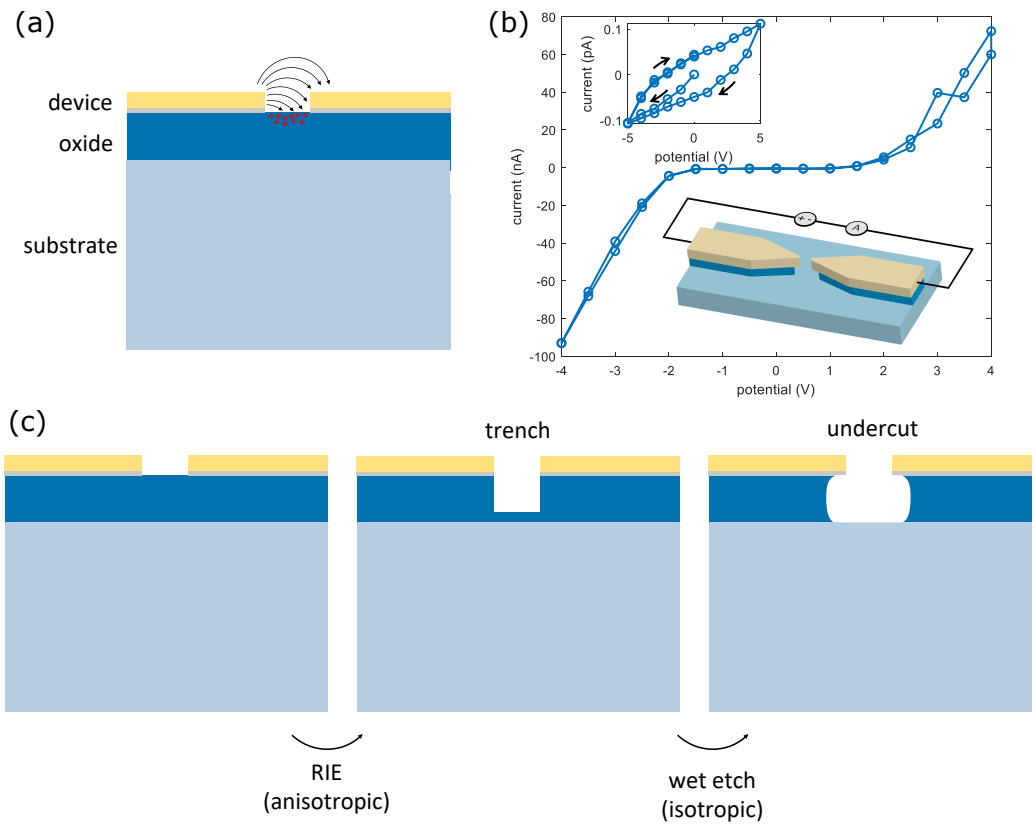

Figure 2-4: Substrate etching and undercut. (a) Schematic showing the trapping of charges in the oxide between the emitter and the collector. (b) IV characteristic of a bowtie device with (main figure) and without (inset) undercut (c) Two-step etching process comprising of an RIE anisotropic step to cut the trench and an isotropic wet etch step to undercut the metal electrodes.

Table 2.1: SiO_2 etch rate using CF_4 RIE

power [W]	etch rate [nm/min]
100	20
150	30
200	40

ever, to create a slower more reproducible process, this was done in a 9:1 DI:BOE solution. A process that is too fast may be difficult to control as illustrated in Fig. 2-6b, showing a collapsed gate due to an undercut that is too deep. The adopted solution provides an etch rate of 20nm/min, as shown in Table 2.2, characterized through reflectometry measurements.

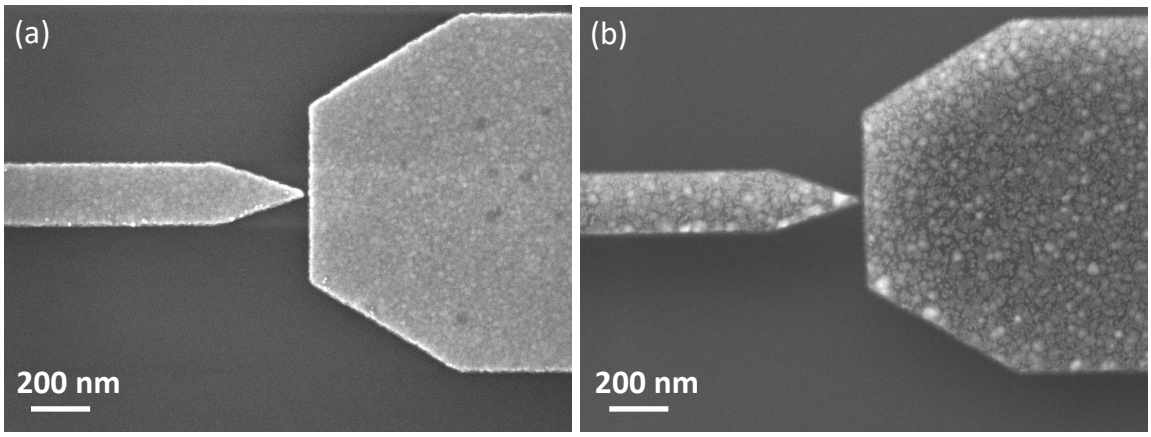

Figure 2-5: Excessive reactive ion etching result. (a-b) SEM micrograph of a diode structure before (a) and after (b) an aggressive RIE step resulting in the damage of the structure.

Table 2.2: SiO_2 etch rate using DOE HF wet etch

concentration [DI:BOE]	etch rate [nm/min]
1:1	60
4:1	30
9:1	20

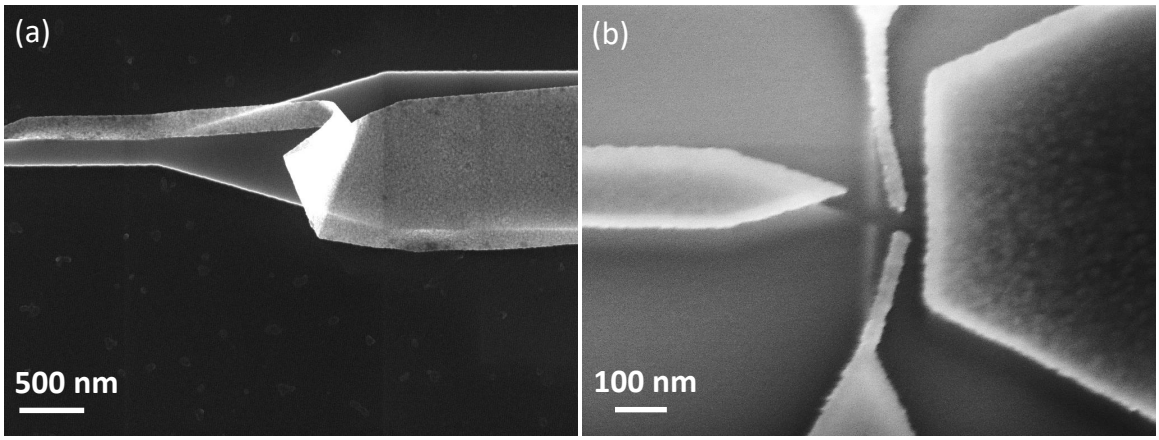

Figure 2-6: Wet etching failures. (a) Delamination of the metal layer due to HF etching of the Ti adhesion layer. To avoid this issue the Ti layer was substituted with a Cr one which is not susceptible to HF. (b) SEM micrograph showing an excessive etching of the substrate underneath the gate electrodes resulting in collapsing of the structures. This can be prevented using a better layout that avoids thin and long features or by decreasing the etching time.

It is also important to notice that the Ti adhesion layer is not compatible with the HF etching, which results in delamination. To avoid this issue the Ti layer was substituted with a Cr one.

Fig. 2-7 illustrates a bowtie structure after RIE and after HF, showing a remarkable 10 nm gap, with the undercut highlighted in the inset.

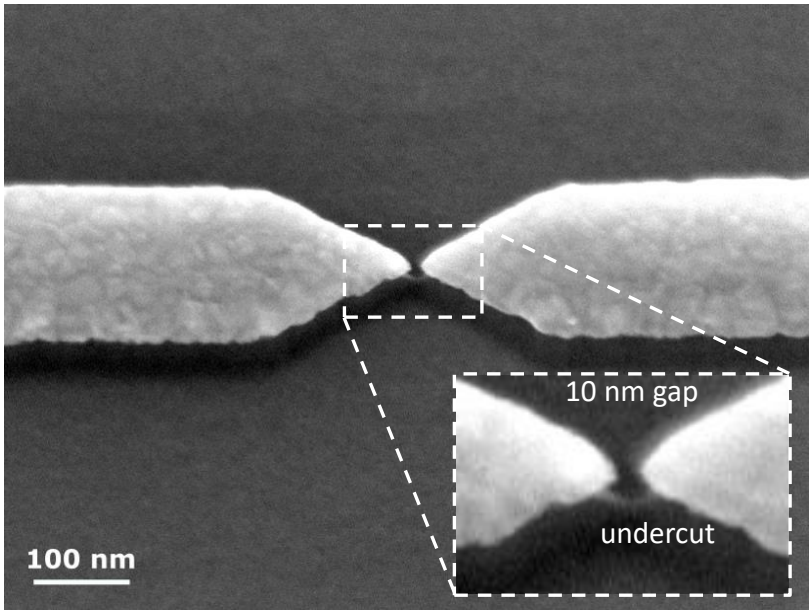

Figure 2-7: SEM micrograph of a Au bowtie with 10 nm gap between emitter and collector electrodes after the HF wet etching. As shown in the inset, this process allows to create an undercut.

2.1.4 Process Flow

Fig 2-8a is a graphical illustration of the different steps of the process which is summarized below :

1. spin of PMMA A2 resist (2.5 krpm and bake for 2 min at 180 °C) on a thermal oxide on Si substrate;

2. EBL patterning of PMMA A2 resist at $\sim 5000\,\mu C/cm^2$: this step is performed to pattern the devices;

3. resist cold development in 3:1 IPA:MIBK at 0 °C for 60 s;

4. e-beam evaporation of 5 nm Cr and 20 nm Au;
5. lift-off in heated NMP at 70 °C for 1h;
6. spin resist bilayer: PMGI SF9 (4.5 krpm, bake at 180 °C for 90s) and S1813 (4.5 krpm, bake at 100 °C for 90s)
7. photolithography of a bilayer PMGI+S1813 resist with Heidelberg MLA100 at 7 mW, 365 nm, and 20% duty cycle : this step is performed to pattern the pads for the electrical connections;
8. resist development for 80 s in CD26, and 60 s in DI water;
9. e-beam evaporation of 40 nm Cr and 160 nm Au
10. lift-off in 5h NMP soak;
11. 1.5 min 100 W CF4 RIE etching;
12. 40 s wet etching in (9:1) DI:BOE HF to create the undercut;

We did some preliminary tests without the last step, but we observed a low current and hysteretic IV characteristics of the devices. We concluded that such an effect was caused by emitted electrons that get trapped in the oxide creating a repulsive potential that prevented further electrons to be emitted. Once the etching step used to create the undercut was introduced the effect disappeared. An example of a completed structure done with this process is shown in Fig. 2-8c.

2.2 TiN Devices

The hardness of TiN is both what makes it an interesting material and what makes it hard to pattern. In the following, I describe the different steps and challenges involved in the development of this nanofabrication process. This process was developed for TiN devices but, in general, it could be adapted to the patterning of many hard materials, modifying the first etching step chemistry.

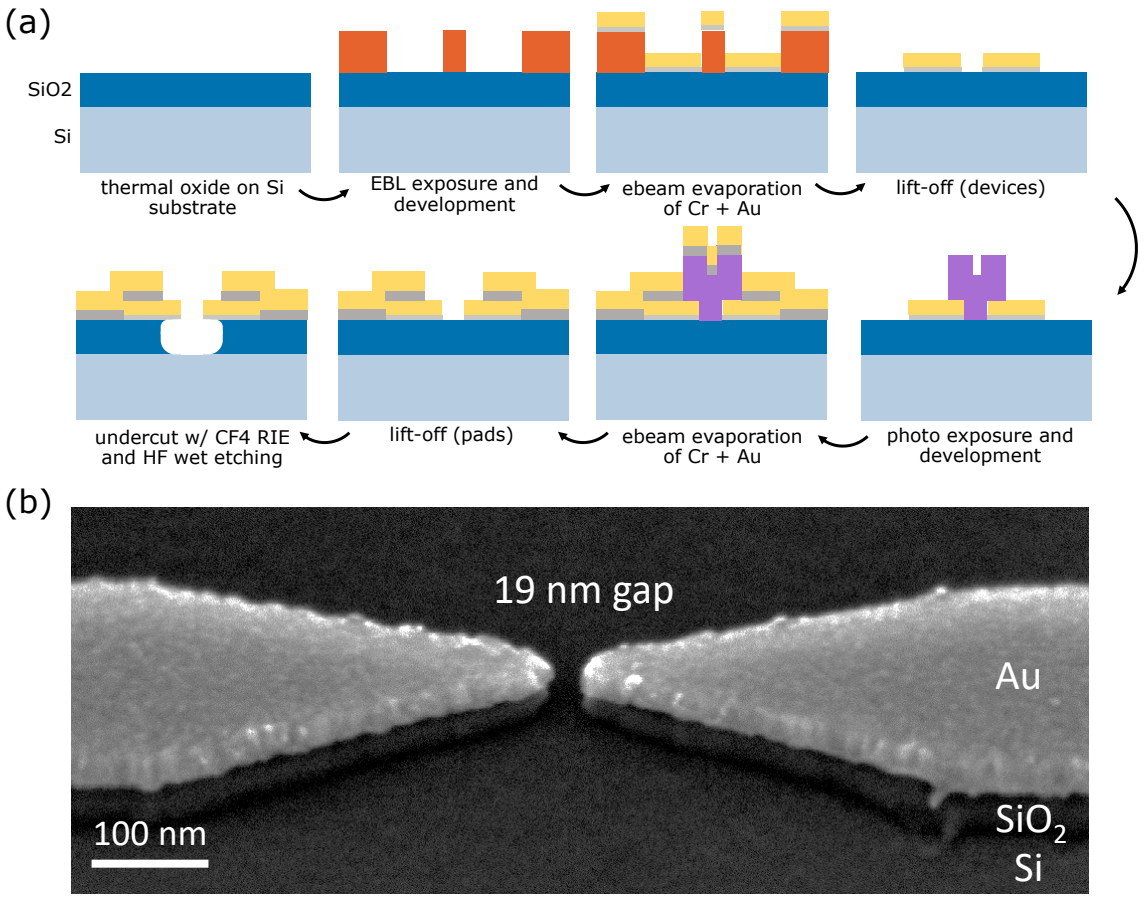

Figure 2-8: Au fabrication. Illustration of the process flow (a) and typical resulting bowtie structure after RIE (b) and wet etching (c) processes.

2.2.1 Device Patterning

In this case, the devices cannot be patterned using a lift-off process since e-beam evaporation is not a viable option to lay down TiN. The TiN film was instead deposited through reactive sputtering of Ti in an argon/nitrogen atmosphere. The deposition was performed using a 300 W power at the Ti target and injecting in the chamber 20 sccm of Ar and 15 sccm of N_2 at a total pressure of 3 mTorr. The patterning was performed by transferring the pattern from a hard mask through an etching step. 50 nm TiN film was used for this process.

The hard mask itself was patterned using a process analogous to the lift-off process described for the Au devices, but with a different material. An exhaustive analysis

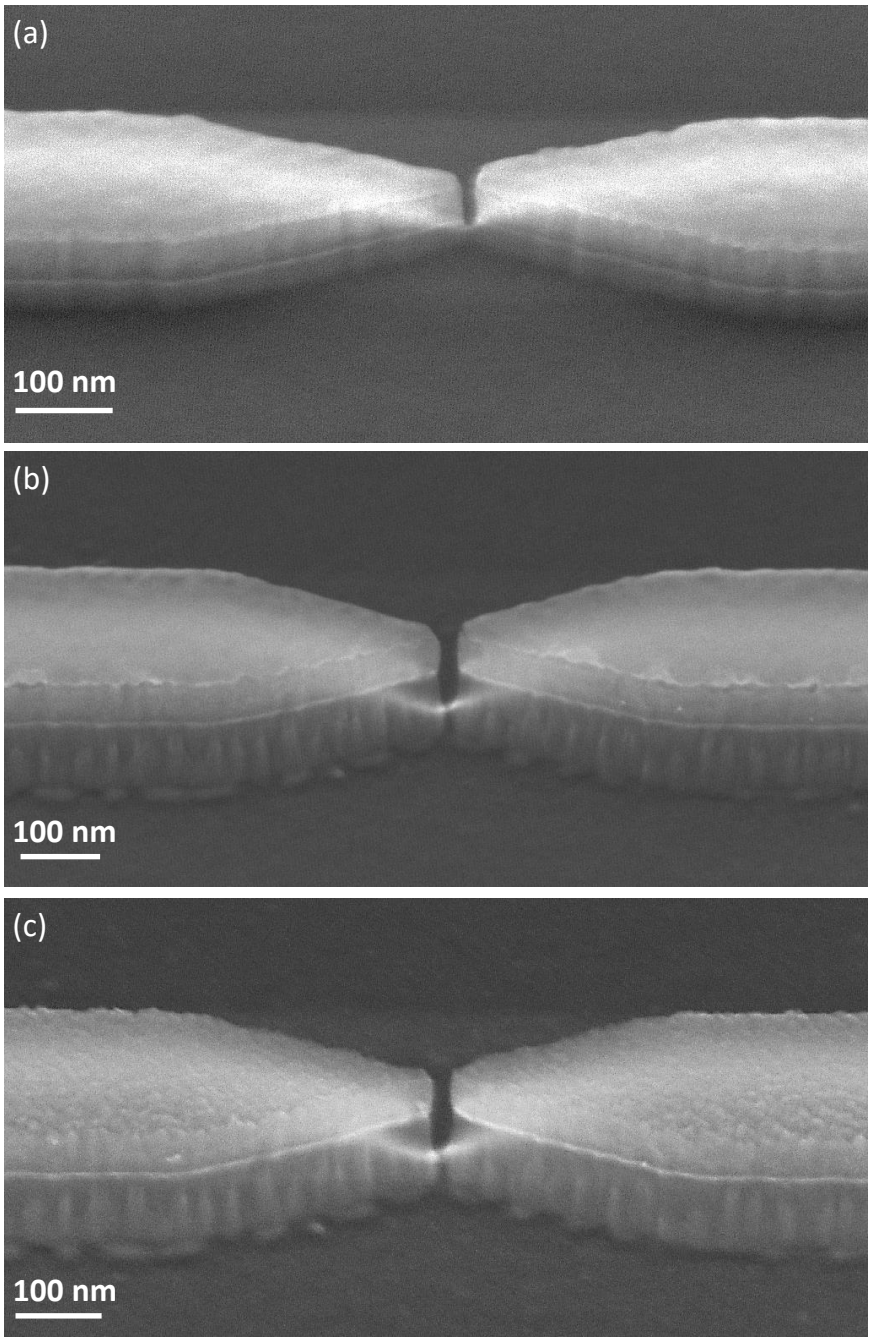

Figure 2-9: TiN device patterning (a) SEM micrograph of a bowtie after device patterning; (b) SEM micrograph of a bowtie after localized etching of the substrate; (c) SEM micrograph of a bowtie after TMAH sonication to remove the hard mask.

of different hard mask materials and etching procedures was performed to develop the process that would give the best performance in terms of gap aspect ratio, edge roughness, and sidewalls steepness after etching. This analysis was carried out to-

gether with Alberto Nardi.[31, 32] The best result was obtained with a bilayer hard mask of 15 nm Al and 15 nm Cr followed by a 100W CF4/O2 9:1 RIE etching, which corresponds to a 5 nm/min etch rate of TiN. The reason why this mask is so effective is that the Cr gives the best performance in the aforementioned metrics but on its own is very hard to remove from TiN (it leaves residues), while Al is too soft to be an effective hard mask but it can be easily removed in TMAH. The bilayer solution exploits the best characteristics of both materials.

The TiN patterning was then performed in 5 steps of 2min RIE, in order to etch down all 50 nm. Fig. 2-9a illustrates an example of this process.

2.2.2 Substrate Etching

The next step is to cut a trench in the substrate to avoid charging, similarly to what was done for the Au devices. However, in this case, there are two important differences:

1. The etching has to be performed with the hard mask on otherwise the RIE would damage the devices while etching the substrate.

2. The etching has to be performed before the photolithography of the contacts, otherwise you wouldn't be able to remove the hard mask afterward.

Hence, the etching has to be localized to the device region, isolating the region where the contacts need to be laid down, otherwise there would be a short between all the electrodes through the substrate.

However, this localized etching cannot be done by employing the same photolithography process explained in the previous section to mask the contact region, because the development in CD26 would damage the hard mask, since CD26 is essentially diluted TMAH. To avoid this issue, a new photolithography process using AZ salty developer was studied. Fig. 2-10 shows the result of different development times on the sidewalls of S1813 resist. A development time of 90 s was found to be optimal.

After development, the trench in the device region was created by RIE analogously to what was described for the Au devices. Following this, the resist was removed first

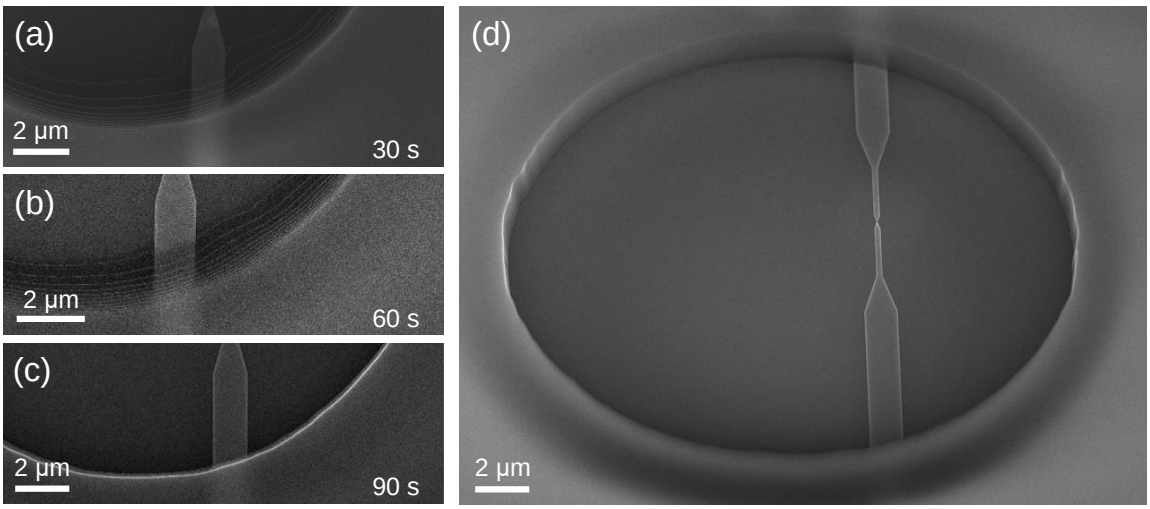

Figure 2-10: Salty development optimization. (a-c) SEM micrographs of the development process immersing the chip in AZ salty developer for different times, namely 30 s, 60 s, and 90 s. It is clear that the 90s development time gives a better result in terms of sidewall steepness. (d) SEM micrographs at an angle of the developed S1813 resist showing the sidewalls' verticality.

with a 70 °C NMP bath for 1h, and then the mask was removed with a 15 min sonication in TMAH. The final steps of laying down the contacts with photolithography followed by wet etching to create the undercut are analogous to the Au devices' process.

2.2.3 Process Flow

Fig 2-11a is a graphical illustration of the different steps of the process, which is summarized below:

1. reactive sputtering of TiN on a thermal oxide on Si substrate;
2. spin of PMMA A2 resist at 2.5 krpm and bake for 2 min at 180 °C;
3. EBL patterning of PMMA A2 resist at $\sim 5000\,\mu C/cm^2$: this step is performed to pattern the hard mask;
4. resist cold development in 3:1 IPA:MIBK at 0 °C for 60 s;
5. e-beam evaporation of bilayer hard mask (15 nm Al and 15 nm Cr);

6. lift-off in heated NMP at 70 °C for 1h;
7. 5×2 min 100 W 9:1 CF4:O2 RIE etching: this step is performed to pattern the devices;
8. spin S1813 (4.5 krpm, bake at 100 °C for 90s)
9. photolithography of a S1813 resist with Heidelberg MLA100 at 7 mW, 365 nm, and 20% duty cycle: this step is performed to pattern the localized etching regions;
10. resist development for 90 s in AZ Developer, and 120 s in DI water;
11. 2×2 min 100 W 9:1 CF4:O2 RIE etching;
12. resist stripping in NMP overnight;
13. mask lift-off through 15 min sonication in TMAH;
14. photolithography of a bilayer PMGI+S1813 resist with Heidelberg MLA100 at 7 mW, 365 nm, and 20% duty cycle: this step is performed to pattern the pads for the electrical connections;
15. resist development in 80 s CD26, and 60 s DI water;
16. e-beam evaporation of 40 nm Cr and 160 nm Au
17. lift-off in 5h NMP soak;
18. 70 s of (9:1) DI:BOE HF to create the undercut.

An example of a completed structure fabricated using this process is shown in Fig. 2-11b.

2.3 Conclusion

In conclusion, nanofabrication processes for metallic (Au) and refractory (TiN) planar nano vacuum channel devices were developed. This chapter focuses on all the

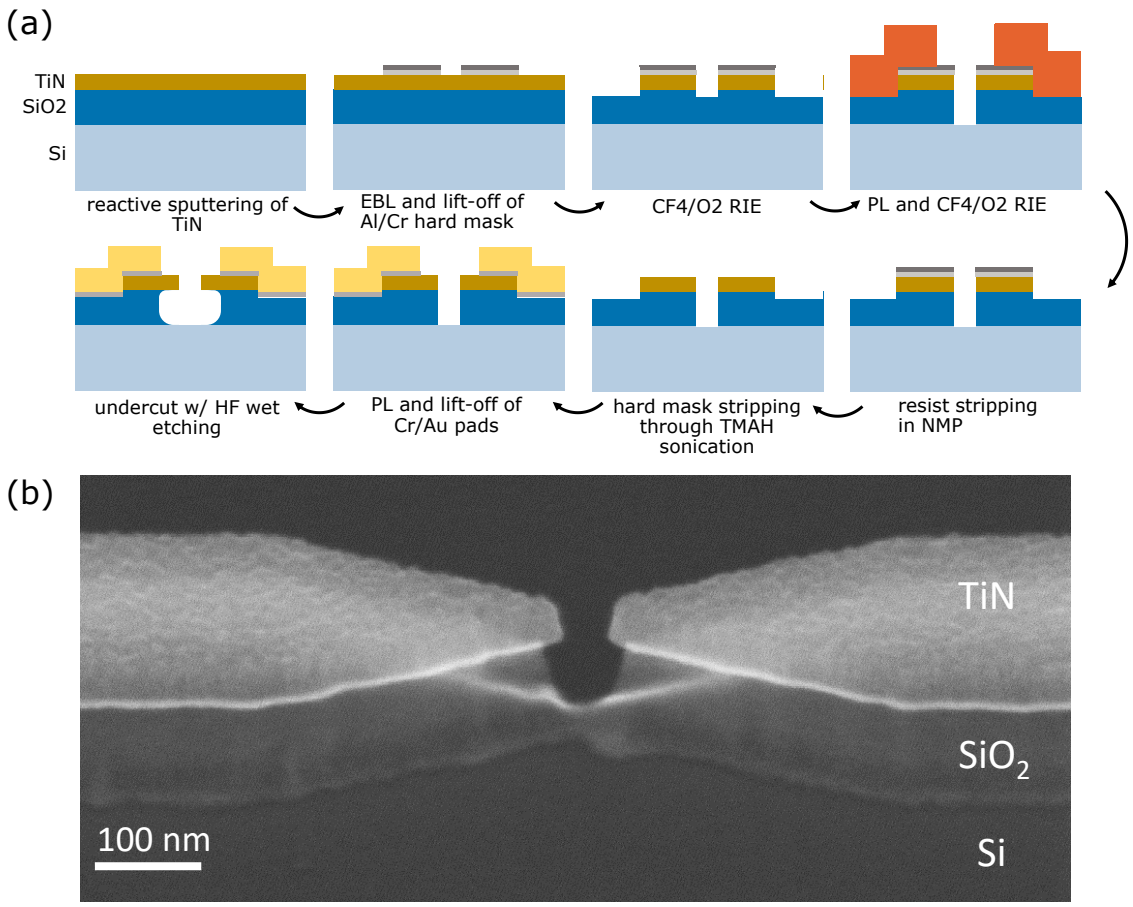

Figure 2-11: TiN fabrication. (a) Illustration of the process flow. (b) Typical resulting bowtie structure.

challenges that had to be addressed during this process development phase, and all the main fabrication parameters and decisions involved. These processes allowed us to reliably obtain sub-10 nm features and represent the fundamental step that all the applications of NVC-based electronics discussed in this thesis are built upon. We are currently expanding upon this work by modifying these processes to introduce a third terminal in an arrayed layout. This requires the development of a VIA process and an aligned deposition of the terminal connections.

Chapter 3

Electrical Simulation of pNVC Devices

To design and build useful electronics using these nano vacuum channel planar devices, it is necessary to understand their emission properties. Knowing how the different geometrical parameters influence these properties is fundamental information to design and optimize the devices. This study was done through the simulation of the IV characteristic of NVC devices. Both two-terminal and three-terminal devices were simulated using Lorentz, a boundary element simulation tool. When two terminals are present the devices behave as a diode, whose symmetry and rectification behavior can be controlled via the geometry. A third terminal can be used as a gate, which can modulate the potential between the other two electrodes (the emitter and the collector) as shown in Fig. 3-1. This can be used to develop transistors, the building block of electronics.

In the following, the simulation of NVC devices is presented, with a focus on the influence of geometrical parameters on the electrical characteristic. These simulations are performed first in 2D which allows for faster optimization, and then in 3D, which allows taking into account the out-of-plane emission.

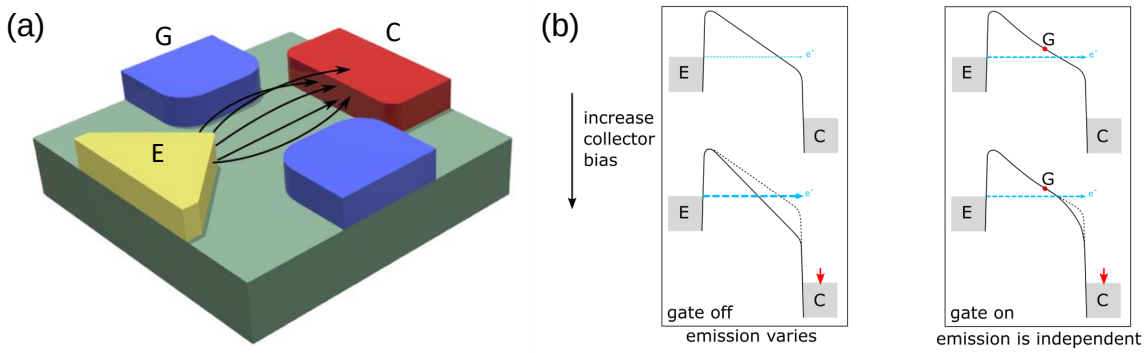

Figure 3-1: Planar nano vacuum channel transistor (pNVCT) concept. (a) Schematic of a pNVCT highlighting the emitter, gate, and collector electrodes, as well as the electron trajectories emitted from the emitter to the collector. (b) Schematic of the potential in the vacuum channel with and without the gate, showing how the gate fixes the potential at the center of the structure making the current from the emitter to the collector ideally independent from the collector potential and being only controlled by the gate potential.

3.1 Two-Dimensional Simulation

As a first approximation, the system can be simulated in 2D, especially for two-terminal devices. Two different device types were simulated in this way: bowtie and diode. A bowtie structure is composed of two electrodes facing each other shaped as tips, which means that the IV characteristic of the system is symmetric. In a diode configuration, on the other hand, one electrode, the emitter is shaped like a tip, while the other, the collector, is flat. This geometrical asymmetry causes a rectified IV response, as shown in Fig. 3-2.

Each system is simulated first by performing an electromagnetic simulation which evaluates the electrical field in the tip region. The field a the tip surface is needed to calculate the current density emitted from the tip, and the field between the emitter and the collector is going to b used to evaluate the trajectory of the emitted charges. The geometry of the device dictates the field enhancement γ which can be defined as the ratio between the calculated field at a certain spot and that which is expected if you had a parallel plate capacitor.

Once the field is calculated, the emitted current density is evaluated using the Fowler-Nordheim rate equation[33]. Fowler-Nordheim emission can be modeled ana-

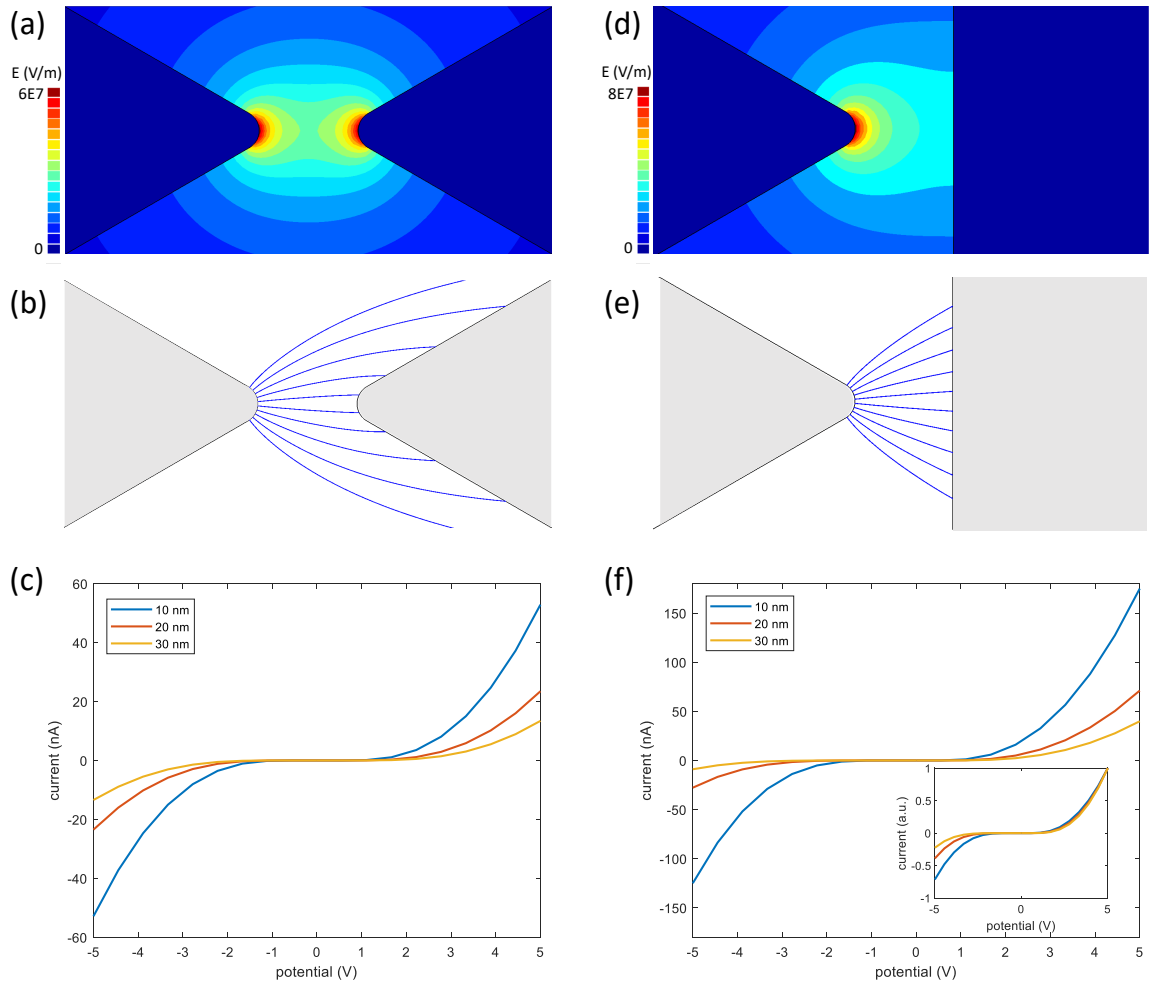

Figure 3-2: Bowtie and diode 2D simulation. (a) Electric field simulation of a bowtie structure, which clearly shows the high electric field regions at the tips. (b) Particle trajectory simulation of a bowtie structure. (c) Simulated IV characteristic of a bowtie, showing the symmetric behavior of the emitted current. (d) Electric field simulation of a diode structure. (e) Particle trajectory simulation of a diode structure. (f) Simulated IV characteristic of a diode, showing the rectified behavior of the emitted current. The inset illustrates the normalized current response, which shows how the more the gap size becomes comparable to the radius of curvature (5 nm), the less rectified the IV characteristic becomes.

lytically as:

$$I \propto \phi^{-1} (\gamma E)^2 \exp\left(-b\frac{\phi^{3/2}}{\gamma E} v(f)\right), \tag{3.1}$$

where $v(f) = 1 - f + (1/6) f \ln(f)$, $f = (q^3/4\pi\epsilon)\phi^{-2}\gamma V/d$, E is the electric field, ϕ is the work function of the material, and $b = 6.83\ eV^{-3/2}Vnm^{-1}$.

Then, for each emitted surface a particle trajectory is performed to evaluate which charges are going to reach the collector. This will be particularly important once we introduce a gate that controls as well as block some of the emission. All the charge densities (in C/m) that reach the collector are then summed and multiplied by the thickness of the device (≈ 20 nm) to get the total current.

Fig. 3-2 illustrates all the different phases of the calculation as well as the resulting IV characteristic. In particular, it is clear from these results that the diode rectified behavior becomes less prominent the smaller the gap becomes. When the gap becomes comparable with the radius of curvature, here taken to be 5 nm, the more the system resembles a parallel plate, hence a symmetric system. A radius of curvature of 5 nm was chosen as this closely approximates the minimum radius of curvature that we can achieve via nanofabrication.

The next step is to add a gate so to create a transistor. In a vertical configuration, this can be done with a circular electrode all around the emitter. In the planar configuration, this can be achieved by adding two fingers in between the emitter and the collector, leaving a gap for the electrons to flow through. These electrodes set the potential in front of the emitter, ideally isolating it from the collector potential, to achieve a current level set only from the gate voltage.

Fig. 3-3b illustrates a typical geometry used to build a planar nano vacuum channel transistor. In particular the different geometrical parameters that influence the performance of the device are highlighted:

1. Emitter-gate gap;
2. Gate thickness;
3. Gate gap width;
4. Emitter semi-angle;
5. Emitter radius;
6. Gate radius;

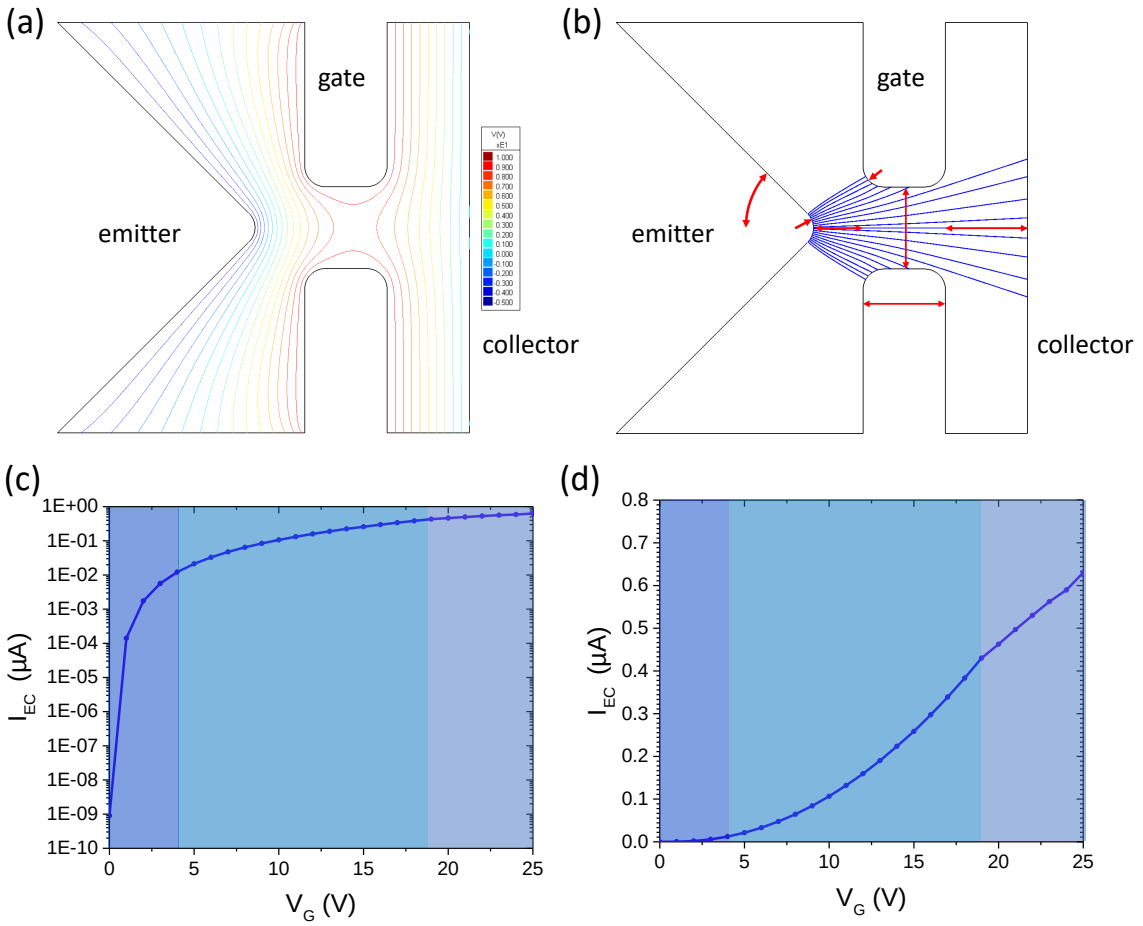

Figure 3-3: pNVC transistor 2D simulation. (a) Electric potential simulation of a pNVCT structure. (b) Particle trajectory simulation of a pNVCT structure, highlighting the different geometrical parameters that influence the device behavior. (c,d) Resulting calculated IV transfer characteristic of a pNVCT, showing three different region of operation.

7. Gate-collector gap;

8. Height.

Analyzing how the collector current depends on the gate voltage reveals 3 regions of operation. The first region is for potentials below the turn-on voltage. Here the field is not sufficient to extract many electrons from the emitter because the bending of the barrier is significantly lower than the work function. The second region is where the devices behave as expected, the gate extracts electrons from the emitter and accelerates them toward the collector. Finally, there is a linear region, where the gate

potential is high enough that even some of the trajectories that are directed toward the collector do not reach it and are instead reverted back to the gate. These regions are highlighted in Fig. 3-3c,d which shows the transistor transfer characteristic.

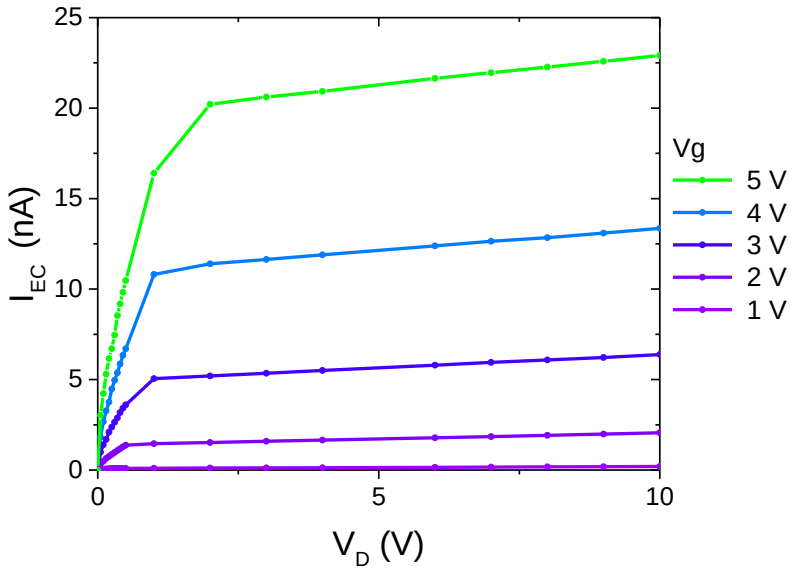

Figure 3-4: 2D simulation of the IV output characteristic of a pNVCT, showing a clear distinction between the ohmic and saturation region.

As can be seen in Fig. 3-4 this device design behaves like a transistor. Different potentials V_G can be effectively used to control the current between the emitter and the collector. The typical ohmic and saturation regions are clearly visible in this graph, which portrays the transistor simulated output characteristic. It is noteworthy, that the saturation region is not perfectly flat as in an ideal transistor, but a small slope is present which suggests that the gate is not fully shielding the gate potential.

Next, the dependence of the output characteristic on several important geometrical parameters was studied. The result of this study is shown in Fig. 3-5. An increase in the gate gap width results in an increase in the current that reaches the collector. However, it also results in a less flat saturation region, which is not ideal. A trade-off is necessary. As expected a smaller radius of curvature results in a higher current. This parameter however is limited by the fabrication procedure and material used. While the gate-collector gap does not influence the current due to the shielding of the gate, the emitter-gate gap is the parameter that influences the most the emitted current.

This is of course due to the exponential dependence of Fowler-Nordheim tunneling emission with the barrier thickness. While a thicker gate improves the saturation due to better shielding, it also decreases the collector current because it has a larger surface to attract electrons. Hence, in this case, a trade-off is also necessary. Finally, a sharper tip (i.e. a smaller semiangle) also increases the emitted current, because it increases the field enhancement due to the lightning rod effect.

3.2 Three-Dimensional Simulation

To develop an accurate model for the electrical characteristics of pNVCTs, we performed field and trajectory simulations of the devices in 3D as well. Because the ballistic trajectories of NVCTs can extend into three dimensions, and are not confined within a material, as shown in Fig. 3-6b. To reliably model the device behavior, a complete three-dimensional field and trajectory simulation is necessary. We performed a comprehensive analysis of the effect of various geometrical parameters and demonstrated how such parameters might be used to improve the devices' design through geometrical optimization. Electron emission and transport in the simulated pNVCTs are controlled by two gate electrodes. The gate potential generates a high field close to the emitter tip which causes electrons to tunnel out from the tip surface. These electrons are transported through the fields surrounding the emitter, gate, and collector before being collected.

The simulations were performed by first solving for the electrical field of the structure and then evaluating the trajectories which were assigned current densities based on a Fowler-Nordheim tunneling model. Fig. 3-6a shows the simulated potential lines for a selected device configuration. Fig. 3-6b instead portrays the simulated electron trajectories for the same device. It is clear from this figure that a significant number of trajectories jump over the gate. While these are not necessarily trajectories that carry a charge density as high as the ones emitted on-plane, we can nevertheless expect a less flat saturation region with respect to the two-dimensional simulation. This assumption is easily confirmed once we plot the output characteristic of the

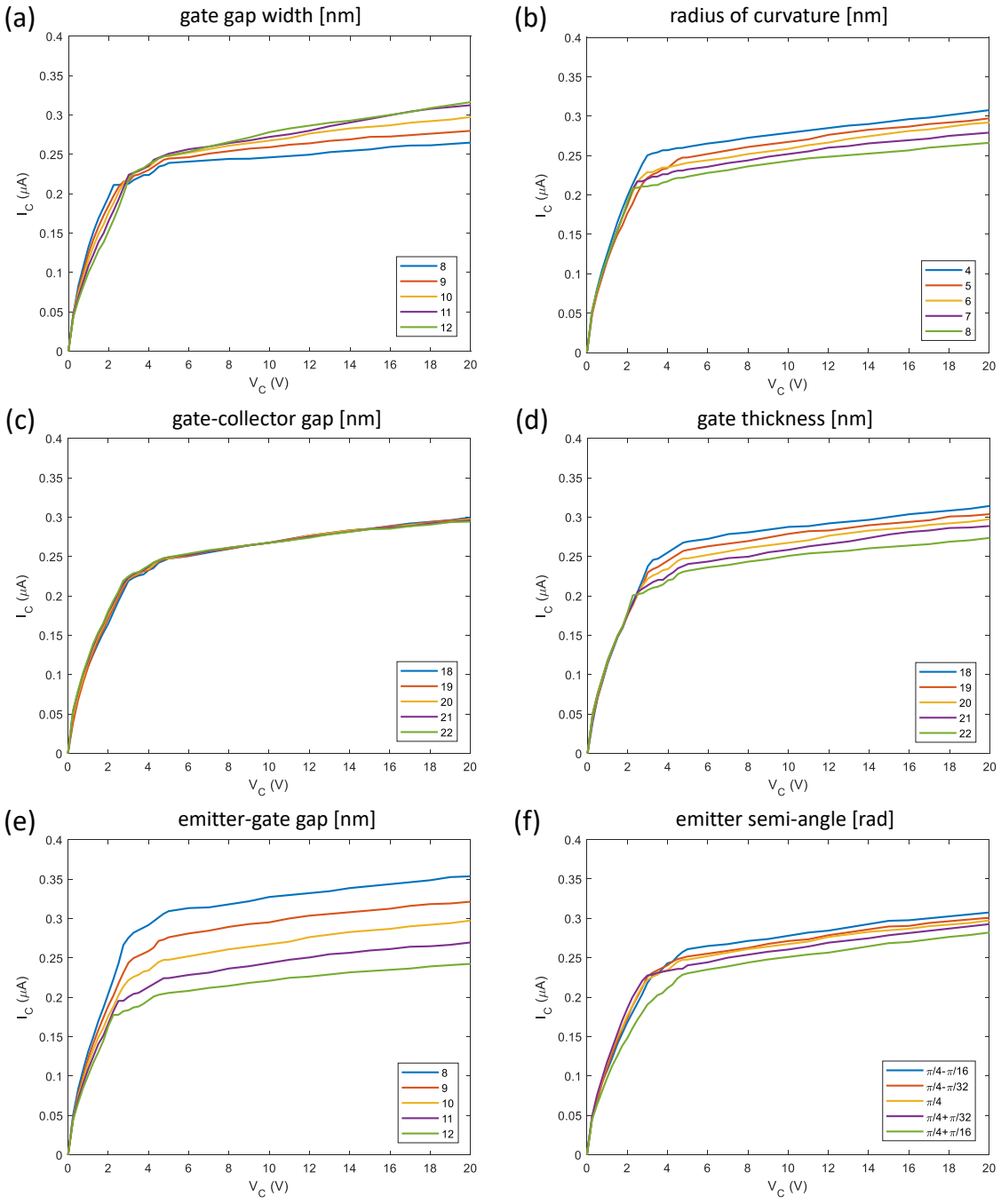

Figure 3-5: 2D Simulation of the IV output characteristic of a pNVCT structure while varying multiple geometrical parameters. In particular gate gap width (a), radius of curvature (b), gate-collector gap (c), gate thickness (d), emitter-gate gap (e), and emitter semi-angle (f). When one parameter is swept, all the other are maintained constant. The reference parameters are emitter-gate gap = 10 nm ; gate thickness = 20 nm; gate gap width = 10 nm; emitter semi-angle = $\pi/4$; emitter radius = 5 nm; gate radius = 5 nm; gate-collector gap = 20 nm; height = 20 nm

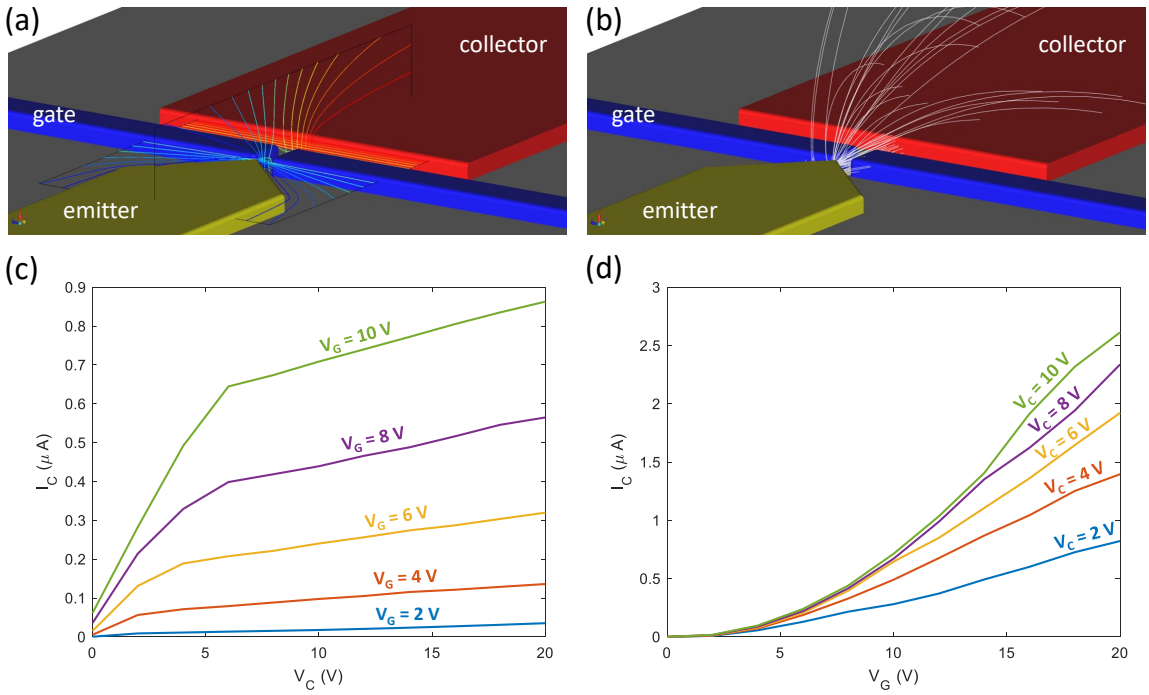

Figure 3-6: 3D Simulation of a pNVCT structure. (a) Electric potential simulation on the horizontal and vertical plane in the active region of the pNVCT (b) Particle trajectory simulation of the electrons emitted toward the collector, assuming a Fowler-Nordheim emission to weight each trajectory with the proper current density. (c) Simulated I-V output characteristics for different gate potentials V_G for this pNVCT configuration, showing transistor behavior. In particular, it is noteworthy that the saturation region is less flat than in the 2D simulation due to electrons jumping over the gate. (d) Simulated transfer characteristic of the pNVCT for different collector potentials V_C.

transistor, shown in Fig. 3-6c. The device still exhibits a clear transistor-like behavior, i.e. a saturation region where the current is gate-controlled with significantly reduced dependence on the collector voltage. However, the slope of the saturation region is significantly higher with respect to the 2D simulation. The overall current is also higher due to the addition of the top and bottom edges of the emitter, which contribute to the emission but which are of course neglected in a 2D simulation.

Fig. 3-7 shows I-V curves obtained for various thicknesses, emitter-gate gaps, and gate width values. As expected, thicker devices correspond to higher currents. However, it is noteworthy to point out that, from a nanofabrication perspective, the thicker the device layer, the worse the resolution is going to be. In fact, it

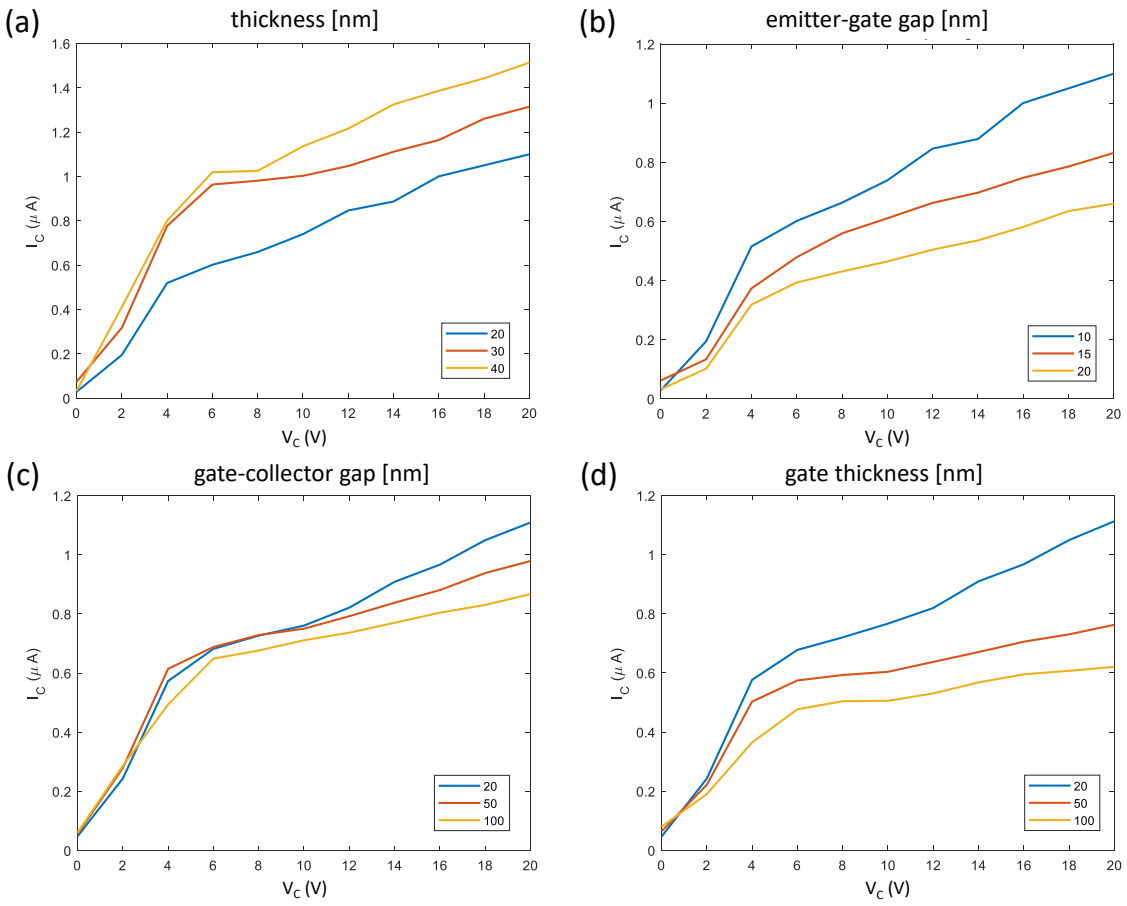

Figure 3-7: 3D Simulation of I-V output characteristics of a pNVCT structure while varying geometrical parameters. In particular the device thickness (a), the emitter-gate gap (b), the gate-collector gap (c), and the gate thickness (d). When one parameter is swept, all the other are maintained constant. The reference parameters are emitter-gate gap = 10 nm ; gate thickness = 20 nm; gate gap width = 10 nm; emitter semi-angle = $\pi/4$; emitter radius = 5 nm; gate radius = 5 nm; gate-collector gap = 20 nm; height = 20 nm

becomes more challenging to pattern small features in thick layers. Similar to the 2D simulation, a smaller emitter-gate gap corresponds to larger currents. Also, a larger gate decreases the current reaching the collector but at the same time results in an improved saturation of I_C. This effect arises because larger gate widths more efficiently shield the collector potential at the cost of increased leakage current to the gate, and is more pronounced in the 3D simulation. Finally, the gate-collector gap that seemed to have no effect in the 2D simulation, plays a significant role when we take into account the real three-dimensional device. It is clear in this case that

a larger gap coincides with a lower current but a flatter saturation region. This happens because when the real thickness of the device is taken into account instead of assuming an infinitely thick device as in the 1D case, some of the fields from the collector leak through the gate influencing the emitted current.

3.3 Conclusion

In this work, the influence of the various distances and thicknesses, structure height, radii of curvature, and tip acuteness, was extensively analyzed to demonstrate how each property affects the I-V characteristic of two- and three-terminal planar NVC devices, providing valuable information to better understand the physics of the device and optimize desired device performance characteristics. This study was instrumental in developing effective designs for planar nano vacuum channel devices. Future work will make use of shape optimization and machine learning algorithms to expand the optimization space beyond parametrization.

Chapter 4

Electrical Characterization

In this chapter, the emission characteristics of planar vacuum nano-diodes having few-nanometer radii of curvature and free-space gaps between the emitter and collector are systematically studied. Most of this work has been submitted for publication. The preprint can be found on arXiv [34].

Free-electron devices played an important role in the early days of electronic systems development. In fact, vacuum tubes constituted the main building blocks of the first electronic computers, including Colossus[1], used by the British to decipher German encrypted communication during WWII, and ENIAC[2], the first general-purpose electronic computer, developed by the US Army to calculate ballistic trajectories. Vacuum tubes were then gradually substituted by semiconductor technology that could deliver faster switching times, lower power consumption, improved scalability, and integrability, and did not require vacuum packaging.[35] The technology survived, but only in a few niche applications where high power is needed.[7, 36, 37, 38] However, in the last few decades, the advancement in nanofabrication techniques have allowed for the miniaturization of vacuum free-electron devices, which have started to regain interest due to their interesting properties when shrunk to the nanoscale, such as high frequency/power output, stability in a harsh environment, integrability and cold emission.[39]

Nano vacuum channel (NVC) electronics promise fast switching times, and a low power-delay product with robust operation in harsh environments [3]. Nanoscale vac-

uum channels allow for true ballistic transport with no phonon and charged impurity scattering, enabling higher electron velocities in the channel. Since these devices do not require vulnerable oxides and free-electrons are effectively insensitive to ionizing radiation and temperature fluctuations, these devices are attractive for applications in harsh environments such as space technology [3, 9]. Field-emission devices commonly use vertical geometries [11, 12, 8, 40] because with this approach it is easier to achieve sharp nanotips. However, it also makes them difficult to integrate with traditional electronics. On the other hand, planar NVC field emitters could be easily incorporated into integrated circuits on a large scale. Moreover, thanks to their small size and low capacitance (down to tens of attofarads), they can be operated at petahertz-scale bandwidths, which makes them an ideal candidate for femtosecond electronics [41] and other optoelectronic applications that require sub-optical-cycle response times [14, 27, 26, 42].

Despite these clear advantages, the underlying emission mechanisms of these devices are poorly understood. In literature, these devices are typically described using a pure Fowler-Nordheim tunneling emission model[43]. While such a model can be used to fit the measured data, to do so requires the use of field enhancement factors of $\gamma > 100$. This stands in stark contrast to electromagnetic modeling of the tips which indicate only modest field enhancement factors of $\gamma \sim 10$ for tips with nanometer-scale radii of curvature and gaps of few to tens of nanometers. For instance, Nirantar et al. [44] had to assume a $\gamma = 590$ to accurately fit their results. Such discrepancies, exceeding more than one order of magnitude, were also noted by De Rose et al. [45], where they had to assume $\gamma = 133$ while their electromagnetic simulation would suggest $\gamma = 3.5$. This implies that these emitters are most likely not operating in the Fowler-Nordheim/Murphy-Good field emission[46] but some other emission mechanism was dominant, unless some other effect is causing the relationship between the emitters' surface field and the measured voltage to be non-linear at low voltages. Understanding the dominant emission mechanisms involved and demonstrating how to reliably determine the proper regime of operation is critical if these devices are going to be used to design and build electronic circuits that operate robustly in extreme

environments.

In this chapter, the emission characteristics of metallic (Au) and refractory (TiN) vacuum-channel bow-tie devices having few-nm radii of curvature and sub-20-nm air/vacuum gaps were compared. This comparison is of interest as Au devices have high electrical conductivity while being chemically inert, which makes them great candidates for operation in a variety of environments, including operation in ambient conditions, but the TiN devices are more resilient, allowing us to reach higher peak field strength and current densities from the emitters and thus transition to different emission regimes, as well as being able to be operated at higher temperatures.

These vacuum nano-diodes were shown to be able to be operated reliably with turn-on voltages of < 10 V and from nA to μA-level operating currents per device. Repeatable behavior over many devices and over several scans per device was demonstrated. The measured IV characteristics were analyzed under variable temperature and atmospheric pressure to reveal the dominant mechanisms responsible for electron emission, and to rule out substrate conduction. In particular, three distinct emission regimes were isolated from single devices for the first time: Schottky, Fowler-Nordheim field emission, and saturation, which we attribute to Child-Langmuir space-charge effects. The transition between these regimes is still under scrutiny from a theoretical perspective, where some important effort has been done to build a model that would encompass all three[47]. The result was fitted with analytical models to better understand these behaviors ensuring that the field enhancement factor reasonably matches that from electromagnetic simulations.

Additionally, the lifetime characterization of Au devices was performed in collaboration with colleagues at Boise State University demonstrating the long-term stability of these devices. Finally, preliminary testing on three-terminal planar nano vacuum channel transistors (pNVCT) was performed demonstrating the successful use of a gate to modulate the collector current.

4.1 Electrical Characterization of the Emission

To analyze the emission behavior of these planar vacuum nanoemitters both metallic (Au) and refractory (TiN) planar nano vacuum channel (pNVC) bow-tie devices having 10-20 nm vacuum gaps were fabricated using the procedures laid out in Chapter 2. Typical examples of the resulting structures are illustrated in the scanning electron microscope (SEM) micrographs shown in Fig. 4-1a and Fig. 4-1b. Particularly important was the implementation of an undercut in the fabrication process. In fact, preliminary testing showed that, without this undercut, the device often showed hysteretic behavior, which we attribute to the charging of the insulating layer underneath the devices. The introduction of an undercut reliably eliminated this effect. An example of the effect of the undercut can be seen in Fig. 4-1c where an I-V curve of a metallic emitter was measured with (main figure) and without (inset) the undercut. Moreover, an undercut allows us to ensure that the measured current is all due to emission in the vacuum gap and there is not a significant contribution due to substrate conduction, for example, Frenkel-Poole emission[48, 49], which can skew the analysis. To make sure there was no appreciable leakage through other pathways the substrate current was monitored as well, which was more than 2 orders of magnitude lower than the collector current. Moreover, as will be discussed in more detail later on, there is a strong pressure dependence on the emission, which demonstrates that the emission is indeed in the vacuum gap. Additionally, the devices were never imaged before testing since the SEM electron beam causes the deposition of a carbon layer, and this was observed to contribute to ohmic conduction. For imaging purposes, a twin device was always fabricated next to each device.

After the fabrication, the I-V response of tens of devices fabricated was analyzed to investigate the underlying emission mechanisms. The testing was performed in a vacuum chamber with a pressure of 10^{-6} mbar using a Keysight B2912A SMU. Fig. 4-2a shows an example of experimental data for a gold bowtie nano emitters having a gap of < 20 nm. The device current exhibited an exponential behavior with respect to the applied field with a turn-on voltage of approximately 5V which is consistent

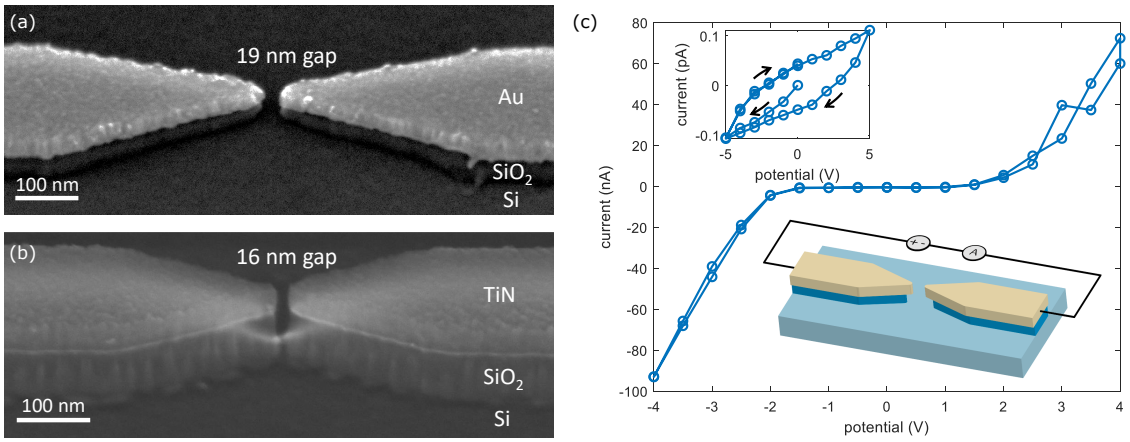

Figure 4-1: (a) SEM micrograph of a typical Au device. (b) SEM micrograph of a typical TiN device. We note that the thicknesses of the devices are different: the Au device is 25 nm thick while the TiN one is 50 nm thick. The radius of curvature is typically of the order of 5-10 nm and the tip semi-angle is 26°. (c) Schematic of an IV measurement (bottom-right inset) and I-V curve of a metallic emitter with (main figure) and without (top-left inset) an undercut. As can be seen from the inset, without the undercut the current is very low and hysteresis is present. With the undercut, the current is orders of magnitude higher and the hysteresis disappears.

with the Au work function of 5.1eV.

The inset shows the same curve plotted in a $log(I)$ vs $V^{1/2}$ plot, which is useful for identifying emission in the Schottky regime. The Schottky emission regime applies to field-enhanced thermionic emission. In the Schottky emission regime, the applied field reduces the work function barrier height, and enhances the thermionic emission. Schottky emission can be modeled as [50, 51]:

$$I \propto T^2 \exp\left(\frac{q}{2k_B T}\sqrt{\frac{q\gamma V}{d\pi\epsilon_0}}\right), \tag{4.1}$$

where γ is the field enhancement factor, T is the temperature, ϵ_0 is the vacuum permittivity, q is the elementary positive charge, k_B is the Boltzmann constant, V is the voltage across the gap between the tips, and d is the gap between the tips. Schottky emission therefore would appear linear with a positive slope when plotting $log(I)$ vs $V^{1/2}$. As such, we refer to these plots as "Schottky plots" for simplicity throughout the remainder of this work. We can see that the tested gold device exhibits a linear characteristic in this plot over the entire range of bias voltages

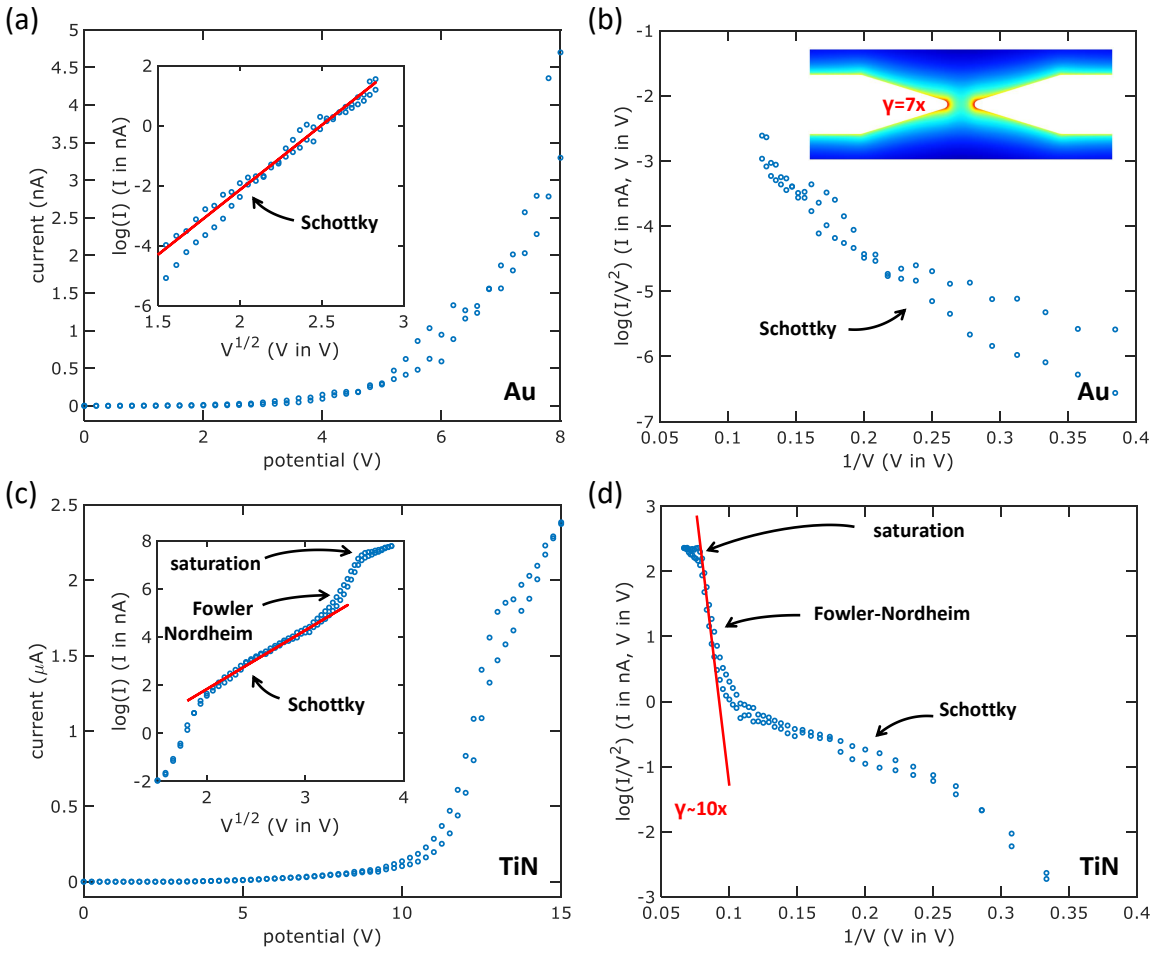

Figure 4-2: Typical behavior of an IV sweep of a Au (a,b) and a TiN (c,d) device. (a) Au experimental results with inset $log(I)$ vs $V^{1/2}$ plot, which highlights Schottky emission. We can see that the Au device exhibits Schottky behavior in this test, which can be identified by a linear dependence in the inset. (b) Au experimental results in $log(I/V^2)$ vs $1/V$ plot, which highlights Fowler-Nordheim emission. Inset illustrates a 3D electromagnetic simulation showing the field enhancement factor (γ) in the region around the two tips, highlighting a $\gamma = 7$ at the edge of the tip. From these data, to fit a Fowler-Nordheim emission we would need to assume a $\gamma = 50$, which is inconsistent with simulation.(c) TiN device experimental results with inset Schottky plot. In this plot, we can identify a Schottky regime that manifests as a linear dependence in the inset. This is followed by a superlinear regime and then saturation. (d) TiN experimental results in Fowler-Nordheim plot. Here, we can identify that the superlinear regime that was visible in the Schottky plot is indeed driven by Fowler-Nordheim emission. In fact, this region can be fitted with a FN model, assuming a $\gamma = 10$, which is consistent with the simulation. These tests were performed at 10^{-6} mbar.

tested, indicating that Schottky emission could be dominant.

To ensure our interpretation is correct, emission due to Fowler-Nordheim tunneling was also considered. The Fowler-Nordheim regime applies to cold-field-emission where the electrons tunnel through the work-function barrier from the Fermi surface of the material, and is the most commonly used theory for modeling field-induced electron emission in literature. Fowler-Nordheim emission can be modeled analytically as:

$$I \propto \phi^{-1} \left(\gamma \frac{V}{d}\right)^2 \exp\left(-b \frac{d\phi^{3/2}}{\gamma V} v(y)\right), \tag{4.2}$$

where $v(y) = 1 - y^2 - y^2 \log(y)/3$, $y = 2\sqrt{\frac{e^2 \gamma V}{16 d \pi \epsilon_0}} \frac{1}{\phi}$, ϕ work function and $b = 6.83$ $eV^{-3/2} V nm^{-1}$. For the Fowler-Nordheim (FN) fit we used a more complete version of this formula, which can be found in Kyritsakis e al. [52]:

$$I \propto \phi^{-1} \left(\gamma \frac{V}{d}\right)^2 \left(t(y) + \frac{d\phi}{e\gamma V R} \psi(y)\right) \exp\left(-b \frac{d\phi^{3/2}}{\gamma V} \left(v(y) + \frac{d\phi}{e\gamma V R} \omega(y)\right)\right), \tag{4.3}$$

where:

$$\begin{cases} t(y) = 1 + y^2/9 - y^2 \ln(y)/11 \\ \psi(y) = 4/3 - y^2/500 - y^2 \ln(y)/15 \\ v(y) = 1 - y^2 - y^2 \ln(y)/3 \\ \omega(y) = 4/5 - 7y^2/40 - y^2 \ln(y)/100 \end{cases} \tag{4.4}$$

and $y = 2\sqrt{\frac{e^2 \gamma V}{16 d \pi \epsilon_0}} \frac{1}{\phi}$, with R radius of curvature, ϕ work function and $b = 6.83$ $eV^{-3/2} V nm^{-1}$.

Fig. 4-2b illustrates the same data as in 4-2a, but now plotted in a Fowler-Nordheim plot ($log(I/V^2)$ vs $1/V$). In such a plot, FN emission would appear linear with a negative slope. While a linear trend with a negative slope does indicate field-emission as likely, it, unfortunately, does not guarantee that Fowler-Nordheim-like tunneling is truly dominant. We note that Schottky emission can also appear quasi-linear when plotted in this fashion over a given bias voltage range. Indeed, this is the case with the data from our gold devices. However, when the curve is

fit with a FN model, $\gamma = 50$ has to be assumed, which is not consistent with the electromagnetic simulation results. Electromagnetic simulations consistently predict $\gamma \sim 10$. An example of such a simulation illustrating γ around the two tips is shown in the inset of Fig. 4-2b, which shows a peak of $\gamma \approx 7$. Taken together with the Schottky plot, this provides strong evidence that across the tested bias range Schottky emission dominated from the gold devices. This is further confirmed with temperature testing which is described below. Unfortunately, the device could not be run at higher potentials to determine if there was a point where Fowler-Nordheim emission appears dominant due to degradation of the devices. This may be due to reshaping of the tips due to high current density or modification of the work function due to current-assisted adsorption on the tips. This latter phenomenon is less commonly discussed in the nanoemitter community where current-assisted desorption is more prevalent, especially when the devices are operated in a high vacuum. However, it is well known to the electron microscopy and field deposition communities, since the electron beam induces deposition of molecules on the sample[53, 54]. We believe the two phenomena may be competing, with net desorption or adsorption resulting depending on the environment.

Before concluding that this emission is in the Schottky regime other possible explanations have to be considered. In literature, low current emission has also been associated with Frenkel-Poole emission[55]. However, in our case, this can be excluded since when monitoring the substrate current of devices with a fully etched insulating layer, no appreciable current contribution was measured. Another possible explanation would be an unaccounted resistance path[43]. This can be excluded because this path would be present also in the case of non-etched devices and in the case of devices with larger gaps (where such resistors would just scale linearly so they would be easily detectable). In both these situations, no appreciable current was measured. This emission behavior could also be due to space-charge effects[56**?**]. However, if this was the case, there would not be a temperature dependence of the current, which, as will be discussed later on, is indeed present in these devices. Whilst not totally excluding the possibility of alternative explanations, the most plausible explanation

of the observed results is that at low voltages the emitter is operating in the Schottky emission regime.

To investigate what impact the emitter material might have on the emission properties, similar testing on the TiN devices was then performed. Thanks to their more resilient nature and a thicker oxide, the TiN devices can be run at higher fields and current densities, which allowed to unveil transitions between different emission regimes as can be seen in Figs. 4-2c and d. At low voltage (approximately from 4 V to 10 V) you can observe what appears to be Schottky emission behavior (see linear response over this range in the Schottky plot shown in the inset of Fig. 4-2c). Unlike the gold devices, at higher potentials (between 10V and 13V) you can see a transition away from Schottky emission where the emission grows at an even higher exponential rate. Fig. 4-2d illustrates the same data in a Fowler-Nordheim plot. In this case, the slope is considerably steeper than the slope for Au for bias voltages between 10 to 13 V. Indeed, the data in this region can be fitted using the aforementioned FN model, which predicts $\gamma \approx 10$, which is physically consistent with the $\gamma \approx 7$ obtained from our electromagnetic simulations. Finally, above 13V the current reaches a saturation region. It is worth noting that this behavior is repeatable in forward and backward scans so it is not due to damage to the devices. We attribute this saturation behavior to space-charge effects [57, 58, 59, 60, 61].

To further investigate our findings, the temperature dependence of the devices' IV response was then tested. Such tests should clearly differentiate between Schottky and Fowler-Nordheim emission as Schottky emission depends strongly on temperature, while Fowler-Nordheim emission does not. The temperature tests were done by placing a heating stage inside the vacuum chamber in thermal contact with the sample. The apparatus used for the test is depicted in Fig. 4-3. This apparatus includes a vacuum chamber to control the pressure, a heating stage (1st stage), a heat sink stage (2nd stage), high-temperature PCBs for the electrical connection, roughing and turbo-molecular pumps, a UV lamp to induce water desorption, a nitrogen line for venting, a thermocouple for temperature feedback, and a source measuring unit (SMU) for performing the electrical characterization.

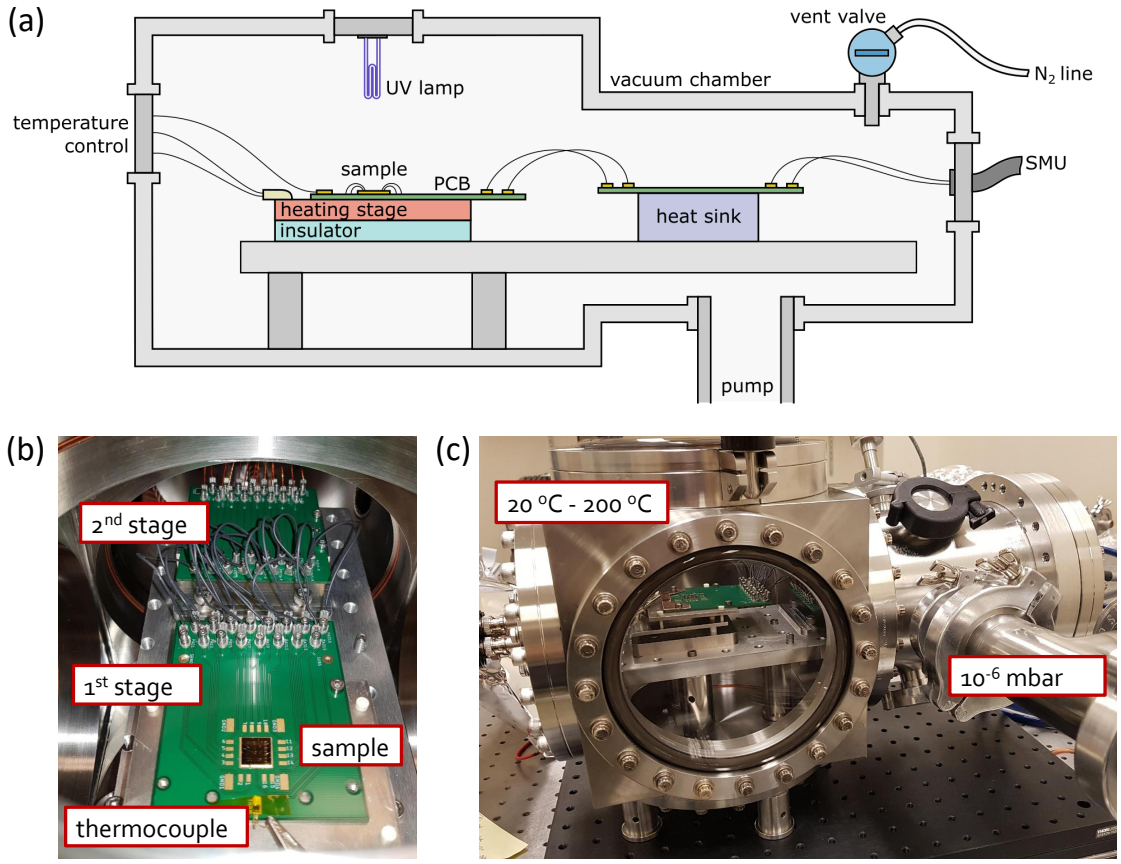

Figure 4-3: Testing Apparatus. (a) Schematic of the apparatus. This apparatus includes a vacuum chamber to control the pressure, a heating stage (1st stage), a heat sink stage (2nd stage), high-temperature PCBs for the electrical connection, roughing and turbo-molecular pumps, a UV lamp to induce water desorption, a nitrogen line for venting, a thermocouple for temperature feedback, and a source measuring unit (SMU) for performing the electrical characterization. (b) Picture of the 2 stages with the sample glued on the high-temperature PCB. (c) Picture of the vacuum chamber used for the testing.

The results of this test are shown in Fig. 4-4 for both Au and TiN devices. The Au devices (Fig. 4-4a) exhibit a clear temperature dependence over the entire range of applied voltages. Each scan appears in the Schottky plot as a series of spaced, roughly linear traces consistent with the expected behavior for Schottky emission. In this regime, the temperature provides the necessary energy to overcome the barrier set by the work function and applied bias voltage.

On the other hand, for the TiN devices, all three regimes are clearly visible. In the Schottky regime, which dominates at the lowest voltages, there is a temperature

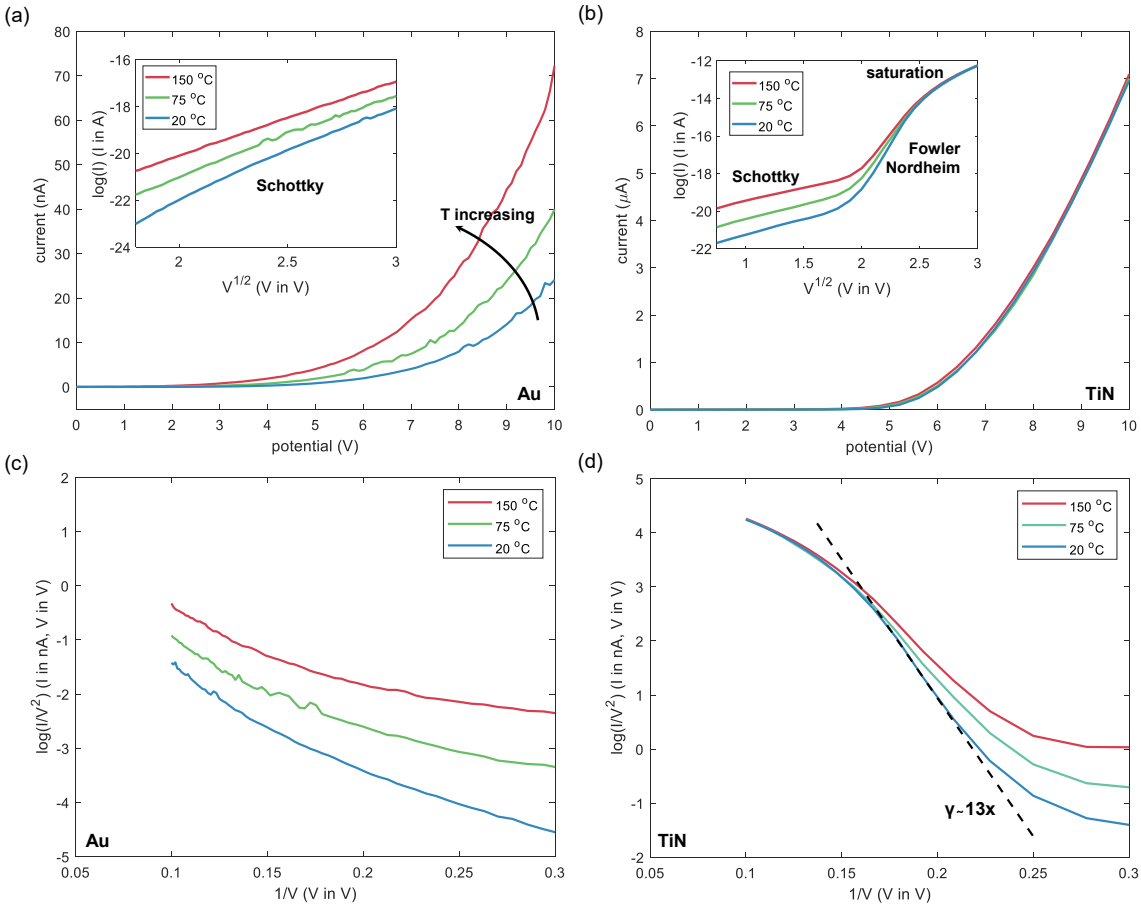

Figure 4-4: Temperature dependence of Au (a) and TiN (b) devices. The devices' IV characteristics are recorded while varying the device temperature using a heater placed in thermal contact with the sample. The insets illustrate the same data plotted in a $log(I)$ vs $V^{1/2}$ axes. The Au devices exhibit Schottky behavior which manifests as parallel traces in this plot. On the other hand TiN devices exhibit all three regimes (Schottky, Fowler-Nordheim, and saturation). While Schottky regime shows temperature dependence similarly to the Au devices, Fowler-Nordheim does not which is consistent with the model. The saturation regime also does not show any temperature dependence. It is worth noticing that in this case the TiN device transitions to the Fowler-Nordheim regime and then to saturation at a lower voltage than the Au device. This can be due to different gap sizes or a sharper tip: both parameters can vary with slightly different fabrication conditions. The same Au and TiN data is plotted in a FN plot in (c) and (d) respectively.

dependence which manifests as vertically-spaced parallel traces in the Schottky plot in the inset of Fig. 3-7b. This dependence gradually shrinks and then disappears when Fowler-Nordheim tunneling begins to dominate at higher voltages. This reduction in temperature dependence is consistent with cold field emission, where tunneling

from near the Fermi level dominates. Finally, we also observe no temperature dependence in the saturation regime. This is consistent with space-charge effect induced saturation that does not depend on temperature or material properties.

When the same data is plotted on a FN graph (Fig. 4-4c,d), you can see that the TiN device reaches Fowler-Nordheim regime approaching the $\gamma \approx 13$ curve (fitted using the 20°C data) and then saturates due to space-charge effects.

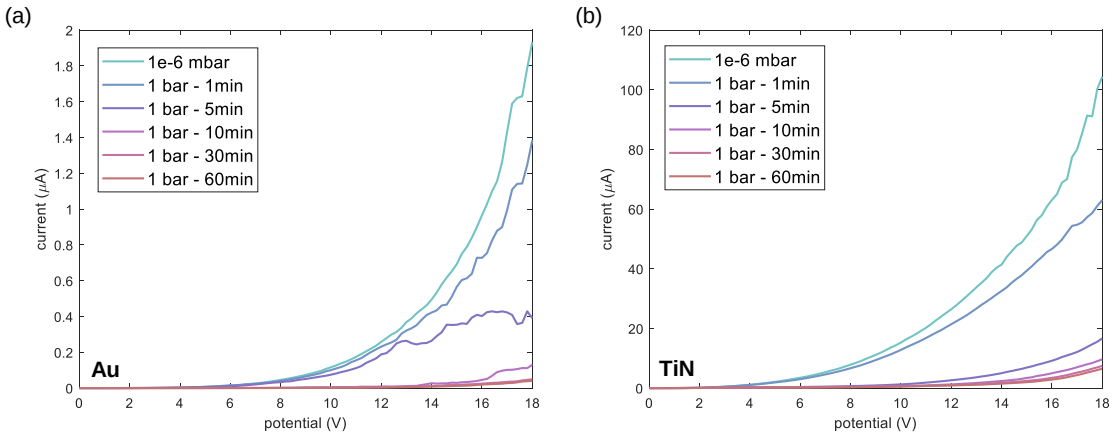

Figure 4-5: Pressure dependence of Au (a) and TiN (b) devices. The devices are first tested in a vacuum chamber with a 10^{-6} mbar vacuum. Then the chamber is vented with air and a series of consecutive traces are recorded at different time intervals: 1, 5, 10, 30, and 60 min. The drop in current is due to adsorption on the tip surface and shows that the conduction is indeed in the vacuum channel with no significant contribution due to substrate conduction, which would not be affected by the pressure.

The influence of ambient air pressure on the devices was also investigated. To do this, the devices were initially tested at 1e-6 mbar and then the chamber was vented and the IV characteristic was recorded at different intervals after exposure to ambient pressure. The sub-20nm gaps ensure that even in ambient pressure the conduction through the emitter to collector gap happens in an effective vacuum, not mediated by the gas. This is because the air molecules' mean free path at atmospheric pressure is larger than the gap size. However, as can be seen in Fig. 4-5, when exposed to the atmosphere, these devices, nonetheless experience a strong reduction in current. The current stabilizes after about an hour to a level much lower than that in vacuum conditions, both for the metallic and refractory devices. We attribute this effect to

the adsorption of molecules (e.g. water) on the tips which modify the work function at the emission surfaces.[62] In the case of TiN devices oxidation might also play a role. In both cases, the vacuum emission characteristics can be fully recovered after a few burn-in cycles (i.e. running a few IV sweeps that clean the emission surface from adsorbed molecules) once they are placed back in vacuum. This effect cannot be attributed to the variation of cooling time at different pressures because is unaffected by whether the IV sweeps are performed in close succession or at different times. It is also noteworthy that the current drop experienced by the refractory devices when exposed to atmospheric pressure is less dramatic than that experienced by the metallic devices. Indeed, the refractory device in Fig. 4-5 experiences a current drop of 16×, while the gold device experiences a current drop of 50×. These findings further confirm the ballistic nature of the electron emission and transport through the vacuum channel as a contribution to the conduction due to leakage through the substrate would not exhibit such strong sensitivity to air exposure.

4.2 Lifetime Testing

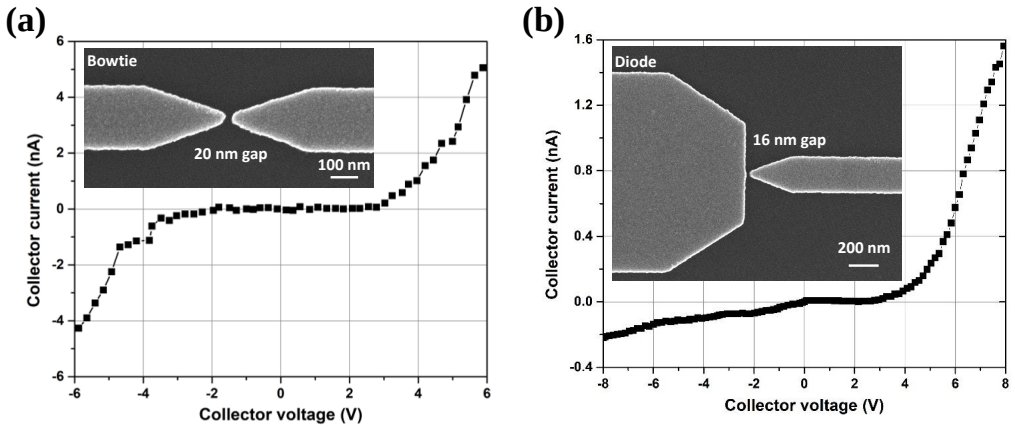

Figure 4-6: Bowtie and Diode IV Characteristic. (a) IV characteristic of one of the lifetime-tested Au bowtie devices showcasing its symmetric behavior. The inset is an SEM micrograph of a typical bowtie. (b) IV characteristic of one of the lifetime-tested Au diode devices showcasing its rectified behavior. The inset is an SEM micrograph of a typical diode.[63]

A characterization of the lifetime of the two-terminal Au devices was also per-

formed in collaboration with Boise State University, in particular with Dr. Ranajoy Bhattacharya and Prof. Jim Browning.[63] Boise is equipped for long-term testing. Therefore, after preliminary characterization at MIT, the devices were sent to Boise state for lifetime testing and then back to MIT for post-test imaging.

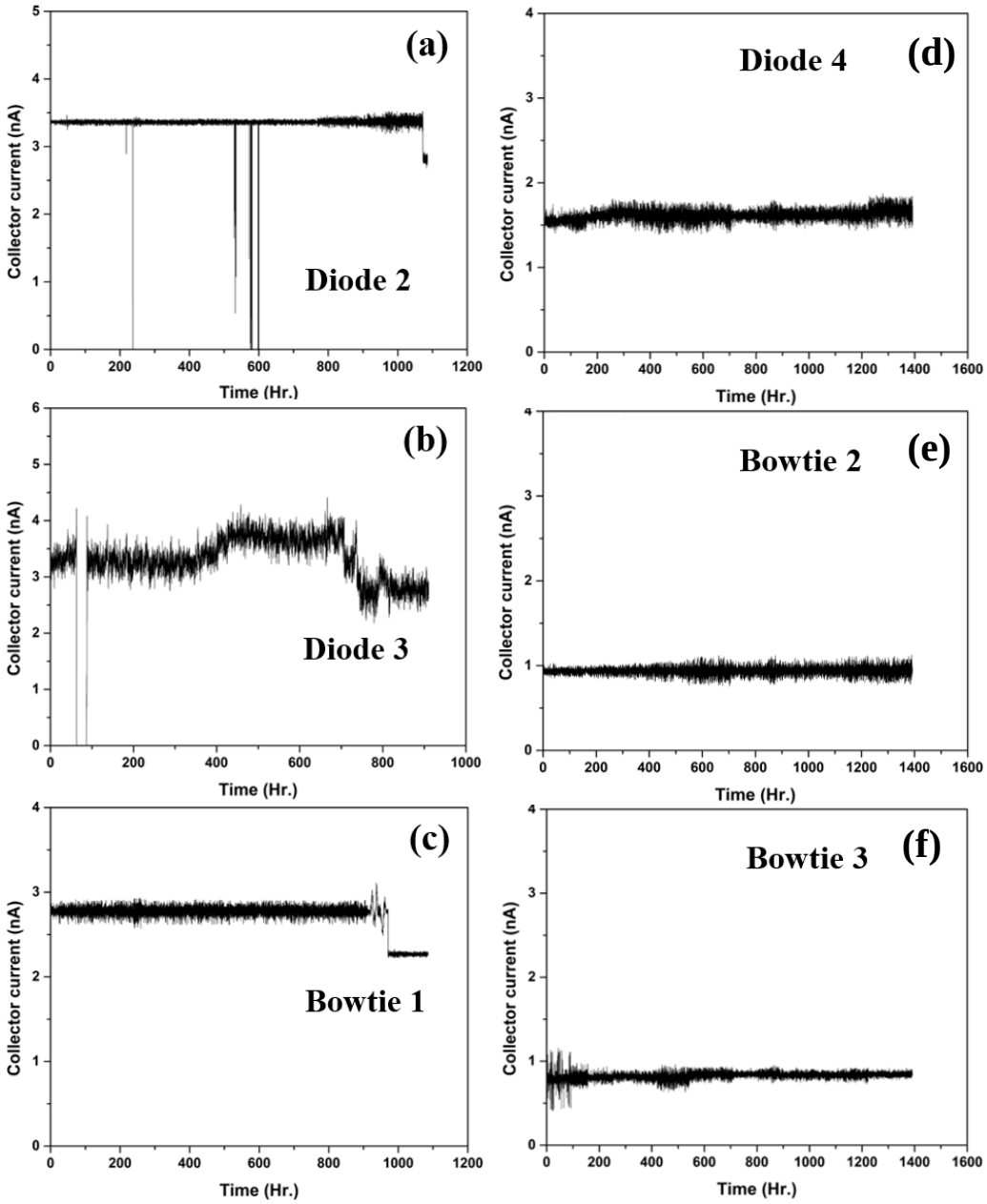

Figure 4-7: Long-term Stability Testing. (a-f) Lifetime electrical characterization of multiple devices showing stability in the order of at least $\sim$ 1000 h. The test was performed applying a 6V potential and recording the current every minute with an SMU.[63]

Fig. 4-6 shows an example of a typical IV characteristic of one of the bowtie and diode tested. It is worth noting that, as explained in Chapter 3, while the bowtie exhibits symmetrical behavior, the diode characteristic is rectified due to its geometrical asymmetry that favors the current flow from the tip (emitter) to the plate (collector).

Then multiple devices were tested setting a DC potential of 6V between the emitter and collector and recording the current for many hours. In particular, 7 devices' lifetimes were tested. One of the devices failed after 350 h, while the other 6 maintained a fairly stable output for more than 900 h as shown in Fig. 4-7.

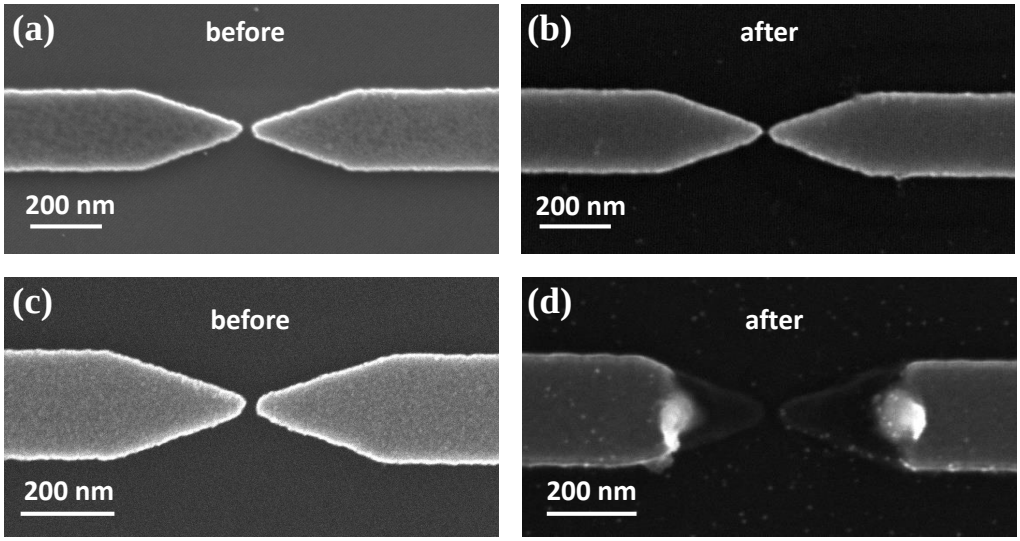

Figure 4-8: Post Imaging. SEM micrographs of before and after testing of a tip that survived the testing (a,b) and one where an arc occurred (c,d). The latter shows that the arc generated a very high current density to flow between the emitter and the collector with subsequent melting of the tip.

When a device fails, what typically happens is that an arc occurs between the emitter and the collector which causes the melting of the metal. This can be due to external instability of the voltage source which generates an instance of high potential between the tip, or it could be a problem intrinsic to the device, such as electromigration of the metal causing a reshaping of the tip with consequent formation of a high field region which, in turn, generates a local high current density resulting in an arc and then the melting of the tips. An example of such occurrence is shown in Fig.

4-8, where the imaging of before and after testing of a tip that survived the testing (a,b) and one where an arc occurred (c,d).

This lifetime test conclusively demonstrated that planar nano vacuum devices can be operated for long periods of time with excellent current stability. Moreover, it is worth noting that the DUTs were all individual devices. Arrays would have an even more stable behavior and could resist the loss of a few tips, therefore further increasing their lifetime.

4.3 pNVCT Testing

Characterization of three-terminal devices was also performed. In these devices, two gate electrodes are added in between the emitter and the collector. Ideally, the gate would set the potential in front of the emitter and would shield the collector potential, therefore univocally determining the current flowing from the emitter to the collector.

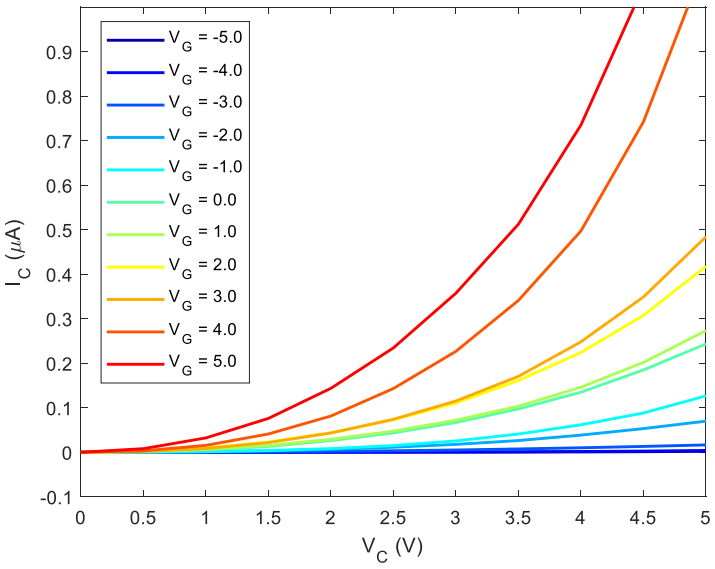

Figure 4-9: Output characteristic of a Planar Nano Vacuum Channel Au transistor. In this test, the collector current was recorded while sweeping the collector voltage for different values of gate potential. Clearly, the gate potential can be used to modulate the collector current but a saturation region is not present. This test was performed in a vacuum.

However, preliminary testing of these pNVCT output characteristics (i.e collector

current vs voltage sweeps at different gate voltage), shows a dependence of the collector current with the gate voltage as expected, but a saturation region is not present in the graph, as can be seen in Fig. 4-9. Moreover, this first batch of tested devices exhibited low reliability over time. Therefore, further testing and geometrical iterations are going to be necessary to optimize these devices, in order to obtain planar nano vacuum transistors that could be effectively used to build useful radiation-resistant electronics.

4.4 Conclusion

The emission physics of planar NVC diodes was investigated. To do so, the IV characteristics of two different emitter materials, Au and TiN, were analyzed under varying temperatures and atmospheric conditions. While past work had primarily used Fowler-Nordheim tunneling to model the emission physics of such devices, a large discrepancy was found between the fitted electric field enhancement factor and that expected from electromagnetic modeling. Upon closer inspection in this work, Schottky emission was found to dominate at lower applied bias values. In particular, it was found that for the Au devices temperature-dependent Schottky emission was the only observable regime before the onset of damage. Instead, for TiN, thanks to the possibility of exploring higher potentials given their higher physical robustness, the transition from Schottky to Fowler-Nordheim tunneling and then a final transition to saturation were clearly identifiable. The saturation regime was ascribed to the Child-Langmuir space charge limitation. Depending on the device requirements (e.g. low voltage or high transconductance) devices could be designed to operate in different regimes. These findings mark an important step toward the development of accurate models necessary for the design and realization of high-speed[41], robust[63] and radiation-resistant[3] vacuum nanoelectronics.

A pressure analysis also revealed a large reduction in the emission rate and an increase in the turn-on voltage of the devices due to a combination of oxidation and absorption of molecules on the surface. While this sensitivity verifies tunneling

emission and transport through free-space dominates compared to substrate leakage, it, unfortunately, indicates that such devices should be properly packaged despite the reduced free-space channel width. However, it is worth emphasizing that this degradation is reversible once the vacuum was restored. Additionally, the Au devices' lifetime was tested demonstrating long-term stability and the effect of possible arcing.

Finally, a preliminary analysis of three-terminal planar vacuum channel transistors was conducted revealing that indeed a gate electrode can be used to modulate the current between the emitter and the collector. Further testing and geometrical optimization of these devices are necessary to study and improve their reliability and reach a configuration that allows for a saturation region of operation in the output characteristic. This would be an important step toward the development of reliable nano vacuum channel electronics for operation in a harsh environment.

Chapter 5

TDSE Optoelectronic Simulation

In this chapter, the multiphoton and optical field tunneling emissions from metallic surfaces with nanoscale vacuum gaps are investigated. Most of this work was originally published in [64].

Developing ultrafast photosensitive devices has become increasingly important as these devices are instrumental for the realization of petahertz electronics as well as the further development of ultrafast metrology and information technology[14, 65, 66, 25, 42]. Ideally, a device for these applications would be simultaneously fast, sensitive, and capable of operating at room temperature. Photodetectors based on thermal absorption can be both sensitive and broadband, but, since thermal events happen on longer timescales, they have relatively slow response times. Superconducting detectors, on the other hand, are faster (they can achieve few-picosecond response times [67]), broadband, and can achieve single-photon sensitivity [68], but they require a cryogenic environment to work, which makes them expensive and difficult to integrate with other systems. While nanoscale and low-dimensional hot-electron detectors are easier to integrate and can operate at a similar speed (on the scale of 100s of GHz [69]), this is still orders of magnitude slower than recently demonstrated detectors based on multiphoton or optical-field tunneling emission [27, 70, 41]. However, while the instantaneous current response from multiphoton and optical-field devices has demonstrated the capability to respond at petahertz-level frequencies, they also require strong fields ($> 10\,\mathrm{V\,nm^{-1}}$) and are less sensitive than many alternative pho-

todetection schemes.

In this chapter, the impact of small DC bias voltages on the photoemission properties of surface-enhanced multiphoton and optical-field emission from broadly tunable photodetectors having nanometer-scale vacuum channels [27, 25, 71] was theoretically investigated. In particular, the analysis focus on how the additional DC bias can enable entry into the petahertz regime at reduced incident optical field strengths, while simultaneously improving detection efficiency. With adequate detection efficiency improvements, such detectors could provide a photodetection scheme capable of operating in ambient conditions that is simultaneously sensitive, ultrafast[41], compact, and easy to incorporate into integrated photonics platforms.

5.1 Biased Nanoantenna Photodetector Concept

In Fig. 5-1a, a schematic of one possible configuration for a nano-vacuum gap optical detector is presented: a plasmonic bowtie nanoantenna sitting on an insulating substrate. The antenna is comprised of an emitter and a collector electrodes, with a nano-vacuum gap on the order of a few to tens of nanometers in between (the materials do not necessarily differ and the coloring is simply for visualization). The two electrodes can be comprised in a bowtie configuration where two tips face each other as in the schematic, in a diode configuration where the collector is flat and is adjacent to a tip, or in a slot-waveguide configuration that supports traveling waves that travel within the gap. The latter case may be preferred in cases where large effective surface areas are desired for increased signal generation. In all cases, when the gap is very small, the preferential emission direction is dictated by the applied bias[72]. The emitter would ideally be fabricated from a plasmonic material, such as gold, enabling large optical field enhancements. For a gold bowtie nanoantenna configuration with an emitter-collector gap of 10 nm, optical-field enhancements on the order of 100× were calculated, which is consistent with what has been simulated and observed in similar devices [71, 25, 73]. The emitter and collector are connected to an external readout circuit via a nanowire, that with proper placement does not

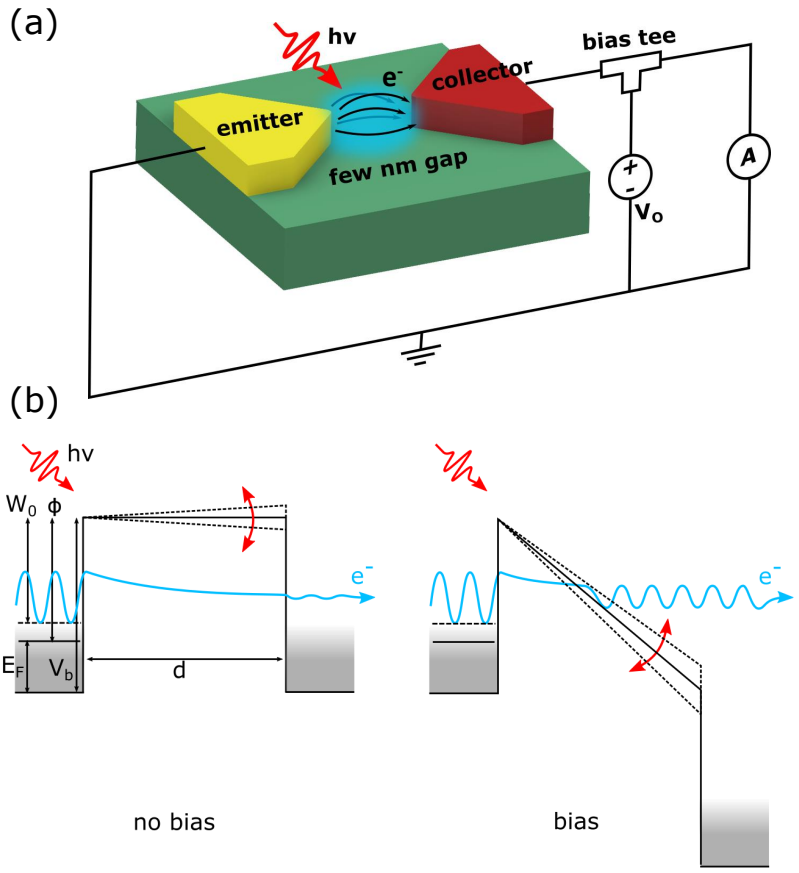

Figure 5-1: (a) Schematic of the device. A bias is applied in between the emitter (yellow) and the collector (red) of the nanoantenna while an optical pulse impinges on the device perturbing the field emission. (b) Emission mechanism with or without a bias applied between the emitter and collector (d being the gap between the two), showing how the presence of a bias bends the barrier which makes the emission more sensitive to an external optical field. In the schematic, the Fermi energy E_F, the barrier potential V_b, the work function ϕ, and the bound energy state of the emitted electron with respect to the vacuum level W_o are also highlighted.

impact the field enhancement at the metal surface [25]. When bias voltages of just a few volts are applied to the device, fields on the order of and exceeding $1\,\mathrm{GV\,m^{-1}}$ are achieved at the metal surface in the gap region, dramatically modifying the potential barrier of the surface electrons and interacting with the bound electronic states at the surface.

The potential profile along the length of the device when in a biased and unbiased state is sketched in Fig. 5-1b. When unbiased, the bound electronic state on the emitter side has a vanishingly low probability of tunneling through the nano-vacuum

gap. The effect of a weak infrared pulse is just that of small modulation of the barrier, which has a limited effect in modifying the emission probability (Fig. 5-1b dashed potential). Of course, a higher energy ultraviolet photon could excite an electron in the material to an energy state above the barrier for photoemission, but for the sake of this work only emission from longer wavelengths in the near- to mid-infrared is considered, where multiple photons would have to be absorbed to excite the electron to a state above the barrier. In contrast to the unbiased configuration, under a high bias, the barrier is bent by the applied potential and the tunneling probability increases exponentially. Thus, by placing a high bias on the collector, even a mild modulation of the barrier due to external alternating optical fields could lead to detectable tunneling photocurrents. Furthermore, by tuning the structure's size and geometry, the wiggling of the potential at the surface can be greatly amplified due to localized resonances. Together, these two effects make the device highly sensitive to any electromagnetic fields oscillating at the emitter's resonant frequency. The resonance of the nanoantenna at the laser frequency is not a requirement for the scheme to work, but can significantly increase the optical field enhancement. This increased field enhancement lowers the incident field intensity needed to generate a detectable signal. While the optical field enhancement works concurrently with the bias in lowering the detection threshold, the DC bias also sets a preferential direction of emission.

Unlike conventional photodetection where the photoelectron-conversion probability depends on material band structures that are difficult to engineer, field emission depends primarily on the peak surface field strength at the surface and the material's work function. This distinction means that by tuning the material geometry, it is possible to tune the operating bandwidth of such photodetectors from visible radiation through to the infrared and even into the terahertz range. While the focus of this work is to study the impact of the bias on the photoemission properties we limit our investigation to a single central wavelength in the near-infrared (IR). However, this detection scheme could also have a strong impact in the mid-IR[71] where there is a scarcity of competing technologies.

Due to the high non-linearity of cold-field electron tunneling with respect to the local field outside a material surface, applying a small DC bias between the anode and cathode of the nanoantennas can dramatically increase the probability of emission of a photoelectron from the surface for a weak incident optical field strengths (see below where it is shown a predicted increase of more than 3 orders of magnitude for an incident optical field strengths on the order of $[10^{-4} - 10^{1}]$ V nm^{-1}). Previous studies have investigated the effect of superimposed electric fields from optical and low-frequency electrical sources in different regimes and length scales[74, 71, 72, 75]. However, in this work, the effect of such a combination of optical and DC bias fields is investigated at the nanoscale in the weak-field (sub 10 V nm^{-1}) ultrafast (sub 100 fs) regime, which has received increasing attention in recent years given the rapid development of nanometer-scale fabrication processes and compact ultrafast optical sources [76, 77, 14, 24].

Taking advantage of the nanoscale gaps between the nanoantenna electrodes is crucial for high-speed weak field operation because the nanofabricated sharp tips can provide enhancement of both the DC and optical field and the nanogap allows for ultrafast operation. Subcycle response times of the instantaneous surface current have already been observed with similar structures in Refs. [25, 27, 78, 72], and the traveling time of the electrons in the gap is on the order of a femtosecond or less.[41, 79]. The effective capacitance of nanoantenna vacuum-gap photodetectors like those used in Ref. [25] was calculated to be $\sim$10 aF. When combined with the few-Ω-level resistances of typical antenna structures and connecting wires, this yields a time constant of one unit cell of the device of $RC < 1$ fs. In this work, it is shown that in the few-nm-gap regime, the application of a few-volt DC bias could enable sufficient detection efficiencies to sense fJ-level near-infrared pulses at room temperature. The ability to detect weak optical pulses with such simple, broadband, and high-speed devices would constitute an invaluable contribution to the development of modern ultrafast photodetector technology for applications such as carrier-envelope phase (CEP) detection [25], lidar[80], and petahertz-scale optical field sampling [81].

In the following sections, the time-dependent Schrodinger equation (TDSE) sim-

ulations used to model the bias-enhanced photoemission process and our simulation results are described. In particular, the focus is on the impact of high and low static electric fields on the evolution of the wavefunction in the nanoscale gap when excited by ultrafast optical pulses, as well as the dependence of the induced photocurrent with respect to both the optical and static field strengths. Finally, the impact of the material work function was analyzed before discussing our results and potential applications.

5.2 Bias-Enhanced Photoemission Model

In this section, the model used to simulate the bias-enhanced photoemission mechanism described in the previous section is discussed. First, the free space photon field was approximated as:

$$E_{\mathrm{o}}(t) = E_{\mathrm{o}}\ e^{-\frac{2\log(2)t^2}{\tau^2}}\cos(\omega t + \phi_{\mathrm{CE}}), \tag{5.1}$$

where E_{o} is the peak field, τ is the full width half maximum (FWHM) of the pulse, ω is the frequency and ϕ_{CE} is the phase. When an optical pulse interacts with the nanoantenna structure, it can excite a surface plasmon that confines the optical field, therefore enhancing it close to each tip (in the gap region between the emitter and collector).

In the case of a nano-vacuum gap detector, with one electrode at $x = 0$ and one at $x = d$, the electric field can be written as:

$$E(x,t) = FE_{\mathrm{o}}(t)\left(e^{-\frac{x}{L}} + e^{\frac{x-d}{L}}\right), \tag{5.2}$$

where F is the field enhancement factor (polarization dependent) at the surface and L is the enhancement decay length, which is typically of the order of 15 nm. Therefore

the time-dependent potential energy of an electron with charge q is:

$$U(x,t) = \int qE(x,t)\mathrm{d}x = -qFE_{\mathrm{o}}(t)L\left(e^{-\frac{x}{L}} - e^{\frac{x-d}{L}}\right) + C = -qFE_{\mathrm{o}}(t)2L\sinh\left(\frac{x-d/2}{L}\right) + C. \tag{5.3}$$

For gaps $d \ll L$ and evaluating the arbitrary constant C so that $U(0,t) = 0$, this can be approximated as:

$$U(x,t) \approx -qF'E_{\mathrm{o}}(t)x, \tag{5.4}$$

where $F' = 2e^{-\frac{d}{2L}}F \approx 2F$ is the field enhancement of the whole nano-vacuum gap detector. Putting this all together, in the biased and illuminated condition we can write the potential energy of the entire structure as

$$U(x,t) = \begin{cases} -qV_{\mathrm{b}} & \text{if } x < 0 \\ +q\left(\frac{V_{\mathrm{o}}}{d} - F'E_{\mathrm{o}}(t)\right)x & \text{if } 0 < x < d \\ -qV_{\mathrm{b}} + qV_{\mathrm{o}} - qF'E_{\mathrm{o}}(t)d & \text{if } x > d, \end{cases}$$

where V_{b} is the barrier at the interface between the material and vacuum, and V_{o} is the DC bias.

To properly account for the total emitted current from the structure, you need to consider emission from the entire ground-state electron population. Since here metallic emitters were considered, the emission from initial bound energy states W_{o}, populated according to the Fermi distribution, was integrated. The Fermi energy E_{F} was also considered to have an energy difference with respect to the vacuum level equal to the work function ϕ. In this framework the kinetic energy of the electrons of a specific bound state is $V_{\mathrm{b}} - W_{\mathrm{o}}$. A method similar to that used in Refs. [33, 82] was then followed to estimate cold field emission from static and optical fields, employing a custom TDSE solver, using discrete transparent boundary conditions [83]. Once solved for the wavefunction ψ, the transmission coefficient is evaluated as the ratio Γ between the transmitted and incoming probability currents, j_{trans} and j_{inc} respectively. The following equations are in atomic units.

$$\Gamma(W_o) = \frac{j_{trans}}{j_{inc}} = \frac{\mathbb{I}\mathrm{m}\left(\psi^* \frac{d\psi}{dx}\right)}{\sqrt{2(V_b - W_o)}}. \tag{5.5}$$

The total charge density emitted in the time interval $[t_0, t_1]$ can then be calculated as:

$$Q = \int_{t_0}^{t_1} dt \int_0^{V_b} dW_o \cdot N(W_o) \cdot \Gamma(W_o), \tag{5.6}$$

where $N(W_o) = k_B T/(2\pi^2) \ln\{1 + \exp[(E_F + W_o - V_b)/(k_B T)]\}$ is the incoming charge supply distribution for each ground state energy.

While the ambient device temperature is considered in determining the initial state electron distribution, it is worth noting that optically-induced thermal effects were ignored. This is reasonable since prior experimental work has shown that such optically-induced thermal effects play a negligible role in the device emission even in the case of much stronger optical fields when similar nanoantenna emitters are excited with ultrafast optical pulses [78, 25, 84, 85].

It is also noteworthy that alterations to this simplified potential model due to space-charge reshaping of the barrier and field penetration into the emitter were also considered. The photocurrent simulation results when incorporating these effects indicate that they do not impact the primary conclusions of this work, so are not discussed explicitly in this manuscript for the sake of clarity. In general, the impact of space charge is similar to that experienced by a slight alteration of the effective work function. Field penetration is rather weak for metals (for example, due to the large magnitude of the material's permittivity, the field strength inside gold is roughly 42× weaker than the surface field at 1 µm), and when incorporated only leads to a slight alteration in the power scaling slope for large optical field strengths.

5.3 Simulation Results

A metallic structure with a 5 nm gap was initially simulated using the model described in the previous section, imposing a work function of 4 eV. Fermi-Dirac statistics in the metallic electrodes and a potential profile as in Fig. 5-1b were assumed. The

fabrication of nanostructures with comparable features has been reported in the literature using a lift-off based patterning processes [78, 27, 70], where the size of the nanostructures can be adjusted to provide field enhancements on the order of 100× when a plasmonic material such as gold is employed according to our electromagnetic modeling. This enhancement is in line with recent experimental observations for similar structures [86, 73]. The system was perturbed with an external optical field waveform assuming a central wavelength of $\lambda = 1\mu m$ and a pulse duration of 30 fs FWHM. All the results in this work are expressed in terms of the field present in the gap instead of the incident field. This allows generalizing these results for any geometry regardless of the field enhancement that it can provide. The peak field strength used in this simulation was $10^{-2}\,\mathrm{V\,nm^{-1}}$. It is worth noting that if the field enhancement of the structure were to be indeed 100×, you would obtain this field strength with an applied field of $10^{-4}\,\mathrm{V\,nm^{-1}}$.

In Fig. 5-2 a,b the result of this simulation is plotted. In particular, the wavefunction evolution under the potential barrier inside the gap region is shown for two different bias conditions: 1 V and 5 V. This plot shows only the wavefunction of the electrons emitted from the emitter to the collector. The smaller and opposite contribution to the current due to the electrons emitted from the collector to the emitter is also taken into account but not shown here. For the case of a 1 V bias, the applied bias is not sufficient to bend the barrier enough to significantly enhance the photoemission and the photocurrent signature is very weak. One can also see that a non-negligible amount of the wavefunction is reflected back and forth within the barrier. On the other hand, for a bias of 5 V, one can clearly see a sub-optical-cycle modulation of the wavefunction and the probability amplitude of the wavefunction is more than 3 orders of magnitude higher than in the 1 V case (the scale of the plot is 3000× higher). This sub-cycle modulation is a signature of the optical field enhanced tunneling through the barrier. Therefore, from 1 V to 5 V bias, the system transition from envelope to subcycle emission. Moreover, the amplitude of the tunneled wavefunction in the 5 V case is more than 3 orders of magnitude higher than for the 1 V case, as can be clearly seen from the plot scales.

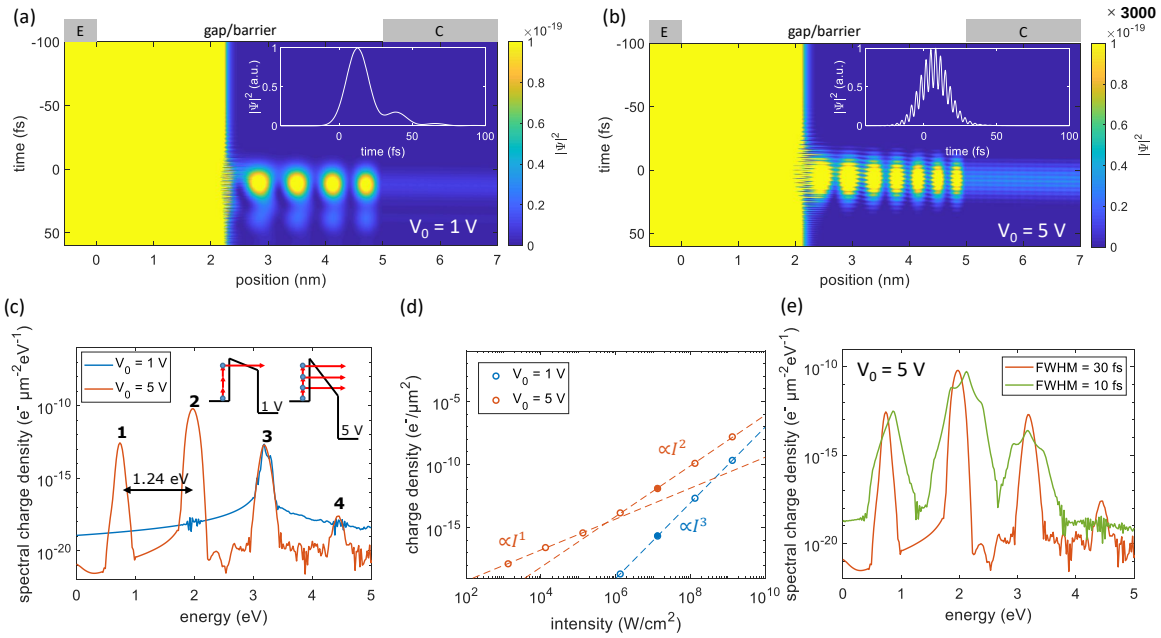

Figure 5-2: (a-b) Evolution of the right propagating wavefunction inside the structure in a condition of (a) low (1 V) and (b) high (5 V) bias. The optical field used in these simulations was $10^{-2}\,\mathrm{V\,nm^{-1}}$. The position of the emitter, gap/barrier, and collector are also highlighted on top of the graphs. The high bias case exhibits a probability of more than 3 orders of magnitude higher of emitting photoelectrons, as can be seen from the color bar scale. Moreover, in the second case, the fingerprint of the optical pulse is clearly visible in the wavefunction modulation after the barrier. The insets show the wavefunction evolution 1 nm after the barrier. (c) The energy spectrum of the emitted electrons at the two bias conditions. The energy plotted is taken with respect to the initial Fermi level E_F and after removing the bias potential. In the low bias case, only 3-photon processes are possible which results in a single peak in the spectrum. In the high bias case 1-, 2-, and 3-photon processes are all possible. Also the 4-photon process peak starts to appear, which corresponds to the case of an electron that absorbs enough energy to go over the barrier without any tunneling. The 3 peaks are separated by 1.24 eV, consistent with the fact that the optical field is generated by 1 µm photons. The inset shows a cartoon representation of the emission process. (d) Dependence of the charge density emitted at each pulse on the optical intensity I, showing that the low bias case (blue curve) follows a 3rd order power rule (I^3), while the high bias case (red curve) follows a 2nd order power rule (I^2). This is consistent with the highest peak in (c) being the one corresponding to a 3-photon and 2-photon process in the 1 V and 5 V bias cases respectively. (e) The energy spectrum of the emitted electrons due to optical pulses with a duration of 30 fs (red curve) and 10 fs (green curve).

A semi-periodic wavefunction modulation in time translates to frequency-domain peaks in the wavefunction that are integer multiples of the optical frequency, and thus

in the photoelectron energy spectrum, we observe photoemission peaks at multiples of the photon energy (the so-called above-threshold photoemission peaks [87]) as shown in Fig. 5-2c, where the emitted electron energy is taken with respect to the initial Fermi level E_F and after removing the bias level. In fact for a 1 V bias only 3 photon transitions are significant, explaining the single photoemission peak. On the other hand, for the case of the 5 V bias 1-,2-,3- and 4-photon events are all possible, so you see multiple peaks in the energy spectrum, all spaced by $\hbar\omega \approx 1.24\,\mathrm{eV}$ apart from each other. This is also demonstrated in Fig. 5-2d when examining the power-law scaling of the photoemission for each biasing condition. Increasing the optical power, or equivalently increasing the peak optical field strength at the nanoantenna surface, increases the probability of extracting an electron. The intensity corresponding to the case portrayed in Fig. 5-2c is highlighted with solid dots. The two curves in Fig. 5-2d show the emission rate as a function of optical power for the two bias cases shown in Fig. 5-2a and b. The 1 V bias case shows a 3rd power dependence on incident optical power which is consistent with the fact that 3 photon transitions dominate. On the other hand, the 5 V bias case shows a 2nd power dependence indicating that a 2-photon transition process is the most probable. This is consistent with the observations in Fig. 5-2d where the 2 photon peak is more than one order of magnitude higher than the other photon transition peaks. The appearance of multiple peaks when increasing the DC bias suggests the onset of optical-field emission when the Keldysh parameter γ is still above unity (It is worth noting that in this chapter γ refers to the Keldysh parameter, not the field enhancement, as used in the previous chapters). This would mean that an external bias can be used to lower the threshold between multiphoton and optical-field emission (or equivalently between weak-field and strong-field) to much lower fields. In fact, while this transition typically happens when $\gamma < 1$, which corresponds to $E > 9\,\mathrm{V\,nm^{-1}}$, with a bias of 5 V the system appears to be already in optical-field emission regime when $E = 10^{-2}\,\mathrm{V\,nm^{-1}}$ or $\gamma = 898$.

It is also worth noting that when the pulse gets shorter its bandwidth is larger. This has a direct consequence on the width of the energy peaks. This can be seen in

Fig. 5-2e where two pulses with the same peak power but different pulse duration (30 fs and 10 fs FWHM) are analyzed. It is clearly observable that the energy distribution of the electron emitted due to the 10 fs pulse is much wider. This effect could be exploited in a detection scheme that uses energy filtering.

Next, the influence of the DC bias voltage (or, equivalently, the gap field) on the photocurrent is evaluated in more detail.

To differentiate between the photocurrent and current generated from tunneling induced by the DC gap field, the current generated in the system was first simulated in a steady-state condition at different DC gap field levels with no optical field. In particular, a static gap field strength between 0 and $4\,\mathrm{V\,nm^{-1}}$ was considered, which can be achieved by applying a bias of less than 20 V using a nanostructure with a 5 nm gap. Then, the TDSE calculation starting from this initial steady-state with the static gap field applied was performed incorporating the optical field waveform as a time-dependent perturbation of the potential as shown in Fig. 5-1. To obtain the photocurrent, the steady-state current was subtracted from the total current after activating the optical pulse. The same calculation was performed sweeping the static field magnitude and then repeated the calculation for different optical peak fields with a pulse duration of 10 fs FWHM, ranging from $1 \times 10^{-4}\,\mathrm{V\,nm^{-1}}$ to $1 \times 10^{1}\,\mathrm{V\,nm^{-1}}$. Fig. 5-3a shows the result of this simulation.

To provide context for the field strengths simulated and how they relate to incident pulse energy, one can think of the bottom curve (with incident optical field $E = 1 \times 10^{-4}\,\mathrm{V\,nm^{-1}}$) in Fig. 5-3a (turquoise) as approximately corresponding to a single photon at 1 µm having a duration of 10 fs and focused down to a $1\,\mu\mathrm{m}^2$ area with field enhancement of 1. This is the worst-case scenario since typical field enhancement values for gold nanoantennas with comparable gap sizes have been shown to range between 20 and 100 [25, 86, 73]. The upper limit for the peak optical field we consider is $E = 10\,\mathrm{V\,nm^{-1}}$, about the level at which the Keldysh parameter $\gamma = 1$ and is borderline between weak and strong field emission. This peak field strength is well within the damage threshold of nanoscale photoelectron emitters. Yang et al.[25] showed that, in gold, fields at the nanoantenna tips of $\sim 50\,\mathrm{V\,nm^{-1}}$ ($1.4\,\mathrm{V\,nm^{-1}}$

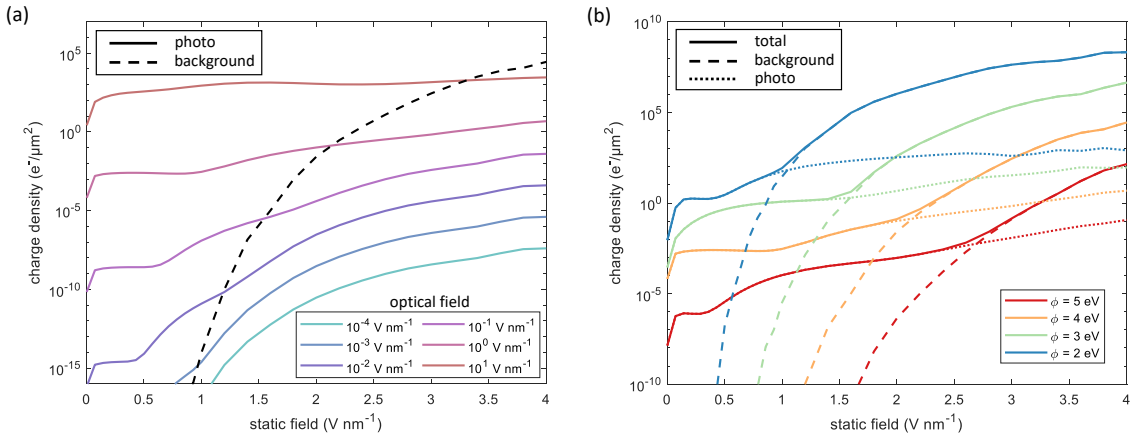

Figure 5-3: (a) Time-dependent Schrodinger equation (TDSE) simulation of the charge density emitted for a 1μm pulse with 10 fs FWHM pulse duration and optical field ranging from $10^{-4}\,\mathrm{V\,nm^{-1}}$ to $10^{1}\,\mathrm{V\,nm^{-1}}$, for different static fields. In this simulation, a work function of $\phi = 4\,\mathrm{eV}$ was assumed for the emitter and collector material. The total number of electrons extracted for 1 ns time window coming from the background emission due to the bias is shown with a dashed line. (b) TDSE simulation of the charge density emitted for materials with work functions ϕ ranging from 2 eV to 5 eV extracted in a 1 ns time window with an impinging optical pulse is shown by the solid lines. The fraction of these electrons due to the bias (dashed) and the photon (dotted) are also highlighted. Here the field peak strength was assumed to be $1\,\mathrm{V\,nm^{-1}}$

incident field with 40x field enhancement) can cause some reshaping but are not sufficient to damage the devices. Moreover, harder materials such as TiN can be used to fabricate the devices if the fields to be detected are significantly higher.[31]

One possible concern with this detection scheme is the need to differentiate photoelectron emission from the background DC field emission. While the photocurrent increases exponentially with bias voltage, so too does the tunneling current induced by the static field. The black dashed curve in Fig. 5-3a shows simulation results depicting the total number of electrons extracted per unit area during a 1 ns window, separating the effect of the DC bias and that of the incident optical pulse. This simulation shows that after a certain point the charge density extracted by the static field becomes much larger than that induced by the optical pulse. Therefore, assuming a detector having a 1 GHz rise time, the detection of a single-shot signal should be carried out in a region where the bias provides the maximum possible gain and the photocurrent is still distinguishable from the background. For instance, for the case

of an optical field of $F = 1 \times 10^{-1}\,\mathrm{V\,nm^{-1}}$ in Fig. 5-3a, this operating region would be below $1.5\,\mathrm{V\,nm^{-1}}$ of static field strength. A possible workaround that could be used to operate the detector at higher DC field levels would be to somehow implement an energy filter on the emitted electrons. As seen in Fig. 5-2c, the photoelectrons have a very specific energy fingerprint compared to those emitted by the static bias field. By only allowing the higher-energy photoelectrons to pass through to the detection electronics, they could be distinguished from those emitted by the static bias. Of course, in an application where the optical signal is repeated at a known frequency, lock-in detection techniques could be used to differentiate the photocurrent from the background DC current allowing for higher static bias fields to be used as well. However, the electron emission from the static bias will still contribute to the noise floor in this case.

In Fig. 5-3b, the influence of the material work function on the bias-enhanced photoemission was also studied. Simulations were performed for materials with different work functions ϕ, ranging from 2 eV to 5 eV, as a function of the gap field. It is clear from the simulation that a low work function can provide a considerable advantage assuming everything else is equal. However, it should be considered that different materials result in different field enhancements. For example, while gold structures exhibit a larger work function of roughly 5.1 eV, they also provide very large optical field enhancements due to their plasmonic properties. Materials having much lower work functions can be engineered [88, 89], but they are generally unstable and difficult to nanofabricate. Thus, the selection of an optimal material will require a trade-off between achievable field enhancements and material work functions.

In Fig. 5-4 a and b the effect on the optically emitted charge density of the ultrafast pulse duration and the gap size, respectively, was investigated. In both cases, the peak optical field strength was kept constant at $1\,\mathrm{V\,nm^{-1}}$. In the unbiased condition, there are nearly equal amounts of charge density due to the photocurrent excited from the emitter to the collector (left-to-right) and the collector to the emitter (right-to-left), which when combined results in almost zero net photocurrent. However, since the emission is ruled by a highly nonlinear process as a function of field strength, with

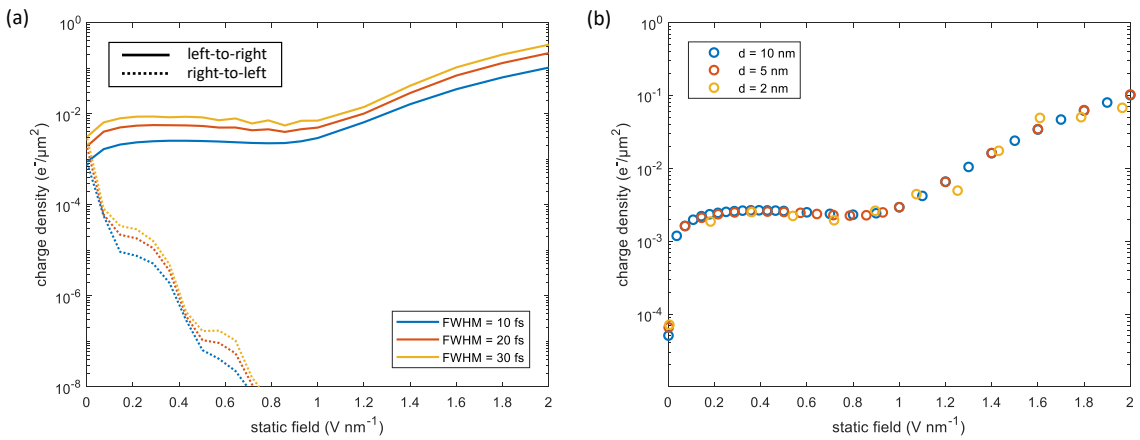

Figure 5-4: (a) Time-dependent Schrodinger equation (TDSE) simulations of the charge density emitted for a 1μm pulse, a work function of $\phi = 4\,\mathrm{eV}$, and a peak optical field strength of $1\,\mathrm{V\,nm^{-1}}$. The simulation was performed for different pulse duration ranging from FWHM =10 fs to 30 fs. The contributions to the charge density due to the photocurrent arising from the emitter to the collector (left-to-right, solid curves) and from the collector to the emitter (right-to-left, dashed curves), are plotted separately. (b). TDSE simulations of the charge density per pulse emitted for different gap sizes ranging from d =2 nm to d =10 nm. The simulations are performed assuming a pulse with the same characteristics as in (a) and a duration of 10 fs .

sufficient bias the emission in the direction opposite to the preferential one set by the static field is strongly suppressed resulting in a rectified response to the optical field. As shown in Fig. 5-4a, a static field of just $0.1\,\mathrm{V\,nm^{-1}}$ is already more than sufficient to achieve almost full rectification. Once rectified, the emitted photocurrent scales almost linearly with the number of optical cycles. We also note in Fig. 5-4b that once the gap size is smaller than the field enhancement decay length so that our approximations hold, it has almost no effect on the emitted charge density provided the static field is fixed. Of course, we note that obtaining the same bias field with a larger gap would require a larger potential.

5.4 Conclusion

The impact of a DC voltage bias on photoemission from metallic surfaces surrounding few-nm vacuum gaps was investigated. Nanoscale vacuum gaps enable the application of very large static fields (beyond $1\,\mathrm{GV\,m^{-1}}$) with the application of only a few volts.

Using TDSE simulations, it was found that these static fields can have a dramatic impact on the photocurrent induced in the surfaces surrounding the gap. In particular, the application of a few-volt bias forced a transition in the system from a condition of envelope-driven emission to a sub-cycle response to the external optical field. In fact, the bias appears to lower the threshold between multiphoton and optical-field emission. We showed that optical-field emission may occur in a weak-field condition, with a Keldish parameter of $\gamma = 898$, orders of magnitude higher than the typical requirement of $\gamma \approx 1$ in the case of no additional DC bias. The bias also causes a dramatic enhancement in the photoemission yield in the weak-field regime, with a typical improvement of more than 3 orders of magnitude in the electron emission probability for an incident optical field strengths on the order of $[10^{-4} - 10^{1}]$ V nm^{-1}. We also analyzed and discussed how using a material with a lower work function can benefit the sensitivity and the possible trade-offs with the field enhancement. The results highlighted by this work can have an important impact on better understanding of the emission mechanisms and in the design of future detectors for multiple applications, from petahertz electronics to lidar to ultrafast metrology.

Chapter 6

PHz Processing of Optical Fields

In this chapter, NVC devices are exploited for the petahertz processing of optical fields. In particular, they are used as building blocks to develop a novel technique to sample optical fields with attosecond resolution and to study carrier dynamics. Some of this work was originally published in [81].

As discussed in the previous chapter, planar nano vacuum devices are extremely fast and can be operated at petahertz frequencies, hence they can be driven both with electrical and optical fields. In this chapter, their use to process signals in the petahertz regime is addressed. In particular, this dual mode of operation of these devices, optical and electrical, is used to develop a technique that exploits the ultra-high bandwidth field-driven response of these nanoscale vacuum channel devices to sample weak optical fields. This work not only provides yet another demonstration of the high-bandwidth operation of Au nano-vacuum channel devices, but provides an extremely valuable technique that combines cutting-edge nanoscience and ultrafast nonlinear optics delivering detectors able to track weak optical field waveforms in the time domain with extreme accuracy. The detectors are chip-scale and could be easily incorporated into integrated photonic platforms.

Time-domain spectroscopy in the Terahertz regime has already been proven to be extremely powerful for the design of electrical systems and for many spectroscopy applications[90, 91, 92, 93, 94]. Spectroscopy in the near-infrared and long-wavelength visible spectral regions is a critical technique for biological, pharmaceutical, and food-

safety applications as those wavelengths penetrate deep into the sample. Due to the potential of these detectors to provide improved molecular selectivity and sensitivity in this spectral regime, this work promises to have a wide-ranging impact across many areas of biomedical research and bioengineering. In fact, analyzing the molecular composition of in vivo samples is extremely important for biomedical research and medical diagnostics and monitoring. When molecules are excited by the near-infrared light resulting in vibrational dynamics and energy loss. These excitations leave behind a fingerprint on the transmitted optical field in both the temporal and spectral domains. However, in standard spectroscopic methods, only the absorption spectra are provided, with phase information typically ignored. This phase information is crucial for reconstructing vibrational dynamics in the samples of interest. Time-domain, field-resolved spectroscopy is a promising candidate to tackle this problem by providing information about both the energy loss and corresponding phase information [95]. Sub-cycle optical field sampling in the NIR and visible would be extremely valuable also in many more areas of science and technology. In fact, it can be used to study the role of optical-field-controlled coherent electron dynamics in the control of chemical reaction pathways[96], to investigate petahertz-level electrical currents in solid-state systems[97, 66, 98], and to better understand light-matter interaction and exciton dynamics important to photovoltaic and photosynthesis.

Time-domain field-resolved techniques, such as manipulation of attosecond electron wavepacket emission[98, 99, 100], electro-optic sampling[101] and attosecond streaking [102, 103, 104], do exist. However, they require lasers with large energies (millijoule-level), room-sized apparatus, and/or vacuum enclosures to operate [98, 99, 95, 42]. Our technique leverages the free-electron emission from nanostructured plasmonic nanoantennas[75, 76, 105, 24, 106] generated by a compact (shoe-box size) ultrafast driver laser (at picojoules-level energies)[107, 84, 78, 108] to sample a weak optical signal field that can carry this molecular fingerprint with attosecond resolution. This time-domain, field-resolved spectroscopy technique uses a device with a compact form-factor (micron-scale), is integratable[26, 72], does not require a special environment or very high-power lasers for operation, and employs conventional labo-

ratory electronics, all while detecting very weak optical field waveforms with energies of the order of few fJ, 6 orders of magnitude lower than the competing state of the art. For these reasons, the field-sampling technique we developed could become a remarkable tool in the hands of biomedical engineers and medical professionals.

The experiments related to the demonstration of the optical field sampling reported in this chapter were conducted together with Dr. Mina Bionta, postdoctoral researcher at MIT, and Felix Ritzkowsky, visiting graduate student from DESY.

6.1 Working Principle

The schematic and the SEM micrograph of the sampling device are depicted in Fig. 6-1 a and d, respectively. Such a device is comprised of an array of gold nanoantennas on a BK7 substrate. The nanoantennas have two electrodes, an emitter and a collector, and are designed using an asymmetric geometry so to establish a preferential emission direction (i.e. a rectified behavior), similarly to what was described for the diodes in Chapter 3. While the collector has a standard wire geometry, the emitter has a triangular shape which provides a $\sim 35\times$ field enhancement at 1170 nm. This is a combination of geometrical field enhancement due to lightning rod effect[109], and plasmonic field enhancement due to excitation of surface plasmons, analogously to what was shown in [25]. The triangle shape and size were informed by COMSOL simulations, which were used to determine the parameters that maximize the plasmonic response at the desired optical frequency. A simulation of the final structure is shown in Fig. 6-1e (simulation performed by Dario Cattozzo Mor). The large field enhancement allows the system to be sensitive and detect much smaller fields.

Fig. 6-1b illustrates the working principle of such a device. The array is biased to increase its sensitivity as explained in Chapter 5, and is illuminated by two optical pulses, the driver and the signal. The driver generates sub-cycle optical-field-driven tunneling of electrons, while the signal acts as a small signal perturbation. The sub-cycle characteristic of emission (on the order of hundreds of attoseconds[72, 78]) is ensured by the strong non-linearity of emission in Fowler-Nordheim regime, and

it is the key factor determining the detection bandwidth (e.g. a pure δ emission would mean unlimited bandwidth). Prior work demonstrated the sub-cycle response of these devices via their CEP sensitivity.[25, 27, 72, 78] If the signal is sufficiently smaller than the driver (i.e. $\sim$3 order of magnitude for the condition used in our experiment), the perturbation to the emitted current will be linear. Therefore, if the delay between the driver and the signal is scanned, the driver can be used to sample the signal at each time step through the aforementioned linear modulation. Hence, the time dependence of the signal field can be obtained with a direct measurement.

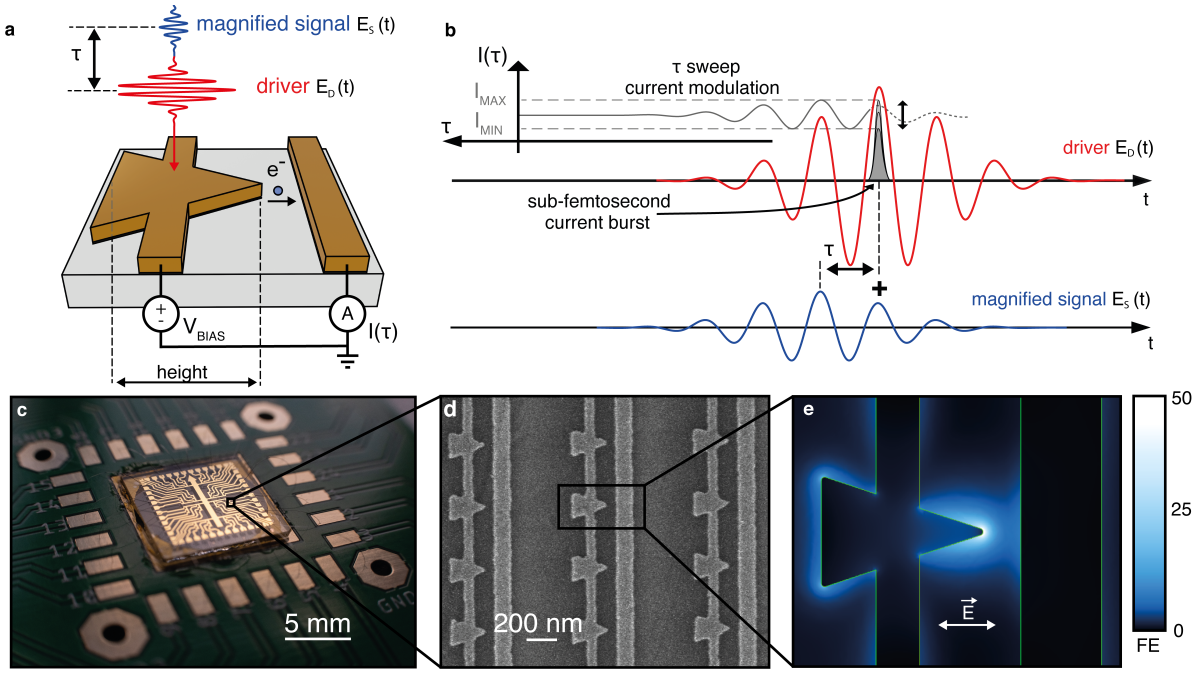

Figure 6-1: (a) Schematic of the device. (b) Depiction of the optical-field sampling process. Attosecond electron bursts are driven from an electrically-connected gold nanoantenna (see (a)) by a strong optical waveform driver ($E_{\mathrm{D}}(t)$, red), collected by an adjacent gold wire, then measured using an external current detector (see Methods). The weak signal waveform ($E_{\mathrm{S}}(t)$, blue), with a peak intensity of 1×10^{-4} that of the driver pulses, modulates the average photocurrent generated by the driver pulse, $I(\tau)$, as a function of delay, τ (grey). The amplitude of the signal waveform is artificially magnified in (a) and (b) for visibility. (c) Photograph of the nanocircuit embedded on a printed circuit board. (d) Scanning electron micrograph of the device. (e) Simulated electric field enhancement around a nanoantenna. The maximum field enhancement is $\sim$35 (on resonance). FE: field enhancement factor. E: polarization direction of the incident electric field.

From a theoretical standpoint, this problem is described in the following. The

nanoantenna is illuminated by the strong driver and weak signal pulses: $E_{\mathrm{D}}(t)$ and $E_{\mathrm{S}}(t)$ respectively. At the tip of the nanoantenna, the driver field generates a local field

$$E_{\mathrm{D}}^{(\mathrm{L})}(t) = \mathcal{F}^{-1}\left(\tilde{H}_{\mathrm{Pl.}}(\omega)\cdot\tilde{E}_{\mathrm{D}}(\omega)\right) \tag{6.1}$$

where $\tilde{H}_{\mathrm{Pl.}}(\omega)$ is the transfer function of the nanoantenna and $\mathcal{F}^{-1}$ is the inverse Fourier transform. Analogously, we can define the local signal field:

$$E_{\mathrm{D}}^{(\mathrm{S})}(t) = \mathcal{F}^{-1}\left(\tilde{H}_{\mathrm{Pl.}}(\omega)\cdot\tilde{E}_{\mathrm{S}}(\omega)\right) \tag{6.2}$$

If the driver is sufficiently strong to bend the barrier potential and generate optical-field-driven tunneling of electrons [84, 27, 25, 78], the instantaneous emision can be described by Fowler-Nordheim model, where the rate of emission is:[33, 110, 82]

$$\Gamma\left(E\right) \propto E^2\cdot\exp^{-\frac{F_t}{|E|}} \tag{6.3}$$

with $F_t = 78.7\,\mathrm{V\,nm^{-1}}$ being the characteristic tunneling field strength for gold.

Considering a delay τ between the signal and the driver the current detected at the collector can be written as the time-average of the emission rate in the laser repetition rate period $T_{\mathrm{Rep.}}$:

$$I(\tau) \propto \int_{-\frac{T_{\mathrm{Rep.}}}{2}}^{\frac{T_{\mathrm{Rep.}}}{2}} \Gamma\left(E_{\mathrm{D}}^{(\mathrm{L})}(t-\tau) + E_{\mathrm{S}}^{(\mathrm{L})}(t)\right) dt, \tag{6.4}$$

Since the signal is not sufficiently strong to generate optical-field-driven tunneling on its own, and it is much smaller than the driver, it can be treated as a small-signal perturbation through Taylor expansion:

$$I(\tau) \propto \int_{-\frac{T_{\mathrm{Rep.}}}{2}}^{\frac{T_{\mathrm{Rep.}}}{2}} \left(\Gamma\big(E_{\mathrm{D}}^{(\mathrm{L})}(t-\tau)\big) + \left.\frac{\mathrm{d}\Gamma}{\mathrm{d}E}\right|_{E_{\mathrm{D}}^{(\mathrm{L})}(t-\tau)}\cdot E_{\mathrm{S}}^{(\mathrm{L})}(t)\right) dt. \tag{6.5}$$

The first term is just going to result in a constant background. The second term (referred from now on as $I_{\mathrm{CC}}(\tau)$) is the current signal of interest. Noticing that this is a cross-correlation term, we can write its Fourier transform as:

$$\tilde{I}_{\mathrm{CC}}(\omega) \propto \mathcal{F}\left(\left.\frac{\mathrm{d}\Gamma}{\mathrm{d}E}\right|_{E_{\mathrm{D}}^{(\mathrm{L})}(t)}\right)^{*} \cdot \tilde{E}_{\mathrm{S}}^{(\mathrm{L})}(\omega), \tag{6.6}$$

Therefore, the resulting current measurement is linearly modulated by the local optical field generated by the weak signal, making this measurement scheme a viable option for time-domain spectroscopy of optical fields.

This detection scheme uses similar principles to hetero- and homo-dyne methods that are often used in techniques such as frequency-comb spectroscopy[111, 112, 113] However, while these methods generally are only sensitive to the time-averaged optical intensity which limits their bandwidth to the amplitude spectrum of the local oscillator, our scheme exploits sub-cycle field gating which uses the highly nonlinear emission process from metal tips to generate electron bursts extremely confined in time (i.e. with large frequency spectrum), therefore greatly extending the detection bandwidth.

6.2 TDSE Simulation

Using a framework analogous to that described in Chapter 5 the optical field sampling technique explained in the previous section was simulated. In this simulation, two pulses were sent onto the nanoantennas: a driver and a signal pulses. The two pulses field were defined as:

$$\begin{cases} E_D = E_0 \operatorname{sech}^2\left(\frac{t}{T_{FWHM}}\right) \cos(\omega t + \phi_{CE}) \\ E_S = rE_0 \operatorname{sech}^2\left(\frac{t+\tau}{T_{FWHM}}\right) \cos(\omega(t+\tau) + \phi_{CE}) \end{cases} \tag{6.7}$$

where T_{FWHM} is the pulse length, ω is the central frequency, τ is the delay between signal and driver, ϕ_{CE} is the carrier envelope phase, and r is the ratio between the driver and the signal.

In this scheme, the driver pulse is going to sample the field of the signal at a specific instant (i.e. the current burst modulation is going to be proportional to the level at which the signal pulse is at the moment when the burst is generated by the

driver), set by the delay between the driver and the signal.

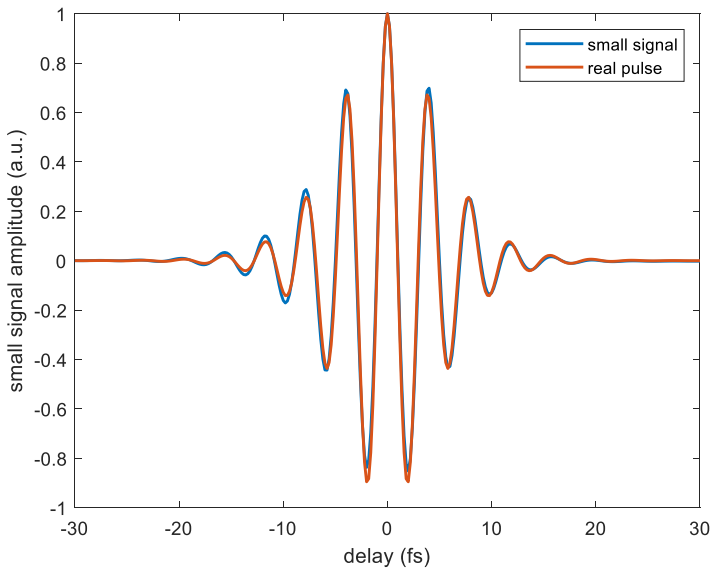

Figure 6-2: Optical Field Sampling Simulation. Graph showing a comparison between the signal pulse incident on the nanoantenna (real pulse), and the integral of the current density that reached the collector, for different delays τ between the signal and the driver. As can be observed, there is a very good match between the two, demonstrating the viability of this measurement scheme.

Therefore, in this simulation, the signal and driver are scanned one with respect to the other and, at each delay, the total emitted current within the simulated time window is binned (i.e. integrated), the resulting charge density is going to be proportional to the signal plus a constant background level due to the driver.

Fig. 6-2 shows the result of the simulation of this sampling technique. Each point on the graph corresponds to charge integration over the entire simulated time window. The retrieved current almost perfectly replicates the incoming signal pulse. Hence, we can conclude that this framework can be used to perform time-domain spectroscopy of ultrafast optical fields.

6.3 Experimental Setup

To demonstrate that this technique can be successfully used for optical field sampling it is necessary to show it experimentally. This was done using a few-cycle super-

continuum source. A supercontinuum source is a laser source that exploits the $\chi^{(3)}$ response of a non-linear medium to increase its bandwidth. This increased bandwidth allows for the generation of a very short pulse. This temporal confinement is quite important for this approach to optical field sampling for two reasons:

1. A short pulse, at equal power, has a much higher peak field. Since this technique is field-driven, the device can be operated with low power, which reduces the power consumption and the heat load to the device, increasing its lifetime. Gold devices are particularly susceptible to thermally-induced degradation[25].

2. A short pulse reduces the number of cycles that contribute to the current signal, ideally restricting it to only the central one. This increases the spectral coverage of the sampling response.

The laser used was a 1.17 µm, 10 fs (2.5 cycles) supercontinuum source.[114] Fig. 6-3a is a schematic of the source, which is comprised of three main stages

1. An oscillator stage: the pulse is generated in an Er fiber oscillator, which outputs a 125 fs, 1550 nm, 100 pJ pulse

2. An amplification stage: the pulse energy is amplified in Erbium-Doped Fiber Amplifier (EDFA), which outputs a 150 fs, 1550 nm, 5 nJ pulse

3. An supercontinuum generation stage: the pulse energy is first compressed in a prism compressor to 80 fs and then is sent to a Highly-Nonlinear Fiber (HNF) where essentially through a non-linear process power is traded for bandwidth. Finally, the output is once again compressed in a second prism compressor, which outputs a 10 fs, 1170 nm, 200 pJ pulse

Part of the output, the 900 nm tail and the 1800 nm notes are also sent to an f-to-2f interferometer, which is used to stabilize and control the carrier-envelope phase (CEP) of the pulse.

Fig. 6-4 shows the spectrum at the output of the oscillator and of the supercontinuum measured with an optical spectrum analyzer (OSA), and a schematic of the

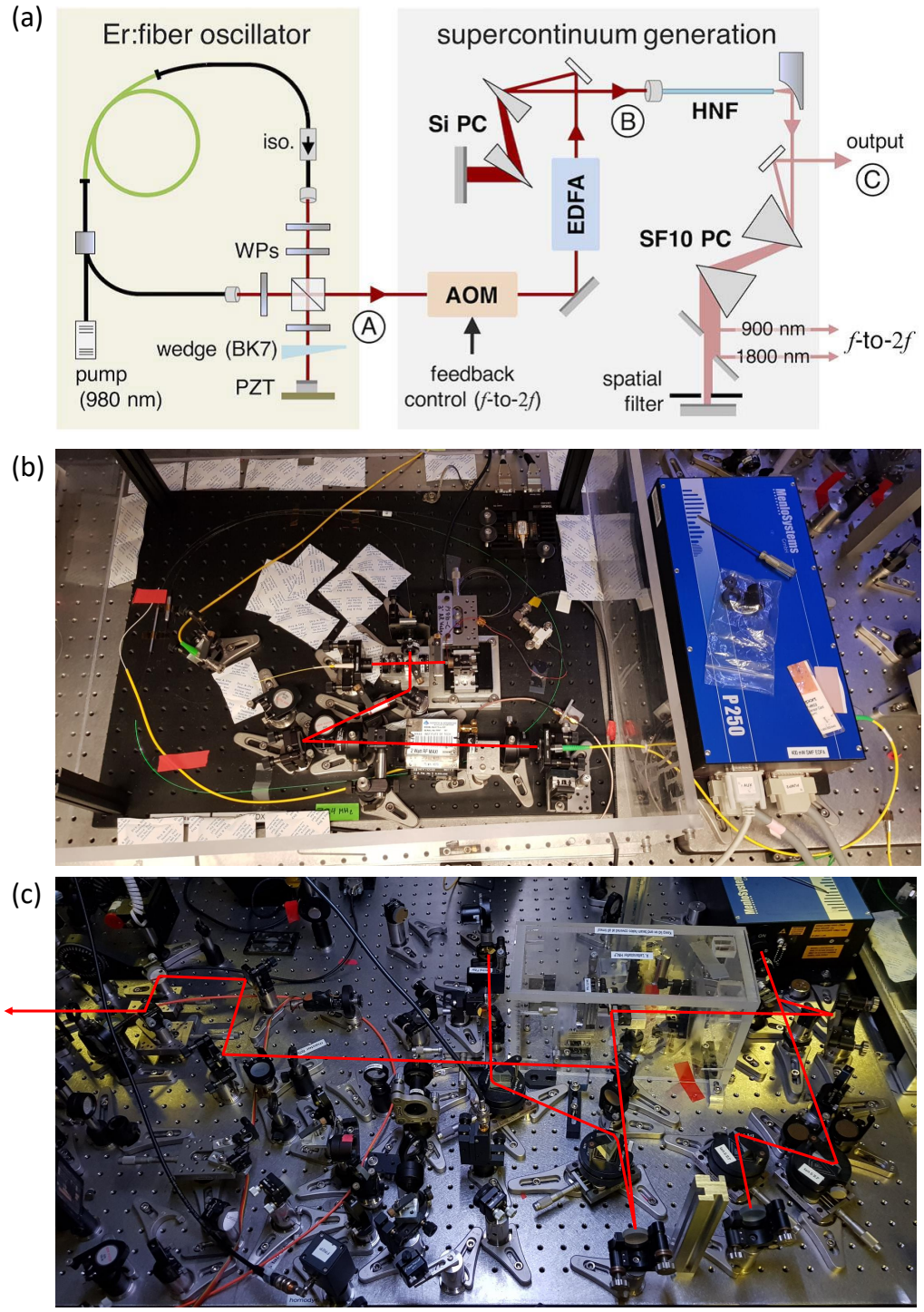

Figure 6-3: Supercontinuum Source. (a) Schematic of the CEP-stabilized laser pulses with a central wavelength of 1170 nm, duration of 10 fs, and repetition rate of 78.4 MHz. [114] (b) Photograph of the oscillator and amplification stages. (c) Photograph of the supercontinuum generation stage.

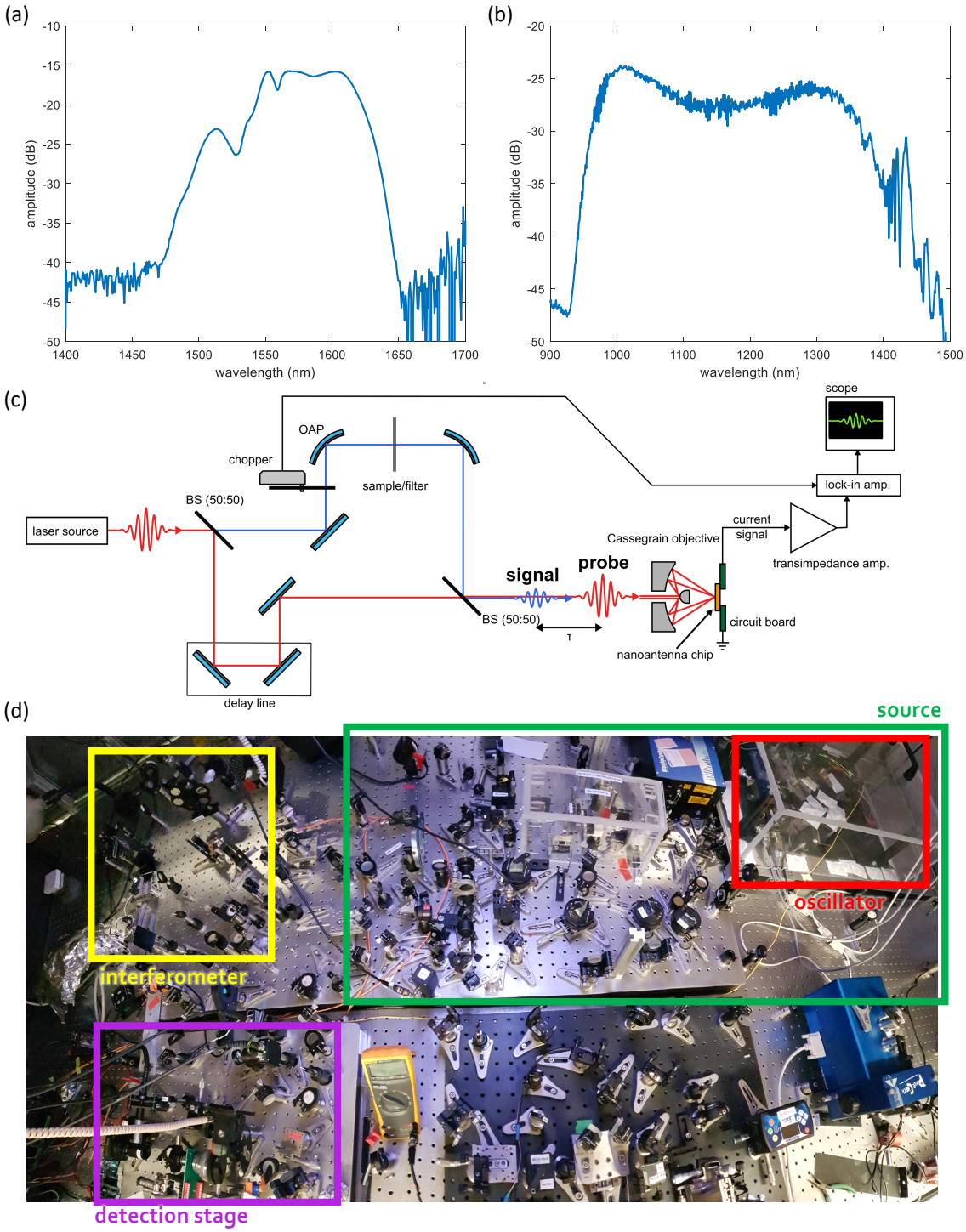

Figure 6-4: Laser spectra and experimental setup. (a) Spectrum at the output of the oscillator measured with an OSA. (b) Spectrum at the output of the supercontinuum stage measured with an OSA. (c) Schematic of the measurement setup. (d) Photograph of the experimental setup highlighting the different stages.

measurement setup. The supercontinuum output is sent to a Mach-Zender interferometer, where the signal and driver arms are separated and then recombined with two beam splitters. In the signal arm, two off-axis parabolas (OAP) are positioned to generate a focus where to place any sample of interest, and a chopper, to be used for lock-in detection. Lock-in detection is going to be necessary in this case because the measurement requires isolating the modulation due to the small signal from the background due to the driver. A delay stage is also placed in the driver's arm to control the delay τ between signal and driver pulse. Finally, after recombination, the optical pulses are sent to the detection stage, which is comprised of:

1. a reference photodiode to check overlapping in space and time of the two pulses
2. a Cassegrain objective to focus on the chip
3. a PCB with the chip containing the nanoantenna arrays mounted on a 3-axis stages
4. a microscope setup to align the chip to the laser

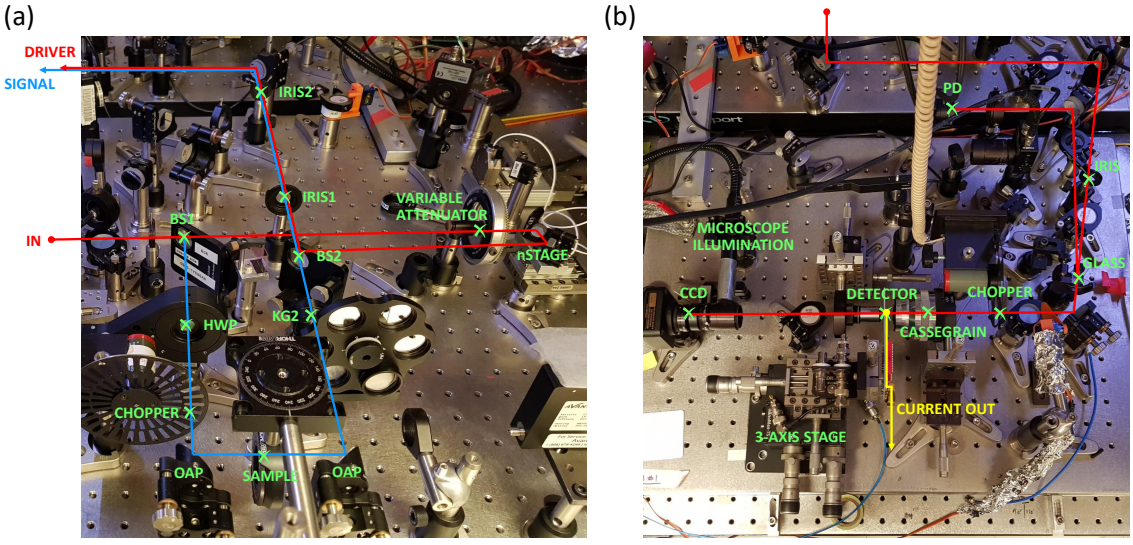

Figure 6-5: Photograph of the interferometer (a) and detection (b) stages. The different components comprising the stages are highlighted as well as the beam paths.

Fig. 6-5 illustrates the interferometer and detection stages.

To measure the signal, the laser is focused onto a nanoantenna array, whose electrodes are wire-bonded to the PCB. The current signal from the PCB is sent first to a transimpedance amplifier (FEMTO DDPCA-300) and then to a lock-in amplifier (connected to the chopper in the signal arm) to isolate the signal modulation from the driver background. The output of the lock-in amplifier is then sent to an oscilloscope whose acquisition windows are synchronized with the movement of the delay stage. The whole acquisition system is controlled by a PC, where the data is also saved at the end of each delay scan.

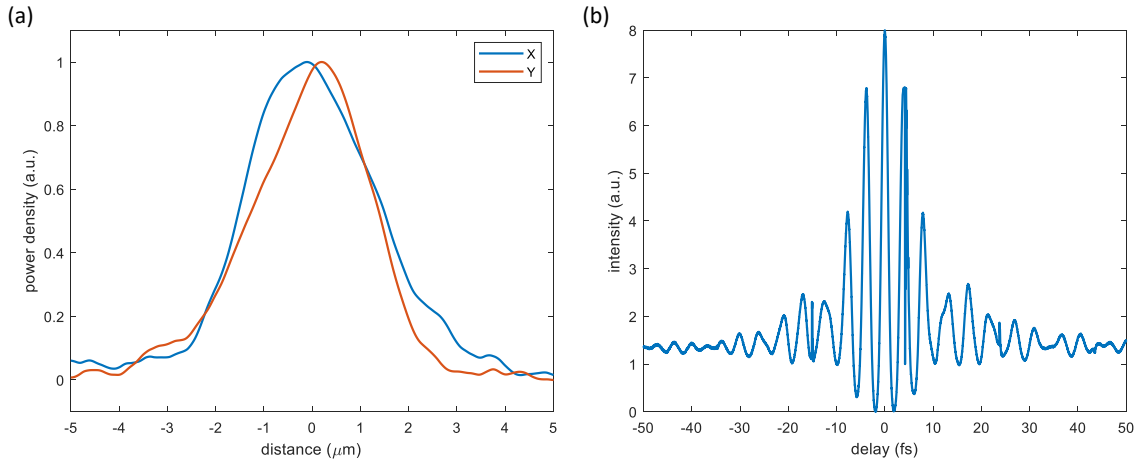

Figure 6-6: Beam characterization. (a) Result of a knife-edge measurement performed at the detector plane to characterize the beam size and astigmatism. This measurement shows a non-stigmated beam of 3.5 µm diameter. (b) Interferometric autocorrelation (IAC) measurements to optimize the pulse length. This was done by placing a BBO at the detector position and measuring the fringes of the SHG signal with a photodiode. Then the second prism compressor was tuned while maximizing the peak-to-background ratio, which would correspond to the condition of best compression. A result of approximately 1:7 was achieved which corresponds to a 2.5 cycles or 10 fs pulse.

The focus size at the detector position (i.e. at the focal position where the nanoantenna array chip would go) was then measured by performing a knife-edge measurement in X and Y directions. This measurement consists in moving an edge into the beam path while measuring the intensity on a photodiode. The result of this measurement is shown in Fig. 6-6a. In order to tune the pulse length, an interferometric autocorrelation (IAC) measurement was performed. This was done by placing

a BBO at the detector position and measuring the fringes of the SHG signal with a photodiode. Then the second prism compressor was tuned while maximizing the peak-to-background ratio, which would correspond to the condition of best compression. The result of this measurement is shown in Fig. 6-6b.

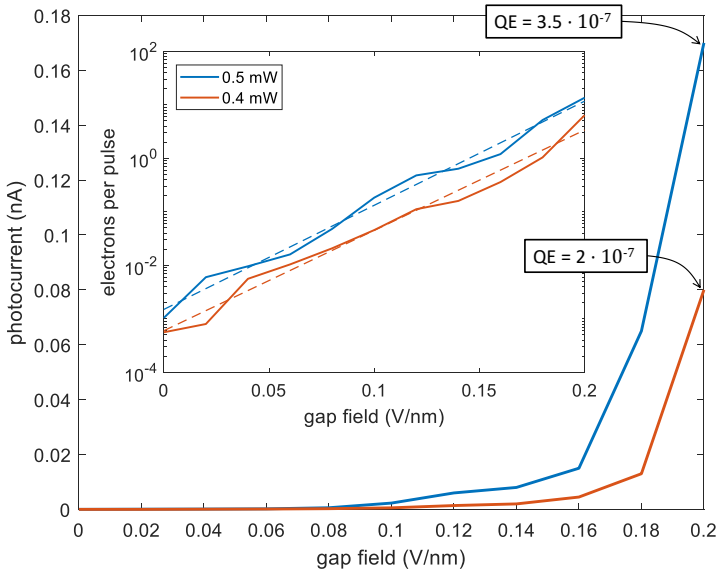

Figure 6-7: Photoresponse as a function of bias field. The result shows that exponential gain in optical sensitivity is achieved with the tuning of the bias field between emitter and collector. The measurement was carried out for two different laser powers, 0.4 mW and 0.5 mW, and resulted in a max quantum efficiency $QE = 3 \cdot 10^{-7}$. The inset shows the same data on a logarithmic scale.

The responsivity of the detector itself can also be measured by shining the laser on top of the array and measuring the resulting photocurrent while chopping on the common path to get rid of the background. The bias can also be adjusted by looking at the increase in the photoresponse. Fig. 6-7 shows an example of the increase of the photoresponse with the bias for two different power levels. This is a direct experimental demonstration of the principle elaborated in Chapter 5. Of course, the optimal bias level to perform sampling is not going to be dependent only on the photocurrent level but also on whether the noise associated with than photocurrent is lower than the photocurrent produced by the small signal. This optimal point can be found empirically by performing multiple sampling scans at different bias levels.

6.4 Reference Pulse Characterization

To demonstrate the validity of a sampling measurement it is necessary to compare it to a reference of the same signal measured with an alternative method. This can be done through an indirect method, measuring the amplitude and phase of the signal separately and then reconstructing it. The spectral amplitude can be measured easily using an optical spectrum analyzer (OSA). The phase instead can be reconstructed through Two-Dimensional Spectral Shearing Interferometry (2DSI)[115, 116].

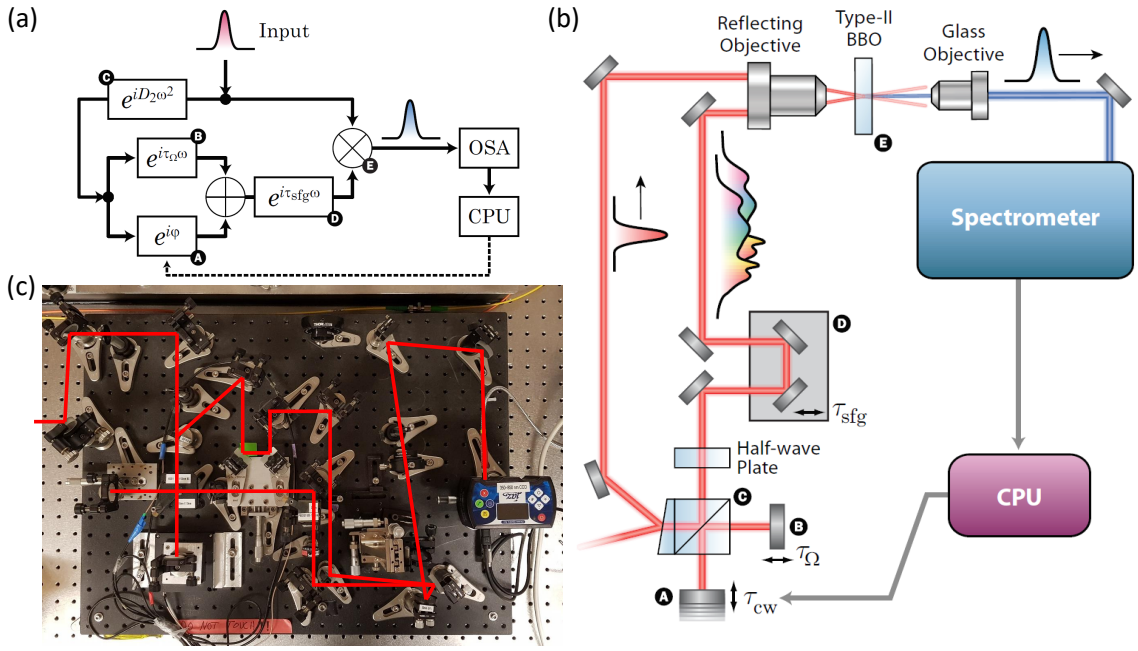

Figure 6-8: Two-Dimensional Spectral Shearing Interferometry (2DSI) setup. (a) Block diagram of the 2DSI process from [116]. (b) Schematic of the 2DSI experimental setup from from [116]. (c) Photograph of the experimental setup used for this measurement.

2DSI is a technique that allows measuring the spectral group delay by looking at the interference between two copies of the pulse under measurement, spectrally shifted with respect to each other. This principle is common for all spectral shearing methods such as SPIDER [117], however, in 2DSI this is achieved without introducing a delay between the two pulse copies (which creates dispersion), making this method much more stable, requiring less careful calibration, and being especially suitable for very short pulses. More detail on the theory can be found in [118].

The 2DSI setup is illustrated in Fig. 6-8. This measurement can be performed first by splitting the beam into two arms using a wedge (approximately 4% and 96%). The 4% arm is sent directly to a BBO crystal. Instead, the 96% arm is first sent to a Michelson interferometer where a beam splitter split the beam into two and chirps them into two quasi-CW beams. The length of one of the interferometer arms is controlled using a micrometer stage (path B in Fig. 6-8b). This arm length is going to set the shear frequency Ω. The other interferometer arm is sent to a delay stage that is used to scan the delay τ_{CW} (path A in Fig. 6-8b). Both the arms of the interferometer are then recombined at the beam splitter and then sent to the BBO crystal. In this path, another delay stage is also positioned to adjust the delay τ_{sfg} to obtain temporal overlap at the crystal. Then the signal is upconverted in the nonlinear crystal to a signal of frequency $\omega = \omega_0 + \omega_{UPconv}$, and is sent to a spectrometer. The intensity on the spectrometer is going to be:

$$I(\omega) = \left|A(\omega) + A(\omega-\Omega)e^{i\varphi}\right|^2 = 2|A(\omega)A(\omega-\Omega)|\cos(\varphi + \phi(\omega) - \phi(\omega-\Omega)) + D.C. \tag{6.8}$$

where $\phi(\omega) - \phi(\omega-\Omega) = \tau_g(\omega - \Omega/2)\Omega + O[\Omega]$, and τ_g group delay. Hence, if you sweep φ with the stage and you know the upconversion frequency ω_{UPconv} and the shear frequency Ω you can retrieve the group delay τ_g.

To evaluate ω_{UPconv} and Ω, two spectrograms are acquired while scanning the delay with and without placing in the path a 1.5mm of Fused Silica (FS) which introduces a known group delay shift. The two spectrograms are shown in Fig. 6-9. Then $\tau_g(\lambda)$ is calculated exploring different values of the ω_{UPconv} and Ω parameter space. For each of these assumed ω_{UPconv} and Ω the RMS of the difference between the retrieved $\tau^*_{gFS} = \tau_g[w/FS] - \tau_g[w/oFS]$ and the known τ_{gFS} introduced by the fused silica is calculated. Then the point in the parameter space that minimizes the error is selected. This represent the optimal point, which in this case corresponds to $\lambda_{UPconv} = 1050nm$ and $f_\Omega = 5.5THz$. This optimization process is illustrated in Fig. 6-10.

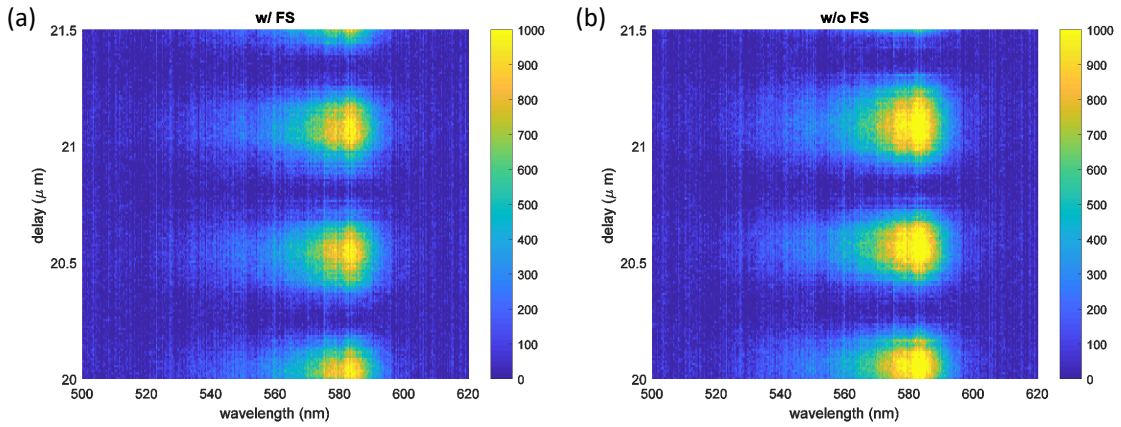

Figure 6-9: 2DSI Spectrograms with (a) and without (b) a 1.5mm of fused silica in the beam path. These spectrograms are acquired by scanning the delay stage in the Michaelson interferometer while acquiring a spectrum at each step.

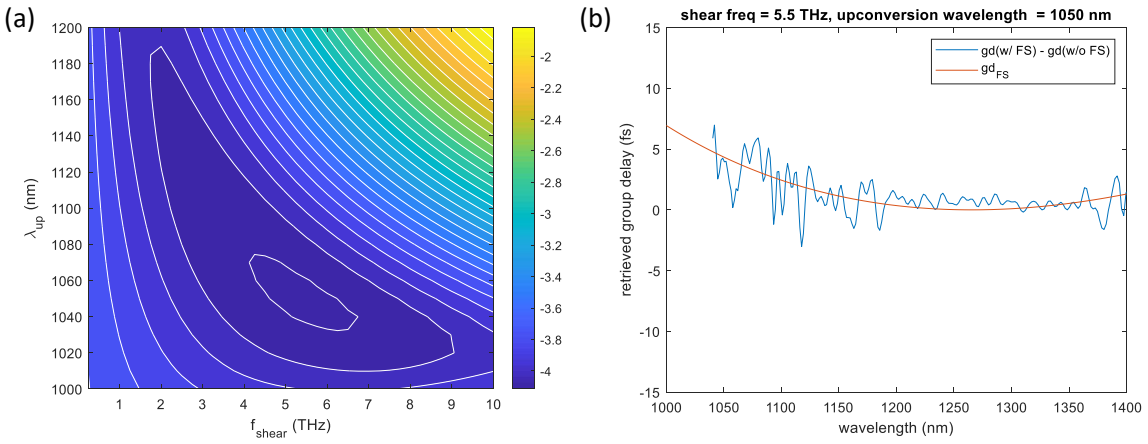

Figure 6-10: Retrieval of ω_{UPconv} and Ω. (a) Color plot illustrating the exploration of the ω_{UPconv} and Ω parameter space. The different colors corresponds to different values of the RMS of the difference between the retrieved $\tau^*_{gFS} = \tau_g[w/FS] - \tau_g[w/oFS]$ and the known τ_{gFS} introduced by the fused silica. (b) Plot of the the retrieved τ^*_{gFS} and the known τ_{gFS} introduced by the fused silica for the optimal value of plot (a): $\lambda_{UPconv} = 1050nm$ and $f_\Omega = 5.5THz$.

Knowing λ_{UPconv} and f_Ω allows you to back-calculate the group delay $\tau_g(\lambda)$ of the incident pulse from the spectrogram. Fig. 6-11 is a plot showing on the same graph the pulse group delay retrieved from this 2DSI measurement and the spectral amplitude of the pulse. It is worth noting that while the spectrum can significantly change from day to day the group delay is expected to remain stable over time.

Finally, from the group delay τ_g the phase ϕ can be easily calculated knowing that

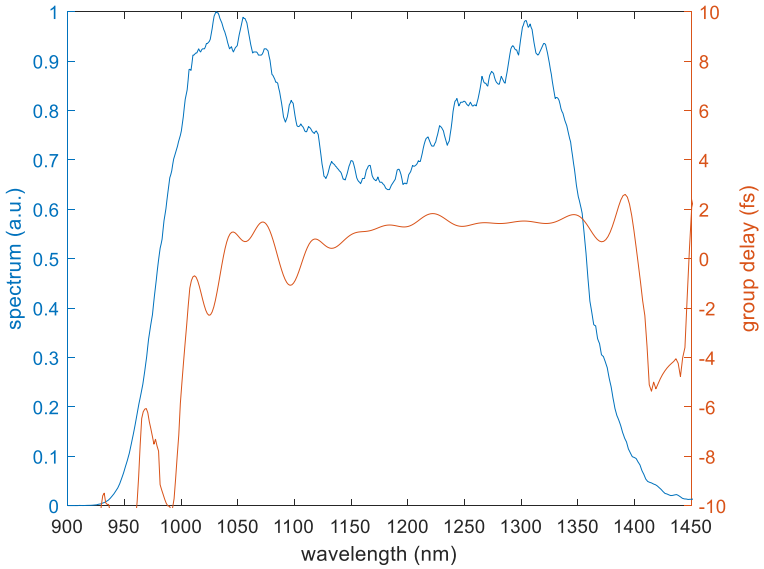

Figure 6-11: Full spectral information. (a) Spectral amplitude measured with an optical spectrum analyzer (OSA). (b) Group delay retrieved through two-dimensional spectral shearing interferometry (2DSI) measurement.

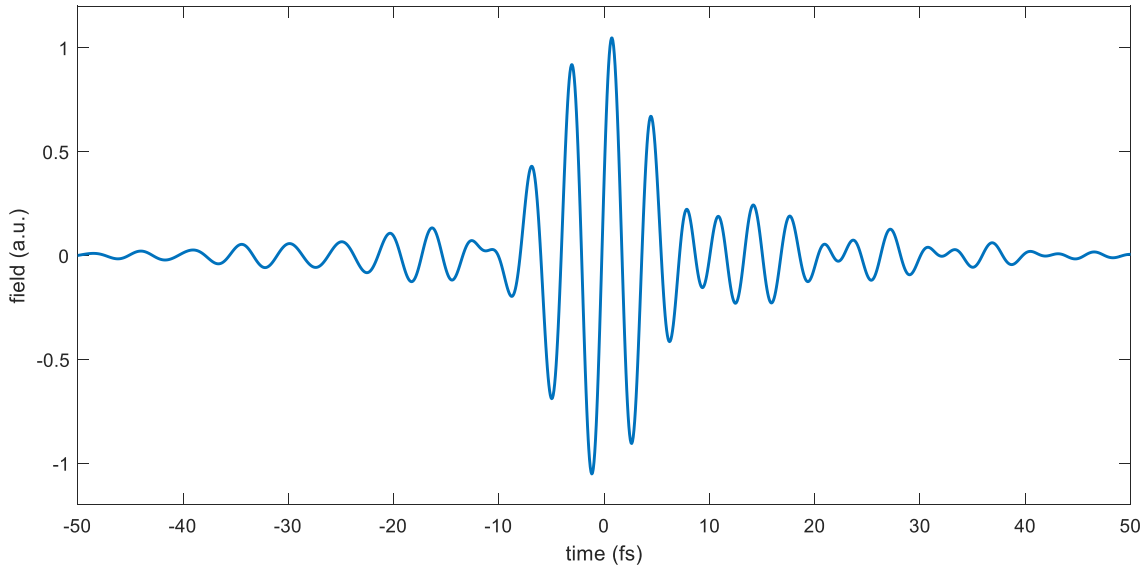

Figure 6-12: Reconstructed time-domain evolution of the field.

the two are related as follows:

$$\tau_g = \frac{\partial \phi}{\partial \omega} \tag{6.9}$$

Then, amplitude $E(\omega)$ and phase $\phi(\omega)$ can be put together to evaluate the tem-

poral evolution of the optical field as:

$$E(t) = \mathcal{F}^{-1}\left(E(\omega)e^{i\phi(\omega)}\right) \tag{6.10}$$

Fig. 6-12 illustrates the resulting retrieved evolution of the field. This retrieval method can be used to calculate the reference to be used as a comparison with the value obtained through optical field sampling with plasmonic nanoantennas, to demonstrate its validity and precision.

6.5 Optical Field Sampling Experimental Demonstration

The experimental demonstration of field sampling is then carried out by placing an ND4 filter in the sample arm to ensure the validity of the small-signal approximation as well as to test the sensitivity of this technique. Then with the help of the microscope, the laser is placed on the array. Then the PCB position in X, Y, and Z is adjusted with a 3-axis stage to place the nanoantenna array at the correct focal position and to find a spot of the array with the optimal response. This condition is achieved by connecting the lock-in to a chopper placed in the common path instead of in the signal arm, and maximizing the current response while scanning the stage. Then the bias is also optimized with the same method. Once the desired response is achieved, the lock-in amplifier reference is switched from the chopper in the common path to the one in the signal arm, and the sampling measurement can proceed as described in Section 6.3.

The field measured using this method, as described in Section 6.1, is mediated by the transfer function of the nanoantenna. Hence, to calculate the appropriate reference the plasmonic response has to be incorporated. Such response was simulated in COMSOL by Dario Cattozzo Mor, and the dephasing deriving from it is shown in Fig. 6-13a. This dephasing is a result of the resonant electron dynamics excited within the nanoantennas. Once the reference is calculated, it can be compared with

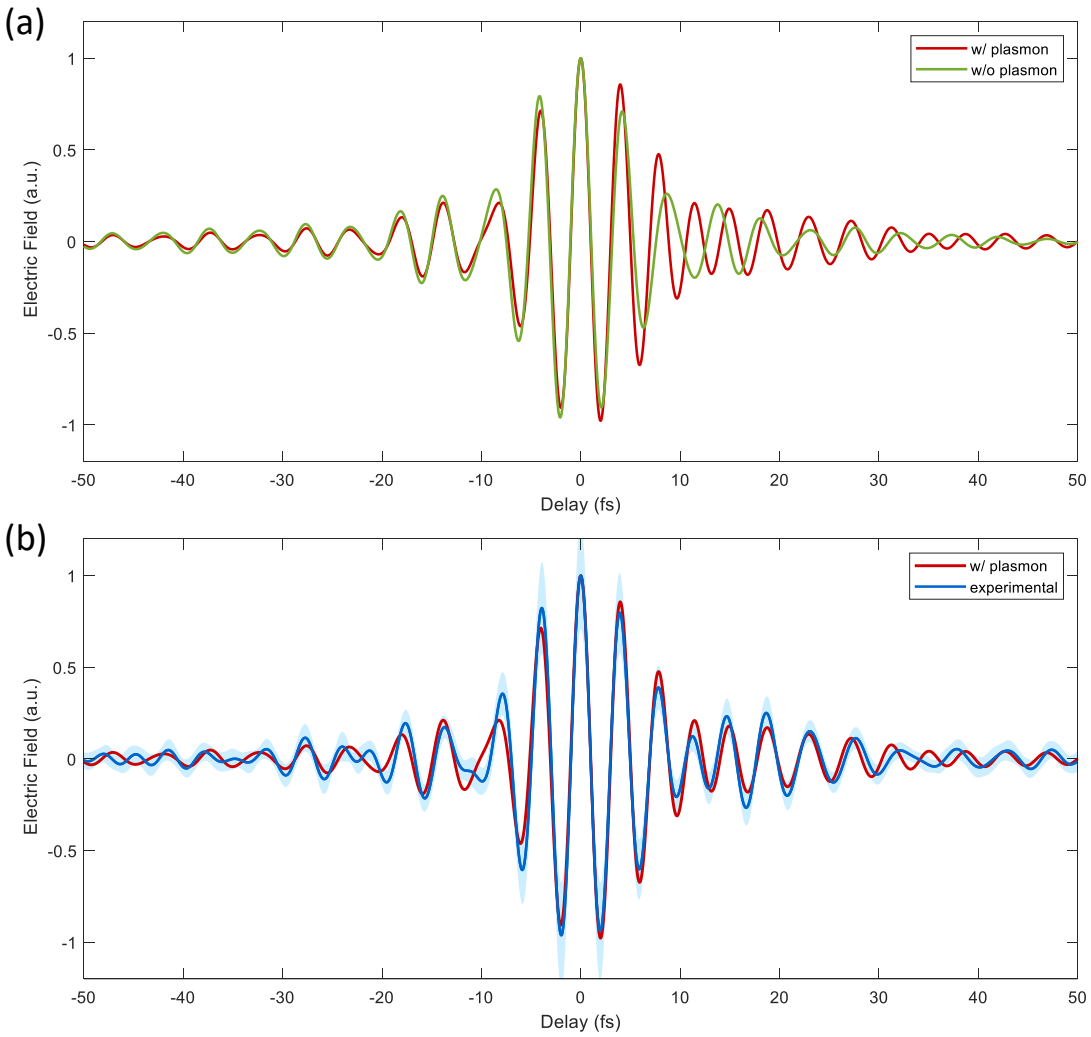

Figure 6-13: Time-domain results for devices with a height of 240 nm. (a) Reconstructed time-domain evolution of the field calculated from the spectral amplitude from the OSA and the phase from a 2DSI measurement (green), and the same field once the plasmonic response of the nanoantenna is incorporated (red). (b) Comparison between the calculated time-domain evolution of the field (red, including the plasmonic response) and the experimental one measured through optical field sampling (blue). The 1σ-confidence interval is shown as a blue shaded ribbon centered around the average value (blue solid line) retrieved from 60 scans. The peak field strength is calculated to b 6.4 MV m^{-1}.

the field sampling measurement obtained as described in Section 6.3. The result of this comparison is shown in Fig. 6-13b. This measurement was performed by evaluating the average over 60 scans. As can be clearly appreciated in the figure, there is a great adherence between the expected and the measured field.

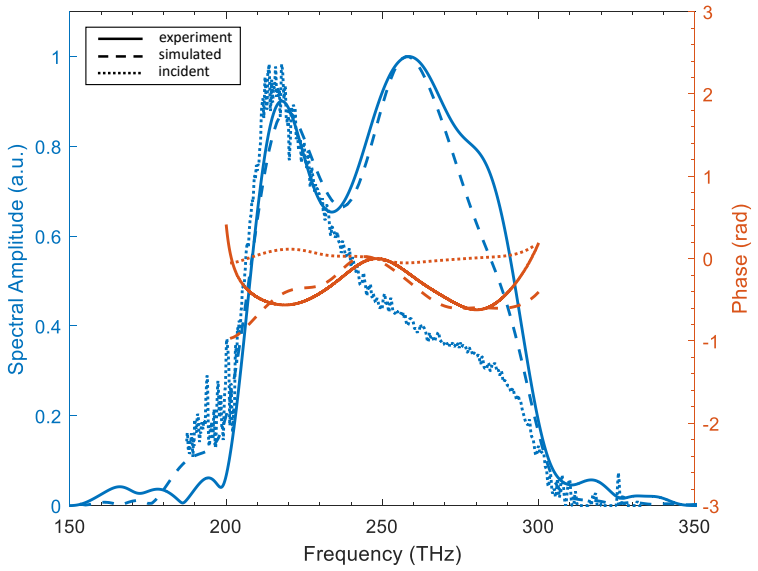

Figure 6-14: Frequency-domain comparison of measured (solid), simulated (dashed, including the plasmonic response) near-fields for devices with a 240 nm height, and the reconstructed incident laser field (dotted). The measured data agree very well with the expected simulated curve. Both cases exhibit two peaks, corresponding to the measured spectrum of the incident field (at 218 THz) and the plasmonic enhancement of the antenna (at 257 THz), respectively.

The same comparison can be done in the frequency domain, taking the Fourier transform of the sampling trace. This comparison is shown in Fig. 6-14, where the amplitude and phase of the signal are plotted on the two vertical axes. Here the contribution of the plasmon is even clearer, as it emerges as a peak at 257 THz. As can be seen, there is a close match between the simulated peak and the measured one.

The nanoantennas used in this measurement have a triangular shape with a base of 180 nm and an altitude of 240nm. These dimensions set the resonance frequency of the plasmon to be at 257 THz.

Studies of the average photocurrent were also performed to verify the operating regime of the devices. Fig. 6-15 shows results from a set of 240 nm devices similar to those used in the main text. We note that this scan was not performed on the exact set of devices used for optical field sampling measurements to avoid device reshaping at the highest intensities. The results indicate a photocurrent power-law scaling of

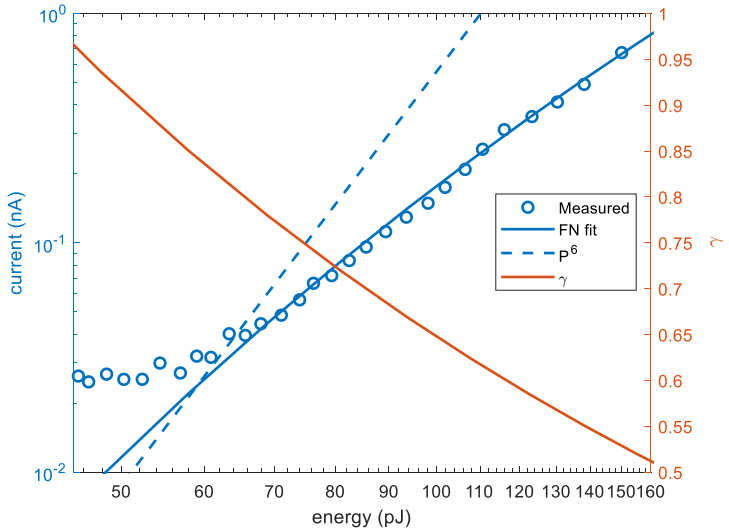

Figure 6-15: Measurement of average photocurrent as a function of incident pulse energy. These measurements were performed on a nominally similar set of 240 nm devices to those used for optical field sampling. A Fowler-Nordheim fit (solid line) is shown indicating emission that scales approximately as $I \propto P^{3.5}$ over the measured pulse energy range. For reference, the dashed line shows $I \propto P^{6}$ which is similar to the observed multiphoton power-law scaling rate from similar structures characterized in [84]. The Keldysh parameter γ (red line) is also calculated in the same energy range.

$I \propto P^{\sim 3.5}$, where P is the incident pulse energy. Multiple scans were performed showing power-law scaling rates ranging from $I \propto P^3$ to $I \propto P^4$ over the measured range of pulse energies. The experimental results fit very well to a quasi-static Fowler-Nordheim photoemission model which is shown as the solid blue curve in Fig. 6-15 assuming a field-enhancement of ≈ 20 in the time domain. This field enhancement is an excellent match to that predicted by our electromagnetic models. For comparison, in Fig. 6-15, it is also shown a power-law scaling reference line for $I_{\mathrm{MP}} \propto P^6$ which is comparable to the experimentally observed multiphoton scaling rate from similar devices in prior work with similar material and resonance properties [84]. The peak field from the quasi-static Fowler-Nordheim fit was also used to calculate the expected Keldysh parameter γ, finding that $\gamma < 1$ over the entire range of intensities as would be expected for optical-field tunneling. Importantly, we find that $\gamma \approx 0.9$ at 50 pJ which was the operating point of the driving field used for the sampling measurements.

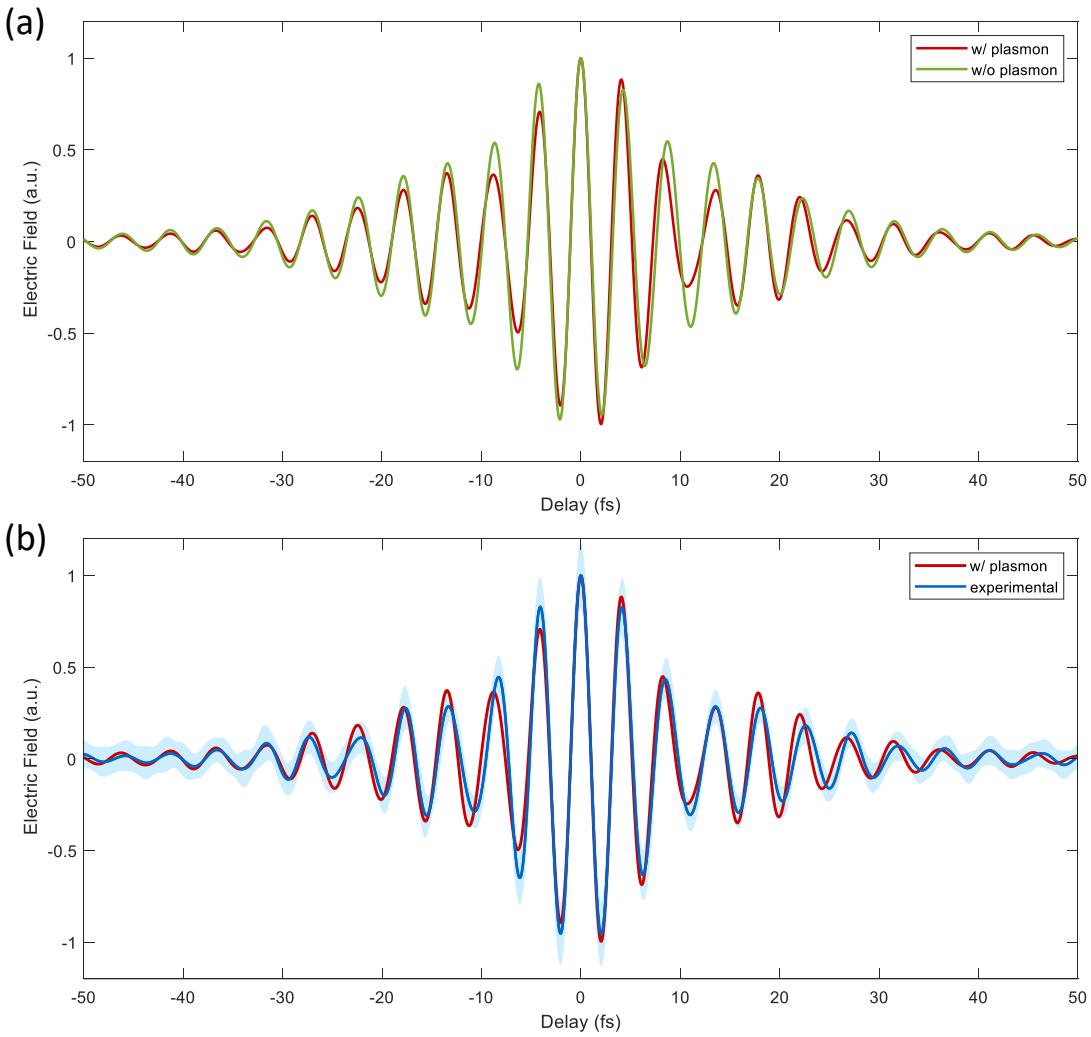

Figure 6-16: Time-domain results for devices with a height of 200 nm. (a) Reconstructed time-domain evolution of the field calculated from the spectral amplitude from the OSA and the phase from a 2DSI measurement (green), and the same field once the plasmonic response of the nanoantenna is incorporated (red). (b) Comparison between the calculated time-domain evolution of the field (red, including the plasmonic response) and the experimental one measured through optical field sampling (blue). The 1σ-confidence interval is shown as a blue shaded ribbon centered around the average value (blue solid line) retrieved from 47 scans.

If the measurement is repeated with different nanoantenna geometry the plasmon contribution can be shifted in frequency. This effect is shown in Fig. 6-16, where antennas with the same aspect ratio but an altitude of 200 nm were used. In this situation, as can be seen from Fig. 6-16a, the dephasing due to the plasmon is minimal. Also in this case, the optical field sampling using plasmonic nanoantennas

is able to successfully capture the expected field.

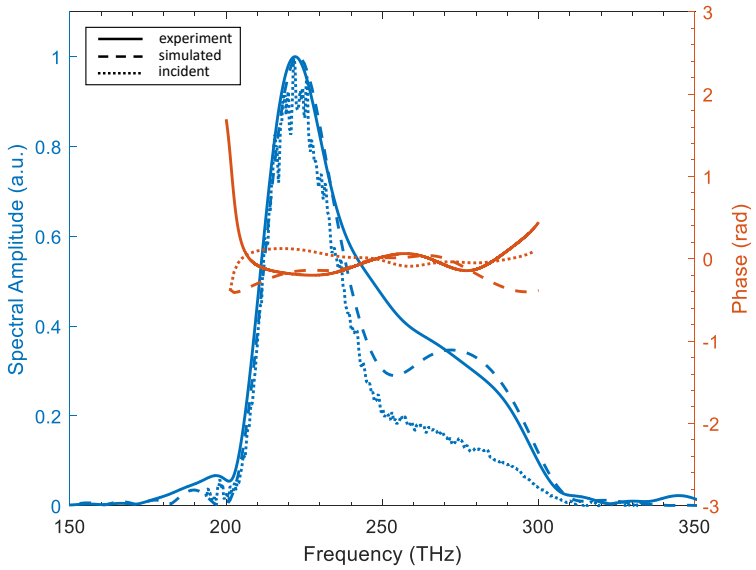

Figure 6-17: Frequency-domain comparison of measured (solid), simulated (dashed, including the plasmonic response) near-fields for devices with a 200 nm height, and the reconstructed incident laser field (dotted). The measured data agree very well with the expected simulated curve. Both cases exhibit one main peak, corresponding to the measured spectrum of the incident field (at 220 THz). In fact, in this case, the plasmon excitation is off-resonance.

The same effect can be seen in the frequency domain, portrayed in Fig. 6-17. As can be seen in this picture, the plasmon peak is much smaller and shifted to higher frequencies, and closely match the simulation result.

From these results it can be concluded that this technique can be successfully used to measure very weak fields in the time domain with attosecond resolution, with energies of the order of a few fJ, 6 orders of magnitude lower than the competing state of the art[102, 96, 66, 97, 98]. Such a compact platform that enables sub-cycle, field-sensitive detection of low-energy optical waveforms for phase-resolved spectroscopy and imaging, devices similar to those discussed here could find applications in a variety of areas such as biology, medicine, food safety, gas sensing, and drug development.

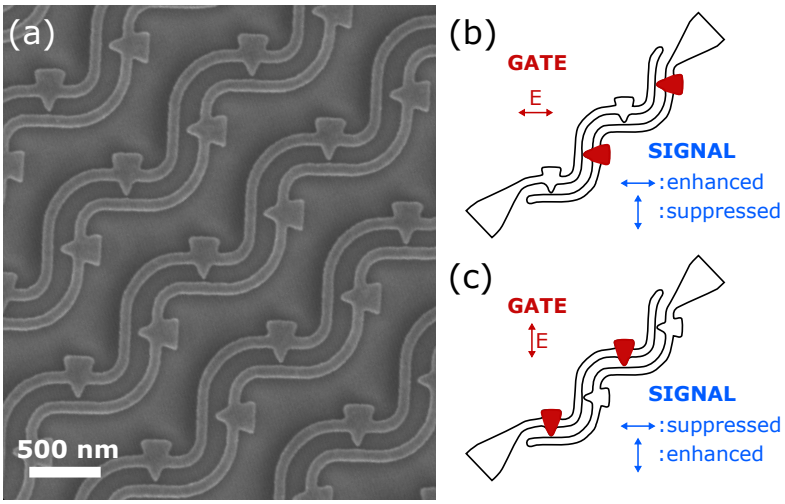

Figure 6-18: Polarization sensitive detection. (a) SEM micrograph of the proposed polarization-sensitive detector showing an array of meandering electrodes where one set of detectors is oriented perpendicularly to the other set. (b-c) Schematic of the detection scheme illustrating how a gate signal can be used to enhance all the signals polarized parallel to the gate and suppress all the signals perpendicular to it. This scheme allows to select the polarization of interest and potentially, through multiple measurements can be used to fully reconstruct an unknown signal in terms of frequency, phase, and polarization information.

6.6 Polarization Sensitive Detection

A detector can also be designed so that it can be gated to be sensitive to different polarizations. This can be achieved by having sinusoidal electrode strips and placing nanoantennas with perpendicular orientation on each electrode, as shown in Fig. 6-18a. When a gate pulse is hitting the device with a polarization parallel to one of the two antennas orientations, it is going to enhance signals with the same polarization and suppress signals with perpendicular polarization, as illustrated in Fig. 6-18b,c.

This detector sensitivity was studied by rotating the polarization of an input pulse, which shows a sinusoidal behavior with peaks and valleys at the positions corresponding with one of the two antenna orientations. This experiment was done by illuminating the nanoantenna array with a single beam and recording the photocurrent while progressively rotating a half waveplate placed in the beam path. The result is portrayed in Fig. 6-19. In this graph peaks and valleys corresponds to the polar-

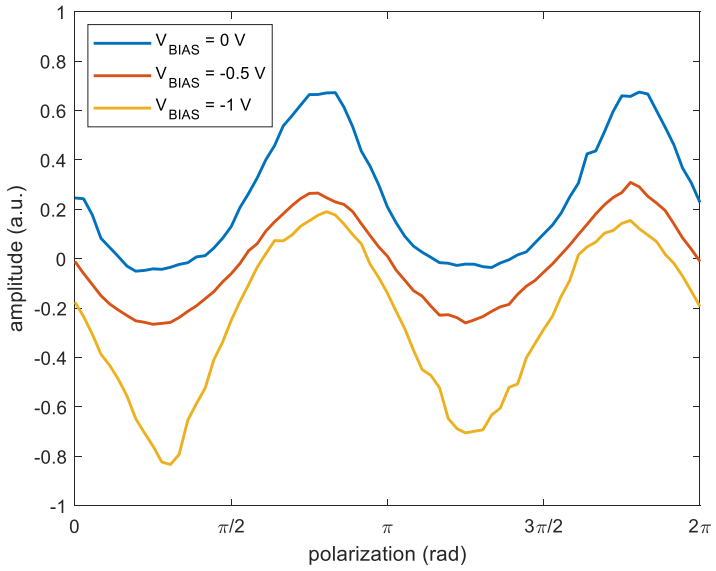

Figure 6-19: Study of the dependence of the photocurrent with the polarization of an incident pulse. The study is performed at different bias levels demonstrating that the detection curves can be shifted up and down so to find the optimal condition of operation. The 0 rad polarization corresponds to the situation when the beam is perpendicular to the lead's direction (i.e. it is 45 degrees with respect to both electrode orientations as depicted in Fig. 6-18a.).

izations at which the beam is parallel to one or the other nanoantenna orientation (the 0 rad polarization is when the beam is perpendicular to the lead's direction). It was also shown that the sensitivity curves can be translated up and down with the application of an external DC bias. This can be used to select the optimal operation condition as well as to build a balanced detector that could be used to reduce the background, therefore improving the signal to noise.

The polarization sensitivity of the device was also demonstrated experimentally by performing an autocorrelation measurement with the driver parallel to one of the two nanoantenna orientations and the signal parallel or perpendicular to the same direction, respectively. The result of this measurement is shown in Fig. 6-20. As can be clearly seen in this plot, when both driver and signal are polarized parallel to one of the nanoantenna orientations the device is sensitive to the signal. On the other hand, when the two are perpendicular, the signal response is suppressed.

Therefore, this geometry can be used to build a polarization-sensitive detector,

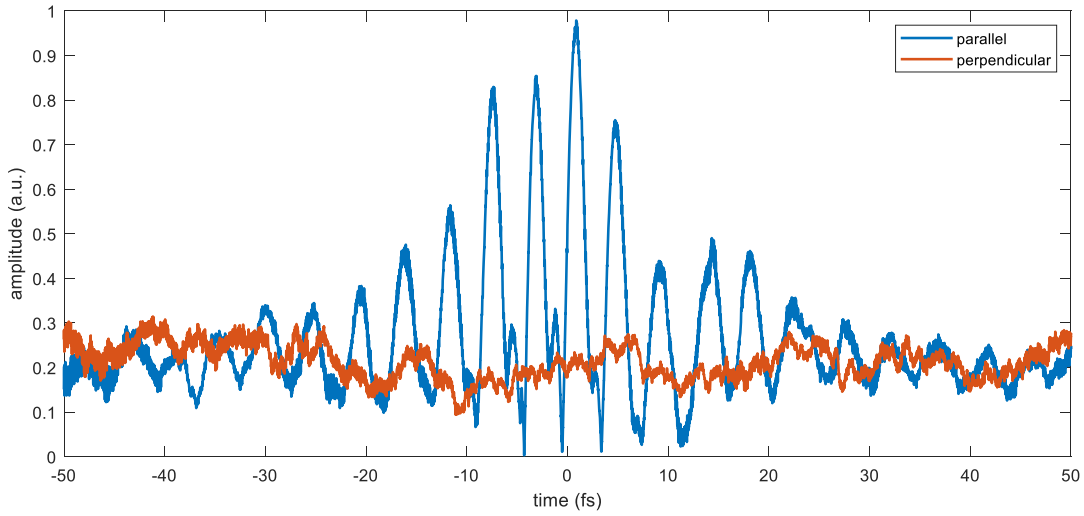

Figure 6-20: Polarization sensitive experimental demonstration. Cross-correlation measurement with the polarization-sensitive detector showing the measured signal in enhanced condition, that is to say when both gate and signal are parallel to one of the nanoantenna orientations (blue), and in suppressed condition, that is to say when gate and signal are perpendicular with each other and each is parallel to a different nanoantenna orientation (red). As clear from the graph the detector is indeed only sensitive to the polarization direction of the gate. This measurement was performed with an ND3 filter in the signal arm.

that can be used to study not only the time evolution of a signal, and so its frequency and phase information, but also its polarization. Future work should include the study of a circularly polarized signal and then measuring the components of the field projected onto the X and Y polarization, and then proceed to reconstruct the full 4-dimensional field evolution.

6.7 Hot Electrons

A key aspect of the ultrafast plasmonic response of these devices is their transient response, which is dependent on the dynamics following the excitation of hot electrons in the system.[119] Studying this transient response is key to understanding the correspondence between the optical dynamics of the field and the carriers' dynamics in the material, which is fundamental to designing proper petahertz electronics since this could set speed limitations at different power and field levels. In fact, one of

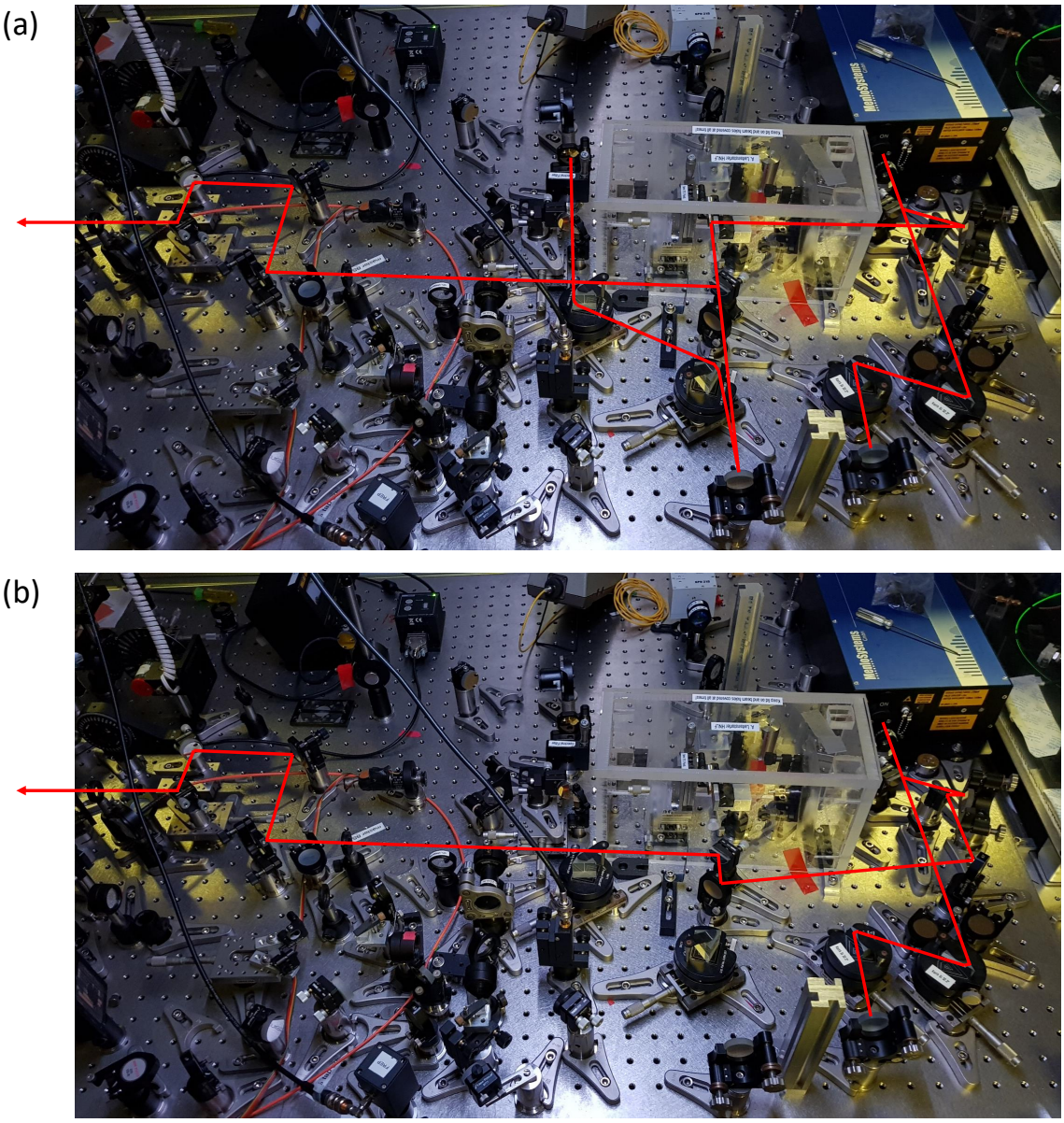

Figure 6-21: Experimental setup highlighting the beam path when the 1170 nm supercontinuum (a) or the 1550 nm is sent to the interferometer stage.

the reasons why the Au devices are more suitable for the aforementioned sub-cycle optoelectronics applications is that carrier dynamics in Au are faster than in most materials such as TiN. [28, 120, 121] Therefore, in this work, the generation of hot electrons in gold nanoantennas was studied.

It is important to note that to perform this measurement the hot electrons excitation in the nanoantennas has to be performed with a pulse orthogonally polarized with

respect to the nanoantenna orientation to ensure that this pulse does not contribute to photoemission. The detection instead, has to be performed using a pulse polarized parallel to the nanoantenna orientation, as will be discussed in the following.

The study was performed using two different laser pulses to excite the electron population in the nanoantennas. The first measurement was performed using the 1170 nm supercontinuum source already employed for the sampling measurements. The second one was done picking off the 1550 nm pulse in the same setup before the supercontinuum generation. This was made possible by inserting removable mirrors and flip mirrors in the setup so as to be able to switch back and forth between the two configurations. Fig. 6-21 illustrates the beam path in both configurations.

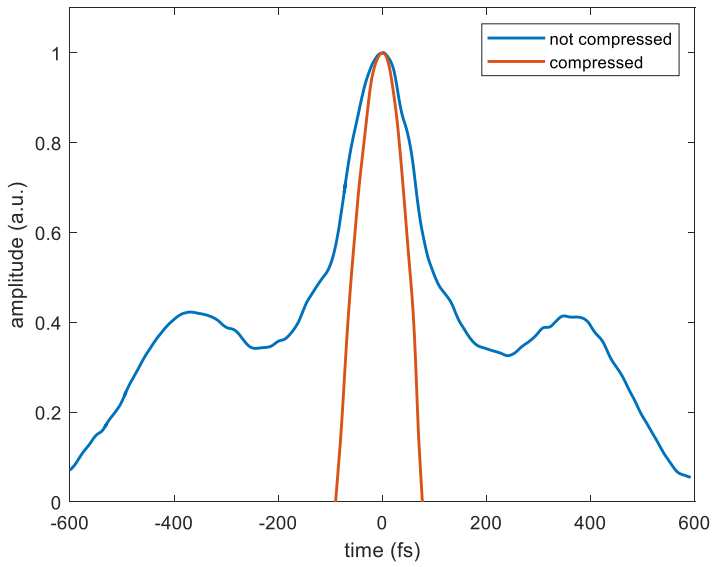

Figure 6-22: Autocorrelation measurement of the 1550 nm pulse before and after compression through the prism compressor stage. This measurement was performed using a pulseCheck.

The 1550 nm was picked off after the prism compressor in order to have control over the beam length. Fig. 6-22 shows an autocorrelation measurement performed with a pulseCheck of the pulse before and after compression. Before compression, the autocorrelation trace shows a FWHM of 216 fs, which, assuming a Gaussian pulse, corresponds to a pulse duration of $216/\sqrt{2} = 152$ fs. After the compression, the autocorrelation trace exhibits a FWHM of 117 fs, which corresponds to a pulse

duration of 82 fs. As mentioned in Section 6.3 the first is a 200 pJ pulse, while the second one is a 5 nJ pulse.

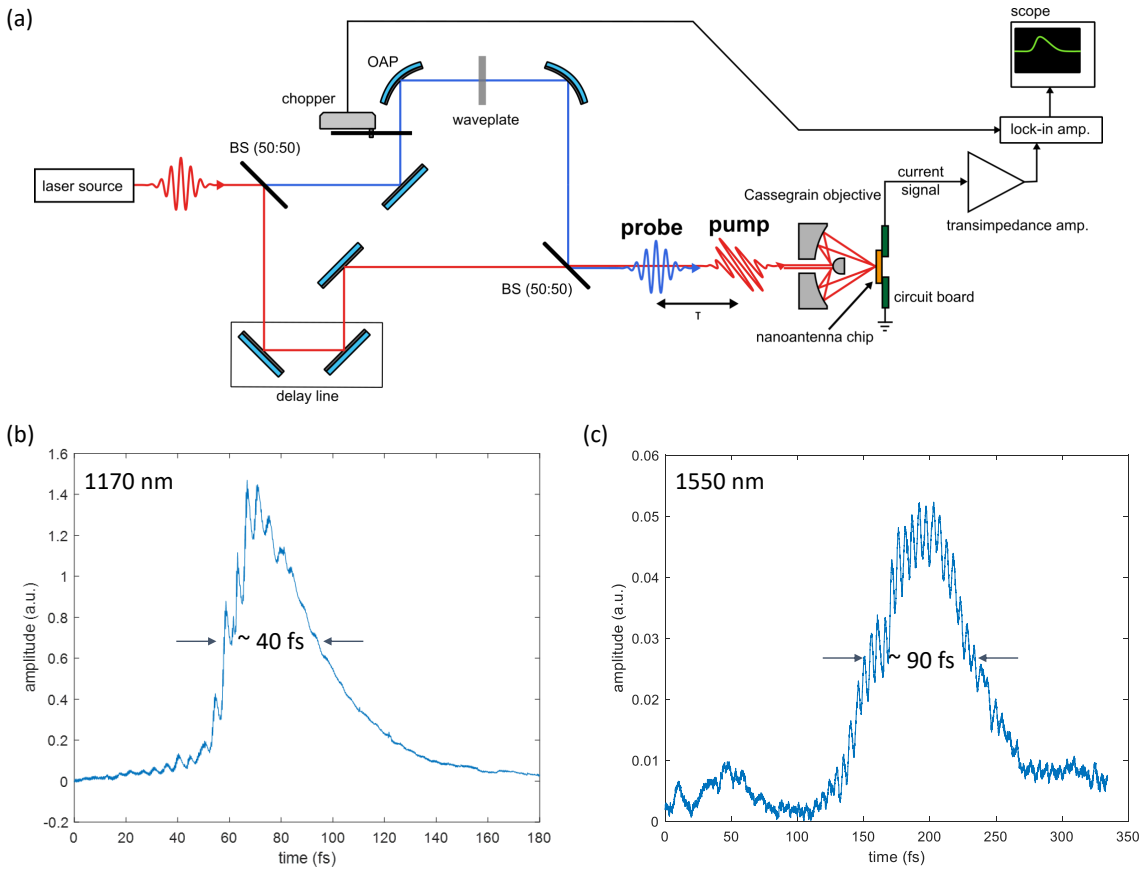

Figure 6-23: Hot electron dynamics characterization. (a) Experimental setup used for the characterization of the hot electron dynamics using a pump-probe detection scheme. The pump and the probe are rotated 90 degrees with respect to each other so that only the probe is oriented in the nanoantenna direction. (b) Result of the pump-probe experiment showing the hot electron dynamics using the 1170 nm supercontinuum pulse. (c) Result of the pump-probe experiment showing the hot electron dynamics using the 1550 nm pulse.

To investigate this mechanism a pump-probe experiment was performed. A laser pulse was shined on the detector polarized orthogonal to the orientation of the nanoantennas (pump), which alters the ground state population over a very short period of time, creating hot electrons, and then the relaxation time was measured by scanning the delay of a second pulse (probe) polarized parallel to the nanoantennas orientation. The latter pulse generates an electron burst whose amplitude is going to be dependent

on the electron population density in the nanoantennas, effectively probing the hot electrons states, as shown in Fig. 6-23.

The result of this measurement obtained with the 1170 nm pulse is portrayed in Fig. 6-23b, and clearly shows an initial faster rise time of approximately 15 fs in which the hot electron states are populated, followed by a slower fall time tail with a time constant $\tau \sim 60$ fs, in which the states are depopulated once again. When a longer higher power pulse is employed (the 1550 nm one), the shape of the measured pump-probe response changes. In fact, in this case, the response looks more symmetric. This is attributed to the fact that, since the pulse is longer than the relaxation time of the hot electrons, along with the duration of the pulse the hot electron states have time to be excited and then relax, and then be excited once again. The result is a convolution of all of these excitations which appears as a more symmetric current signal.

This analysis is going to be very beneficial when defining the speed limitation of future petahertz electronics. Moreover, these results highlight the need for few-cycle excitation. Otherwise, for longer pulses, one can excite carrier dynamics that dynamically alter emission from one side of the pulse to another. Future work should include the extension of these analyses to different powers and different nanoantenna materials.

6.8 Sampling of a Second Harmonic Pulses

In this section, the initial work done towards the demonstration of sampling of second harmonics and the remaining steps are discussed.

An important characteristic of the sampling technique described in Section 6.5 is the extremely broad bandwidth. In fact, the sampling bandwidth is not set by the bandwidth of the driver, but by the bandwidth of the current burst from the emitter to the collector. And since this burst is generated through field emission, which is a strongly non-linear process, the sampling bandwidth can be extremely wide. In an ideal situation, the current burst would be a δ and you could sample any signal.

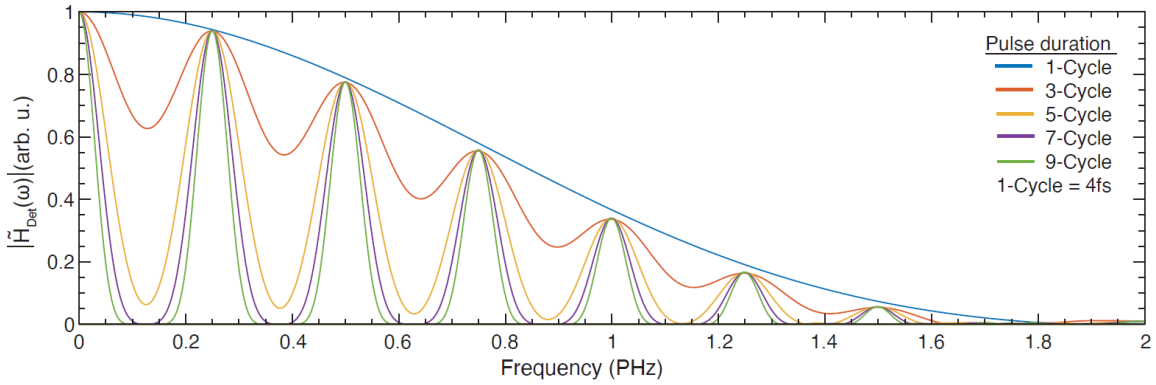

Figure 6-24: Calculation of the bandwidth of the sampling detection scheme for different values of driver pulse duration expressed in terms of the number of cycles in the envelope. With the increase in the number of cycles, there is a creation of dead spots in between harmonics in the bandwidth. This calculation was performed by Felix Ritzkowsky.

In reality, the burst is not a δ but it is still very sharp, and the bandwidth spans over a PHz. Another effect that needs to be taken into account is the fact that the driver pulse is short, but it is not single-cycle (for our supercontinuum source it is 2.5 cycles). This means that not only the main peak is going to contribute to the current, but the side peaks are also going to generate current bursts. This is going to create dead spots in the bandwidth. This effect was investigated by Felix Ritzkowsky and is illustrated in a calculation shown in Fig. 6-24. As can be clearly seen in this graph the bandwidth includes many harmonics of the fundamental, even when considering a driver pulse consisting of multiple cycles.

An elegant way to experimentally demonstrate that the bandwidth spans multiple harmonics is to use a driver at a certain central frequency to sample a signal at a harmonic frequency. In this section, some preliminary experimental work carried out to demonstrate second harmonic generation (SHG) sampling is reported. This approach involves placing a beta barium borate (BBO) nonlinear crystal[122] in one of the arms of the interferometer to generate the SHG signal, filtering out the fundamental and then sending the second harmonic together with the driver to the nanoantennas similarly to what was done for the sampling of the fundamental in previous experiments. A type-I (oo-e) BBO crystal is a non-linear optical medium that can be used for sum-

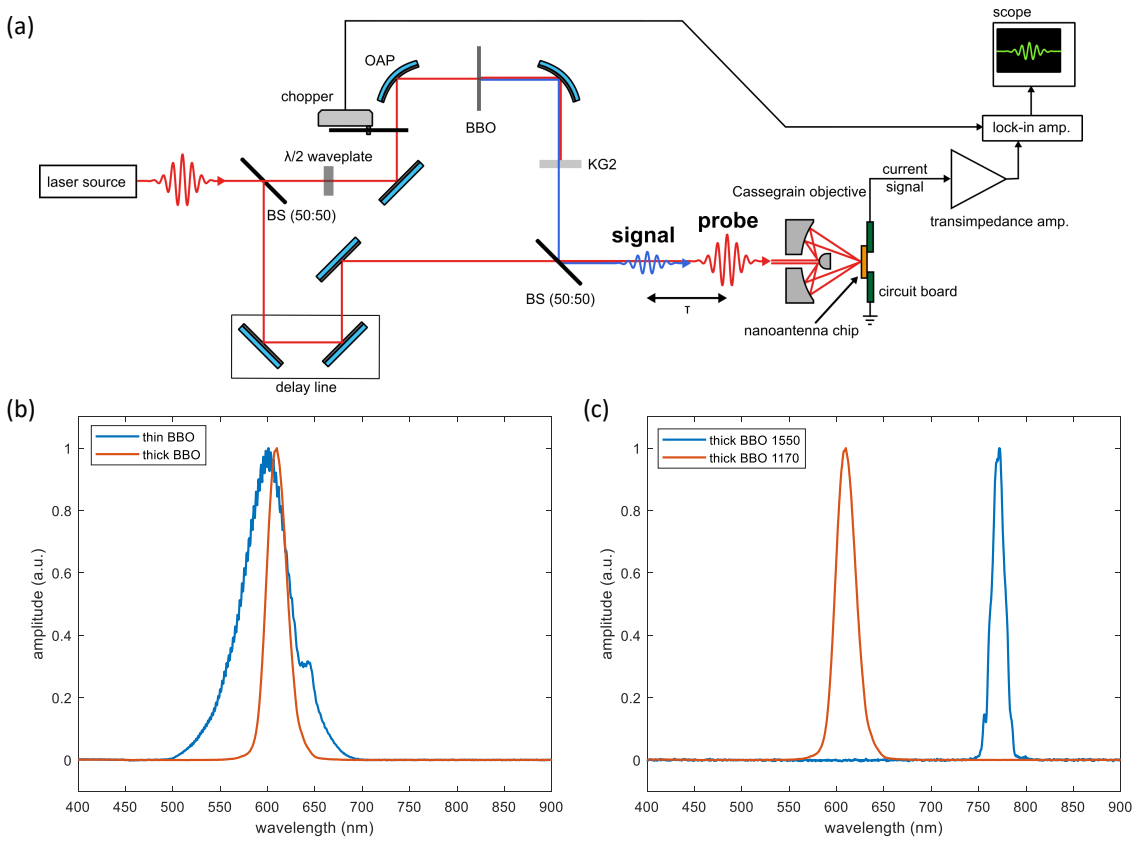

Figure 6-25: Sampling of the second harmonic. (a) Schematic of the experimental setup for the sampling of the SHG signal. The SHG signal is generated by a type-I BBO non-linear crystal. (b) SHG spectrum measured with an Avantes spectrometer using a thin (100 µm) and a thick (1 mm) BBO crystal. The thin crystal one has higher bandwidth but yields $\sim 1\,\mu W$, while the thicker one has a smaller bandwidth but yields $\sim 9\,\mu W$. (c) SHG spectrum measured with an Avantes spectrometer using a thick BBO using the 1170 nm supercontinuum source ($\sim 9\,\mu W$) or the 1550 nm source ($\sim 300\,\mu W$).

frequency generation exploiting its second-order non-linearity $\chi^{(2)}$, where a pump at ω can be used to generate an idler at ω with polarization parallel to the pump and a signal at 2ω with polarization perpendicular to the pump. The polarization rotation can be easily taken into account by introducing a half waveplate in the signal arm. The experimental setup that we are working on is illustrated in Fig. 6-25a. This setup is similar to that used for the normal field sampling except for the introduction of the BBO at the focal position of the OAPs, the introduction of the half waveplate to account for the polarization rotation, and the use of a KG2 glass to filter out the fundamental in the signal path.

The main challenges with this approach are:

1. generation of a sufficiently strong SHG signal that can be sampled;
2. spatial and temporal alignment of the SHG with the driver; and
3. nanoantenna design to be sufficiently sensitive to both the driver and the signal.

Regarding the generation of a sufficiently strong SHG signal, different avenues were investigated. The two main parameters to be considered are the thickness of the BBO and the selected driver frequency. In fact, the thicker the BBO, the more efficient the second harmonic generation but the more dispersive, that is to say, that a thicker crystal is going to yield more output SHG power but with a smaller bandwidth, hence a longer pulse. Since, for the same amount of power, a longer pulse entails a lower peak field and nanoantenna detectors are field sensitive, finding the optimal thickness is a trade-off. Fig. 6-25b illustrates the difference between the SHG signals generated by the 1170 nm source with a thin (100 µm) and a thick (1 mm) BBO crystal. It is clear that the thicker crystal has a smaller bandwidth. However, while the thin crystal yields $\sim 1\,\mu W$ of power, the thicker one yields $\sim 9\,\mu W$. Since these powers are significantly low, another option is to use the 1550 nm source (i.e. picking off the beam before the supercontinuum generation). When this is done the generated SHG is at a higher frequency (775 nm), which is beneficial because the nanoantennas exhibit higher field enhancement at those frequencies due to a hard cutoff of Au plasmonic response below 700 nm. Moreover, since the 1550 nm is at a much higher power with respect to the supercontinuum, also the SHG output has higher power ($\sim 300\,\mu W$). Fig. 6-25c illustrates the spectrum of the second harmonic signal generated in this condition. The drawback with this approach is that the higher power comes at a cost of increased damage to the sample and higher noise. In fact, to achieve the appropriate driver field at the fundamental frequency, a higher power is necessary.

The alignment also requires some nuance in this condition compared to the sampling of the fundamental pulse, both for spatial and temporal overlap. When signal and driver are at the same wavelength you can just maximize the beams on a reference

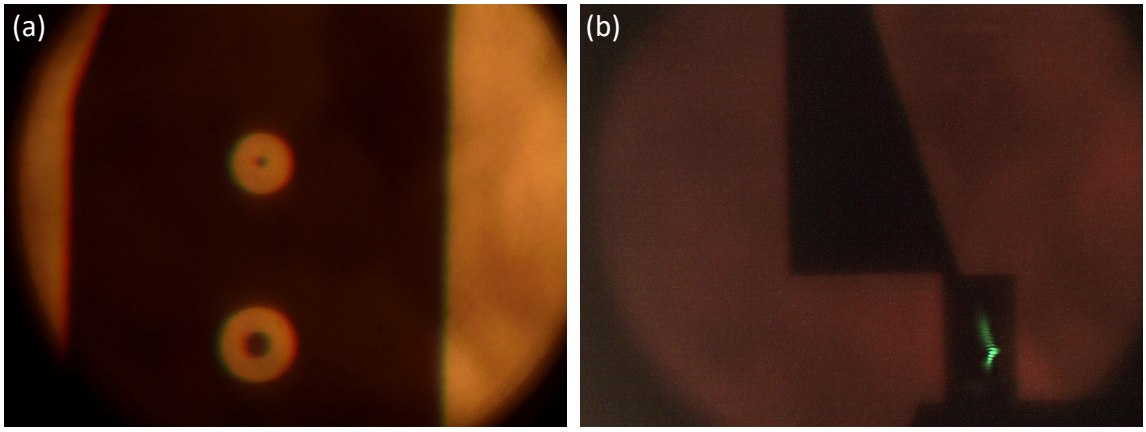

Figure 6-26: Spatial Overlap. (a) Microscope image of the donut-shaped structures nanofabricated with photolithography to align spatially the fundamental to the SHG. (b) Microscope image of the light coming from third-harmonic generation (THG) at the glass interface used to locate the fundamental beam and align it. This picture is taken with the beam on top of the nanoantennas where the field is stronger due to field enhancement. However, the THG is visible also off-sample, just more faint.

photodiode, and look at the fringes while scanning the delay. Instead, when the two wavelengths are different a different procedure is required. In this case, the alignment is performed in two steps: first, a rough alignment is done by looking at Fresnel fringes while passing through two irises using a CCD and then maximizing the beam on a power meter. Then, a fine alignment is performed at the detector plane exploiting a donut-shaped structure nanofabricated with photolithography (this is incorporated in the contact laydown step). An example of these structures is shown in Fig. 6-26 This step is performed by tuning the beam path while passing the driver and the signal through the donuts and first maximizing the intensity by looking with a CCD camera and then using a power meter(PM). It is noteworthy that while on the CCD the SHG is clearly visible, the fundamental is not. However, adjusting the focus to be exactly at the glass interface allows third-harmonic generation (THG) which can be seen on the CCD.

Regarding the temporal overlap, since the fundamental and SHG have different group velocities, the delay is going to be different with respect to the case when the signal and driver are at the same wavelength. Therefore first the two fundamentals are aligned by looking at fringes on the reference photodiode while scanning the delay.

Then, the additional delay induced by each optics element the SHG is going through is calculated. These steps ensure both spatial and temporal overlap.

Additional consideration has to be taken into account regarding the material and geometry of the nanoantennas. Gold nanoantennas of the current geometry maximize the response (i.e. the field enhancement) at the fundamental frequency, but they may in fact not be the best option to sample SHG. A material and geometry that ensures a good field enhancement both at the fundamental and second harmonic may be preferable.

Future work should include the completion of this experiment to demonstrate the sampling bandwidth of this technique. Some possible avenues that can be explored to successfully make this demonstration are: encapsulation of the devices in HSQ to reduce damage, using thicker nonlinear crystals to increase the signal, and using different nanoantenna materials (e.g. Ag) to have a bigger enhancement of the field at SHG frequencies.

6.9 Conclusion

In conclusion, planar NVC devices can be used to build detectors that enable chip-based time-domain spectroscopy up to the PHz regime, allowing the measurement of a weak, few-fJ, broadband electric field transient in the time domain. This permits the full retrieval of phase and spectral amplitude, which could be used for many applications such as the study of nonlinear phenomena in condensed matter systems and molecular fingerprinting. These detectors' geometry can also be modified to be polarization-sensitive therefore fully reconstructing the field in all its properties. These devices were also used to study the carrier dynamics of gold and preliminary work was performed to demonstrate the broadness of the bandwidth of this detection scheme.

Chapter 7

Conclusion and Outlook

In the coming years, nanoscale free-electron devices are going to play an important role in the development of innovative electronics solutions for many applications, from radiation-resistant logic, to petahertz electronics, to ultrafast metrology.

In this thesis, several aspects of the development and study of these devices were addressed, and their use for cutting-edge technological applications was discussed.

Initially, the development of a consistent fabrication process for both metallic and refractory nano vacuum channel devices was performed. The influence of several fabrication parameters and processes was studied. NVC devices reliably having sub-10 nm features were achieved.

The optimal design of such NVC devices was studied through electromagnetic and particle trajectory simulation. In particular, effort was directed toward the analysis of the influence of multiple geometrical parameters on the performance of gated NVC devices, or planar nano vacuum channel transistors (pNVCT). These devices represent the building block of any radiation-resistant logic to be developed with this technology.

The experimental characterization of the emission characteristics of planar NVC emitters was then carried out. By investigating the electrical characteristics of Au and TiN NVC devices under various temperatures and pressures, three distinct emission regimes were clearly isolated: Schottky, Fowler-Nordheim, and saturation. The long-term stability of these devices was also demonstrated[63], as well as their gated operation. The latter is the first step towards the development of useful logic. This

work will enable robust and accurate modeling of vacuum nanoelectronics which will be critical for future applications requiring high-speed and low-power electronics capable of operation in extreme conditions.[34]

Thanks to the fast switching time of NVC devices, they can be operated at optical frequencies as well as more typical electrical ones. In this thesis, the optical-electrical mixed-mode operation was studied. In particular, a careful analysis of how the synergy between the two can be exploited to operate the devices in different regimes was carried out. Using time-dependent Schrödinger equation (TDSE) simulations, it was demonstrated how the application of an external electrical bias can be used to reduce the threshold for the transition to optical-field-driven tunneling from the surface. The enhancement to the photocurrent provided by this effect allows to electronically tag fJ ultrafast pulses at room temperature. Given the sub-fs response time of NVC devices, detectors that exploit this bias-enhanced surface emission from nanoscale vacuum gaps could prove to be useful for communication, petahertz electronics, and ultrafast optical-field-resolved metrology.[64]

Finally, the use of NVC devices for on-chip petahertz processing of optical fields was investigated experimentally in the context of developing detectors that can be used to sample optical fields with sub-cycle resolution. A novel device able to sample arbitrary, low-energy, near-infrared waveform under ambient conditions with attosecond resolution was demonstrated. In this work, these nanoantenna arrays were used to sample optical pulses with energies of the order of a few fJ, 6 orders of magnitude lower than the competing state of the art.[81] An improvement to this scheme, using a device design that allows for polarization sensitivity was also demonstrated. Such arrays were then used to investigate carrier dynamics in gold. Preliminary work was also conducted to experimentally demonstrate the theoretically predicted sampling bandwidth through SHG sampling.

The work discussed in this thesis demonstrated how the interesting emission properties that arise from the miniaturization to the nanoscale and planarization of vacuum channel devices, such as high speed, stability, low power operation, and integrability can be leveraged in multifarious fields. These devices are the first step toward

the development of reliable radiation-resistant and petahertz electronics. With further development, they will be an extremely powerful tool for many applications, such as space electronics, molecular fingerprinting, and optical information processing.

Future work should include: (1) the continuation of the study of optical and electrical properties of NVC devices; (2) the optimization of existing and development of new devices for specific applications such as radiation-resistant logic; (3) CCD-like modules for field-resolved imaging application, and (4) detectors on waveguides for ultrafast communication applications. Moreover, there should be a push towards more and more integration to bring all the optics (e.g using metasurfaces) and processing into a compact module. These advancements would shape a new future in many fields such as diagnostics, imaging, communication, electronics, and much more.

Bibliography

[1] Brian Randell. Colossus: Godfather of the computer. In *The Origins of Digital Computers*, pages 349–354. Springer, 1982.

[2] Douglas Rayner Hartree. The eniac, an electronic computing machine. *Nature*, 158(4015):500–506, 1946.

[3] Jin-Woo Han, Dong-Il Moon, and M Meyyappan. Nanoscale vacuum channel transistor. *Nano letters*, 17(4):2146–2151, 2017.

[4] Giorgio Baccarani, Matthew R Wordeman, and Robert H Dennard. Generalized scaling theory and its application to a 1/4 micrometer mosfet design. *IEEE Transactions on Electron Devices*, 31(4):452–462, 1984.

[5] Harley Iams and Bernard Salzberg. The secondary emission phototube. *Proceedings of the Institute of Radio Engineers*, 23(1):55–64, 1935.

[6] Ferdinand Braun. Über ein verfahren zur demonstration und zum studium des zeitlichen verlaufes variabler ströme. *Annalen der Physik*, 296(3):552–559, 1897.

[7] AS Gilmour. *Klystrons, traveling wave tubes, magnetrons, crossed-field amplifiers, and gyrotrons*. Artech House, 2011.

[8] AAG Driskill-Smith, DG Hasko, and H Ahmed. Nanoscale field emission structures for ultra-low voltage operation at atmospheric pressure. *Applied physics letters*, 71(21):3159–3161, 1997.

[9] Georg Gaertner. Historical development and future trends of vacuum electronics. *Journal of Vacuum Science & Technology B, Nanotechnology and Microelectronics: Materials, Processing, Measurement, and Phenomena*, 30(6):060801, 2012.

[10] CA Spindt, I Brodie, L Humphrey, and ER Westerberg. Physical properties of thin-film field emission cathodes with molybdenum cones. *Journal of Applied Physics*, 47(12):5248–5263, 1976.

[11] Meng Ding, Han Kim, and Akintunde I Akinwande. Highly uniform and low turn-on voltage si field emitter arrays fabricated using chemical mechanical polishing. *IEEE Electron device letters*, 21(2):66–69, 2000.

[12] Meng Ding, Guobin Sha, and Akintunde I Akinwande. Silicon field emission arrays with atomically sharp tips: Turn-on voltage and the effect of tip radius distribution. *IEEE Transactions on Electron Devices*, 49(12):2333–2342, 2002.

[13] Wikipedia contributors. Vacuum tube — Wikipedia, the free encyclopedia, 2021. [Online; accessed 11-May-2021].

[14] Johannes Schötz, Zilong Wang, E Pisanty, M Lewenstein, Matthias F Kling, and MF Ciappina. Perspective on petahertz electronics and attosecond nanoscopy. *ACS photonics*, 6(12):3057–3069, 2019.

[15] Eleftherios Goulielmakis, Vladislav S Yakovlev, Adrian L Cavalieri, Matthias Uiberacker, Volodymyr Pervak, A Apolonski, Reinhard Kienberger, Ulf Kleineberg, and Ferenc Krausz. Attosecond control and measurement: light-wave electronics. *Science*, 317(5839):769–775, 2007.

[16] Ronald Hanson, Leo P Kouwenhoven, Jason R Petta, Seigo Tarucha, and Lieven MK Vandersypen. Spins in few-electron quantum dots. *Reviews of modern physics*, 79(4):1217, 2007.

[17] Pascale Senellart, Glenn Solomon, and Andrew White. High-performance semiconductor quantum-dot single-photon sources. *Nature nanotechnology*, 12(11):1026–1039, 2017.

[18] Aymeric Delteil, Zhe Sun, Stefan Fält, and Atac Imamoğlu. Realization of a cascaded quantum system: Heralded absorption of a single photon qubit by a single-electron charged quantum dot. *Physical review letters*, 118(17):177401, 2017.

[19] John R Schaibley, Hongyi Yu, Genevieve Clark, Pasqual Rivera, Jason S Ross, Kyle L Seyler, Wang Yao, and Xiaodong Xu. Valleytronics in 2d materials. *Nature Reviews Materials*, 1(11):1–15, 2016.

[20] Yuan Cao, Valla Fatemi, Shiang Fang, Kenji Watanabe, Takashi Taniguchi, Efthimios Kaxiras, and Pablo Jarillo-Herrero. Unconventional superconductivity in magic-angle graphene superlattices. *Nature*, 556(7699):43–50, 2018.

[21] M Zahid Hasan and Charles L Kane. Colloquium: topological insulators. *Reviews of modern physics*, 82(4):3045, 2010.

[22] Su-Yang Xu, Qiong Ma, Huitao Shen, Valla Fatemi, Sanfeng Wu, Tay-Rong Chang, Guoqing Chang, Andrés M Mier Valdivia, Ching-Kit Chan, Quinn D Gibson, et al. Electrically switchable berry curvature dipole in the monolayer topological insulator wte2. *Nature Physics*, 14(9):900–906, 2018.

[23] Peter Hommelhoff and Matthias Kling. *Attosecond nanophysics: From basic science to applications*. John Wiley & Sons, 2015.

[24] Marcello F Ciappina, José A Pérez-Hernández, Alexandra S Landsman, William A Okell, Sergey Zherebtsov, Benjamin Förg, Johannes Schötz, Lennart Seiffert, Thomas Fennel, Tahir Shaaran, et al. Attosecond physics at the nanoscale. *Reports on Progress in Physics*, 80(5):054401, 2017.

[25] Yujia Yang. *Nanostructures for vacuum optoelectronic engineering*. PhD thesis, Massachusetts Institute of Technology, 2019.

[26] Yujia Yang, Marco Turchetti, Praful Vasireddy, William P Putnam, Oliver Karnbach, Alberto Nardi, Franz X Kärtner, Karl K Berggren, and Phillip D Keathley. Light phase detection with on-chip petahertz electronic networks. *Nature communications*, 11(1):1–11, 2020.

[27] Tobias Rybka, Markus Ludwig, Michael F Schmalz, Vanessa Knittel, Daniele Brida, and Alfred Leitenstorfer. Sub-cycle optical phase control of nanotunnelling in the single-electron regime. *Nature Photonics*, 10(10):667, 2016.

[28] Nicholas A Gusken, Alberto Lauri, Yi Li, Takayuki Matsui, Brock Doiron, Ryan Bower, Anna Regoutz, Andrei Mihai, Peter K Petrov, Rupert F Oulton, et al. Tio2–x-enhanced ir hot carrier based photodetection in metal thin film–si junctions. *ACS Photonics*, 6(4):953–960, 2019.

[29] Nasim Mahmoodi, Abduljabbar I Rushdi, James Bowen, Aydin Sabouri, Carl J Anthony, Paula M Mendes, and Jon A Preece. Room temperature thermally evaporated thin au film on si suitable for application of thiol self-assembled monolayers in micro/nano-electro-mechanical-systems sensors. *Journal of Vacuum Science & Technology A: Vacuum, Surfaces, and Films*, 35(4):041514, 2017.

[30] Marco Colangelo. Development of resistor process for the fabrication of shunted superconducting nanowire single photon detectors (snspd). Master's thesis, Polytechnic University of Turin, 2017.

[31] A Nardi, M Turchetti, WA Britton, Y Chen, Y Yang, L Dal Negro, KK Berggren, and Phillip D Keathley. Nanoscale refractory doped titanium nitride field emitters. *Nanotechnology*, 32(31):315208, 2021.

[32] Alberto Nardi. Novel field emission devices for vacuum nanoelectronics and optoelectronic applications. Master's thesis, Polytechnic University of Turin, 2019.

[33] R. H. Fowler and L. Nordheim. Electron emission in intense electric fields. *Proceedings of the Royal Society of London. Series A*, 119(781):173–181, May 1928.

[34] Marco Turchetti, Yujia Yang, Mina R Bionta, Alberto Nardi, Luca Daniel, Karl K Berggren, and Phillip D Keathley. Electron emission regimes of planar nano vacuum emitters. *arXiv preprint arXiv:2201.04043*, 2022.

[35] William F Brinkman, Douglas E Haggan, and William W Troutman. A history of the invention of the transistor and where it will lead us. *IEEE Journal of Solid-State Circuits*, 32(12):1858–1865, 1997.

[36] Joe X Qiu, Baruch Levush, John Pasour, Allen Katz, Carter M Armstrong, David R Whaley, Jack Tucek, Kenneth Kreischer, and David Gallagher. Vacuum tube amplifiers. *IEEE Microwave Magazine*, 10(7):38–51, 2009.

[37] Robert S Symons. Tubes: Still vital after all these years. *IEEE Spectrum*, 35(4):52–63, 1998.

[38] Eric Barbour. The cool sound of tubes [vacuum tube musical applications]. *IEEE Spectrum*, 35(8):24–35, 1998.

[39] Jin-Woo Han, Jae Sub Oh, and M Meyyappan. Vacuum nanoelectronics: Back to the future?—gate insulated nanoscale vacuum channel transistor. *Applied Physics Letters*, 100(21):213505, 2012.

[40] CA Spindt, CE Holland, A Rosengreen, and Ivor Brodie. Field-emitter arrays for vacuum microelectronics. *IEEE Transactions on Electron Devices*, 38(10):2355–2363, 1991.

[41] Christoph Karnetzky, Philipp Zimmermann, Christopher Trummer, Carolina Duque Sierra, Martin Wörle, Reinhard Kienberger, and Alexander Holleitner. Towards femtosecond on-chip electronics based on plasmonic hot electron nano-emitters. *Nature communications*, 9(1):1–7, 2018.

[42] Ferenc Krausz and Mark I Stockman. Attosecond metrology: from electron capture to future signal processing. *Nature Photonics*, 8(3):205–213, 2014.

[43] Richard G Forbes. Development of a simple quantitative test for lack of field emission orthodoxy. *Proceedings of the Royal Society A: Mathematical, Physical and Engineering Sciences*, 469(2158):20130271, 2013.

[44] Shruti Nirantar, Taimur Ahmed, Guanghui Ren, Philipp Gutruf, Chenglong Xu, Madhu Bhaskaran, Sumeet Walia, and Sharath Sriram. Metal–air transistors: semiconductor-free field-emission air-channel nanoelectronics. *Nano letters*, 18(12):7478–7484, 2018.

[45] Lucia B De Rose, Axel Scherer, and William M Jones. Suspended nanoscale field emitter devices for high-temperature operation. *IEEE Transactions on Electron Devices*, 67(11):5125–5131, 2020.

[46] Edward Leo Murphy and RH Good Jr. Thermionic emission, field emission, and the transition region. *Physical review*, 102(6):1464, 1956.

[47] Adam M Darr, Caleb R Darr, and Allen L Garner. Theoretical assessment of transitions across thermionic, field, and space-charge-limited emission. *Physical Review Research*, 2(3):033137, 2020.

[48] J Frenkel. On pre-breakdown phenomena in insulators and electronic semiconductors. *Physical Review*, 54(8):647, 1938.

[49] Antonio Di Bartolomeo, Filippo Giubileo, Laura Iemmo, Francesco Romeo, Saverio Russo, Selim Unal, Maurizio Passacantando, Valentina Grossi, and Anna Maria Cucolo. Leakage and field emission in side-gate graphene field effect transistors. *Applied Physics Letters*, 109(2):023510, 2016.

[50] Georg Gaertner, Wolfram Knapp, and Richard G Forbes. *Modern Developments in Vacuum Electron Sources*. Springer, 2020.

[51] D Tomer, S Rajput, LJ Hudy, CH Li, and L Li. Carrier transport in reverse-biased graphene/semiconductor schottky junctions. *Applied physics letters*, 106(17):173510, 2015.

[52] A Kyritsakis and JP Xanthakis. Derivation of a generalized fowler–nordheim equation for nanoscopic field-emitters. *Proceedings of the Royal Society A: Mathematical, Physical and Engineering Sciences*, 471(2174):20140811, 2015.

[53] A Vladar and M Postek. Electron beam-induced sample contamination in the sem. *Microscopy and microanalysis*, 11(S02):764–765, 2005.

[54] Michael Huth, Fabrizio Porrati, Christian Schwalb, Marcel Winhold, Roland Sachser, Maja Dukic, Jonathan Adams, and Georg Fantner. Focused electron beam induced deposition: A perspective. *Beilstein journal of nanotechnology*, 3(1):597–619, 2012.

[55] Antonio Di Bartolomeo, Filippo Giubileo, Laura Iemmo, Francesco Romeo, Saverio Russo, Selim Unal, Maurizio Passacantando, Valentina Grossi, and Anna Maria Cucolo. Leakage and field emission in side-gate graphene field effect transistors. *Applied Physics Letters*, 109(2):023510, 2016.

[56] HM Wang, Z Zheng, YY Wang, JJ Qiu, ZB Guo, ZX Shen, and T Yu. Fabrication of graphene nanogap with crystallographically matching edges and its electron emission properties. *Applied Physics Letters*, 96(2):023106, 2010.

[57] TE Stern, BS Gossling, and Ralph Howard Fowler. Further studies in the emission of electrons from cold metals. *Proceedings of the Royal Society of London. Series A, Containing Papers of a Mathematical and Physical Character*, 124(795):699–723, 1929.

[58] Richard G Forbes. Exact analysis of surface field reduction due to field-emitted vacuum space charge, in parallel-plane geometry, using simple dimensionless equations. *Journal of Applied Physics*, 104(8):084303, 2008.

[59] Alex Rokhlenko, Kevin L Jensen, and Joel L Lebowitz. Space charge effects in field emission: One dimensional theory. *Journal of Applied Physics*, 107(1):014904, 2010.

[60] YY Lau, Youfan Liu, and RK Parker. Electron emission: From the fowler–nordheim relation to the child–langmuir law. *Physics of Plasmas*, 1(6):2082–2085, 1994.

[61] RJ Umstattd, CG Carr, CL Frenzen, JW Luginsland, and YY Lau. A simple physical derivation of child–langmuir space-charge-limited emission using vacuum capacitance. *American journal of physics*, 73(2):160–163, 2005.

[62] Ranajoy Bhattacharya, Mason Cannon, Rushmita Bhattacharjee, Girish Rughoobur, Nedeljko Karaulac, Winston Chern, Akintunde Ibitayo Akinwande, and Jim Browning. Effect of room air exposure on the field emission performance of uv light irradiated si-gated field emitter arrays. *Journal of Vacuum Science & Technology B, Nanotechnology and Microelectronics: Materials, Processing, Measurement, and Phenomena*, 40(1):010601, 2022.

[63] Ranajoy Bhattacharya, Marco Turchetti, P Donald Keathley, Karl K Berggren, and Jim Browning. Long term field emission current stability characterization of planar field emitter devices. *Journal of Vacuum Science & Technology B, Nanotechnology and Microelectronics: Materials, Processing, Measurement, and Phenomena*, 39(5):053201, 2021.

[64] Marco Turchetti, Mina R Bionta, Yujia Yang, Felix Ritzkowsky, Denis R Candido, Michael E Flatté, Karl K Berggren, and Phillip D Keathley. Impact of dc bias on weak optical-field-driven electron emission in nano-vacuum-gap detectors. *JOSA B*, 38(3):1009–1016, 2021.

[65] Michael Krüger, Markus Schenk, Michael Förster, and Peter Hommelhoff. Attosecond physics in photoemission from a metal nanotip. *Journal of Physics B: Atomic, Molecular and Optical Physics*, 45(7):074006, 2012.

[66] Agustin Schiffrin, Tim Paasch-Colberg, Nicholas Karpowicz, Vadym Apalkov, Daniel Gerster, Sascha Mühlbrandt, Michael Korbman, Joachim Reichert, Martin Schultze, Simon Holzner, et al. Optical-field-induced current in dielectrics. *Nature*, 493(7430):70–74, 2013.

[67] Boris Korzh, Qing-Yuan Zhao, Jason P Allmaras, Simone Frasca, Travis M Autry, Eric A Bersin, Andrew D Beyer, Ryan M Briggs, Bruce Bumble, Marco Colangelo, et al. Demonstration of sub-3 ps temporal resolution with a superconducting nanowire single-photon detector. *Nature Photonics*, 14(4):250–255, 2020.

[68] GN Gol'Tsman, O Okunev, G Chulkova, A Lipatov, A Semenov, K Smirnov, B Voronov, A Dzardanov, C Williams, and Roman Sobolewski. Picosecond superconducting single-photon optical detector. *Applied physics letters*, 79(6):705–707, 2001.

[69] Jacek Gosciniak and Jacob B Khurgin. On-chip ultrafast plasmonic graphene hot electron bolometric photodetector. *ACS Omega*, 2020.

[70] Philipp Zimmermann, Alexander Hotger, Noelia Fernandez, Anna Nolinder, Kai Muller, Jonathan J Finley, and Alexander W Holleitner. Toward plasmonic tunnel gaps for nanoscale photoemission currents by on-chip laser ablation. *Nano letters*, 19(2):1172–1178, 2019.

[71] Shiva Piltan and Dan Sievenpiper. Plasmonic nano-arrays for enhanced photoemission and photodetection. *JOSA B*, 35(2):208–213, 2018.

[72] Markus Ludwig, Andrey K. Kazansky, Garikoitz Aguirregabiria, Dana Codruta Marinica, Matthias Falk, Alfred Leitenstorfer, Daniele Brida, Javier Aizpurua, and Andrei G. Borisov. Active control of ultrafast electron dynamics in plasmonic gaps using an applied bias. *Phys. Rev. B*, 101:241412, Jun 2020.

[73] Péter Rácz, Zsuzsanna Pápa, István Márton, Judit Budai, Piotr Wróbel, Tomasz Stefaniuk, Christine Prietl, Joachim R Krenn, and Péter Dombi. Measurement of nanoplasmonic field enhancement with ultrafast photoemission. *Nano Letters*, 17(2):1181–1186, 2017.

[74] C. Ropers, D. R. Solli, C. P. Schulz, C. Lienau, and T. Elsaesser. Localized multiphoton emission of femtosecond electron pulses from metal nanotips. *Phys. Rev. Lett.*, 98:043907, Jan 2007.

[75] Péter Dombi, Zsuzsanna Pápa, Jan Vogelsang, Sergey V Yalunin, Murat Sivis, Georg Herink, Sascha Schäfer, Petra Groß, Claus Ropers, and Christoph Lienau. Strong-field nano-optics. *Reviews of Modern Physics*, 92(2):025003, 2020.

[76] Michael Krüger, Christoph Lemell, Georg Wachter, Joachim Burgdörfer, and Peter Hommelhoff. Attosecond physics phenomena at nanometric tips. *Journal of Physics B: Atomic, Molecular and Optical Physics*, 51(17):172001, 2018.

[77] DJ Park and YH Ahn. Ultrashort field emission in metallic nanostructures and low-dimensional carbon materials. *Advances in Physics: X*, 5(1):1726207, 2020.

[78] PD Keathley, WP Putnam, P Vasireddy, RG Hobbs, Y Yang, KK Berggren, and FX Kärtner. Vanishing carrier-envelope-phase-sensitive response in optical-field photoemission from plasmonic nanoantennas. *Nature physics*, 15(11):1128–1133, 2019.

[79] Jae Dong Lee, Youngjae Kim, and Chil-Min Kim. Model for petahertz optical memory based on a manipulation of the optical-field-induced current in dielectrics. *New Journal of Physics*, 20(9):093029, 2018.

[80] Ruisheng Wang. 3d building modeling using images and lidar: A review. *International Journal of Image and Data Fusion*, 4(4):273–292, 2013.

[81] Mina R Bionta, Felix Ritzkowsky, Marco Turchetti, Yujia Yang, Dario Cattozzo Mor, William P Putnam, Franz X Kärtner, Karl K Berggren, and Phillip D Keathley. On-chip sampling of optical fields with attosecond resolution. *Nature Photonics*, 15(6):456–460, 2021.

[82] Sergey V. Yalunin, Max Gulde, and Claus Ropers. Strong-field photoemission from surfaces: Theoretical approaches. *Physical Review B*, 84(19):195426, November 2011.

[83] Matthias Ehrhardt Xavier Antoine , Anton Arnold , Christophe Besse and Achim Schädle. A review of transparent and artificial boundary conditions techniques for linear and nonlinear Schrödinger equations. *Commun. Comput. Phys.*, 4:729–796, 2008.

[84] William P. Putnam, Richard G. Hobbs, Phillip D. Keathley, Karl K. Berggren, and Franz X. Kärtner. Optical-field-controlled photoemission from plasmonic nanoparticles. *Nature Physics*, 13(4):335–339, April 2017.

[85] Peter Hommelhoff, Catherine Kealhofer, and Mark A. Kasevich. Ultrafast electron pulses from a tungsten tip triggered by low-power femtosecond laser pulses. *Phys. Rev. Lett.*, 97:247402, Dec 2006.

[86] Peter Dombi, Anton Horl, Peter Racz, Istavan Marton, Andreas Trugler, Joachim R Krenn, and Ulrich Hohenester. Ultrafast strong-field photoemission from plasmonic nanoparticles. *Nano letters*, 13(2):674–678, 2013.

[87] Markus Schenk, Michael Krüger, and Peter Hommelhoff. Strong-Field Above-Threshold Photoemission from Sharp Metal Tips. *Physical Review Letters*, 105(25):257601, December 2010.

[88] Sharon H Chou, Johannes Voss, Igor Bargatin, Aleksandra Vojvodic, Roger T Howe, and Frank Abild-Pedersen. An orbital-overlap model for minimal work functions of cesiated metal surfaces. *Journal of Physics: Condensed Matter*, 24(44):445007, 2012.

[89] Franz AM Koeck, Robert J Nemanich, Andrada Lazea, and Ken Haenen. Thermionic electron emission from low work-function phosphorus doped diamond films. *Diamond and related materials*, 18(5-8):789–791, 2009.

[90] Masayoshi Tonouchi. Cutting-edge terahertz technology. *Nature photonics*, 1(2):97–105, 2007.

[91] Jens Neu and Charles A. Schmuttenmaer. Tutorial: An introduction to terahertz time domain spectroscopy (THz-TDS). *J. App. Phys.*, 124(23):231101, dec 2018.

[92] A Bonvalet, J Nagle, V Berger, A Migus, J-L Martin, and M Joffre. Femtosecond infrared emission resulting from coherent charge oscillations in quantum wells. *Physical review letters*, 76(23):4392, 1996.

[93] Olaf Schubert, Matthias Hohenleutner, Fabian Langer, Benedikt Urbanek, C Lange, U Huttner, D Golde, T Meier, M Kira, Stephan W Koch, et al. Sub-cycle control of terahertz high-harmonic generation by dynamical bloch oscillations. *Nature photonics*, 8(2):119–123, 2014.

[94] Claudius Riek, DV Seletskiy, Andrey S Moskalenko, JF Schmidt, Philipp Krauspe, Sebastian Eckart, Stefan Eggert, Guido Burkard, and Alfred Leitenstorfer. Direct sampling of electric-field vacuum fluctuations. *Science*, 350(6259):420–423, 2015.

[95] Ioachim Pupeza, Marinus Huber, Michael Trubetskov, Wolfgang Schweinberger, Syed A Hussain, Christina Hofer, Kilian Fritsch, Markus Poetzlberger, Lenard Vamos, Ernst Fill, et al. Field-resolved infrared spectroscopy of biological systems. *Nature*, 577(7788):52–59, 2020.

[96] Franck Lépine, Misha Y. Ivanov, and Marc J. J. Vrakking. Attosecond molecular dynamics: fact or fiction? *Nat. Photon.*, 8(3):195–204, March 2014.

[97] Martin Schultze, Elisabeth M. Bothschafter, Annkatrin Sommer, Simon Holzner, Wolfgang Schweinberger, Markus Fiess, Michael Hofstetter, Reinhard Kienberger, Vadym Apalkov, Vladislav S. Yakovlev, Mark I. Stockman, and Ferenc Krausz. Controlling dielectrics with the electric field of light. *Nature*, 493(7430):75–78, 2013.

[98] Shawn Sederberg, Dmitry Zimin, Sabine Keiber, Florian Siegrist, Michael S Wismer, Vladislav S Yakovlev, Isabella Floss, Christoph Lemell, Joachim Burgdörfer, Martin Schultze, et al. Attosecond optoelectronic field measurement in solids. *Nature communications*, 11(1):1–8, 2020.

[99] Seung Beom Park, Kyungseung Kim, Wosik Cho, Sung In Hwang, Igor Ivanov, Chang Hee Nam, and Kyung Taec Kim. Direct sampling of a light wave in air. *Optica*, 5(4):402, apr 2018.

[100] Wosik Cho, Sung In Hwang, Chang Hee Nam, Mina R. Bionta, Philippe Lassonde, Bruno E. Schmidt, Heide Ibrahim, François Légaré, and Kyung Taec Kim. Temporal characterization of femtosecond laser pulses using tunneling ionization in the UV, visible, and mid-IR ranges. *Sci. Rep.*, 9(1):16067, 2019.

[101] Sabine Keiber, Shawn Sederberg, Alexander Schwarz, Michael Trubetskov, Volodymyr Pervak, Ferenc Krausz, and Nicholas Karpowicz. Electro-optic sampling of near-infrared waveforms. *Nat. Photon.*, 10(3):159–162, 2016.

[102] J. Itatani, F. Quéré, G. L. Yudin, M. Yu. Ivanov, F. Krausz, and P. B. Corkum. Attosecond streak camera. *Phys. Rev. Lett.*, 88:173903, Apr 2002.

[103] R Kienberger, E Goulielmakis, M Uiberacker, A Baltuska, V Yakovlev, F Bammer, A Scrinzi, Th. Westerwalbesloh, U Kleineberg, U Heinzmann, M Drescher, and F Krausz. Atomic transient recorder. *Nature*, 427(6977):817–821, 2004.

[104] Giuseppe Sansone, Enrico Benedetti, Francesca Calegari, Caterina Vozzi, Lorenzo Avaldi, Roberto Flammini, Luca Poletto, P Villoresi, C Altucci, R Velotta, et al. Isolated single-cycle attosecond pulses. *Science*, 314(5798):443–446, 2006.

[105] J. Schoetz, Z. Wang, E. Pisanty, M. Lewenstein, M. F. Kling, and M. F. Ciappina. Perspective on Petahertz Electronics and Attosecond Nanoscopy. *ACS Photonics*, 6(12):3057–3069, dec 2019.

[106] Mark I. Stockman, Katrin Kneipp, Sergey I. Bozhevolnyi, Soham Saha, Aveek Dutta, Justus Ndukaife, Nathaniel Kinsey, Harsha Reddy, Urcan Guler, Vladimir M. Shalaev, Alexandra Boltasseva, Behrad Gholipour, Harish N.S. Krishnamoorthy, Kevin F. Macdonald, Cesare Soci, Nikolay I. Zheludev, Vassili Savinov, Ranjan Singh, Petra Groß, Christoph Lienau, Michal Vadai, Michelle L. Solomon, David R. Barton, Mark Lawrence, Jennifer A. Dionne, Svetlana V. Boriskina, Ruben Esteban, Javier Aizpurua, Xiang Zhang, Sui Yang, Danqing Wang, Weijia Wang, Teri W. Odom, Nicolò Accanto, Pablo M. De Roque, Ion M. Hancu, Lukasz Piatkowski, Niek F. Van Hulst, and Matthias F. Kling. Roadmap on plasmonics. *J. Opt.*, 20(4):043001, apr 2018.

[107] Markus Ludwig, Garikoitz Aguirregabiria, Felix Ritzkowsky, Tobias Rybka, Dana Codruta Marinica, Javier Aizpurua, Andrei G Borisov, Alfred Leitenstorfer, and Daniele Brida. Sub-femtosecond electron transport in a nanoscale gap. *Nature Physics*, 16(3):341–345, 2020.

[108] Michael Krüger, Markus Schenk, and Peter Hommelhoff. Attosecond control of electrons emitted from a nanoscale metal tip. *Nature*, 475(7354):78–81, 2011.

[109] Robert Gomer. *Field emission and field ionization*, volume 34. Harvard University Press Cambridge, MA, 1961.

[110] F V Bunkin and M V Fedorov. Cold Emission of Electrons from Surface of a Metal in a Strong Radiation Field. *Soviet Physics JETP*, 21(5):896–899, 1965.

[111] Nathalie Picqué and Theodor W. Hänsch. Frequency comb spectroscopy. *Nat. Photon.*, 13(3):146–157, mar 2019.

[112] Ian Coddington, William C. Swann, and Nathan R. Newbury. Coherent multiheterodyne spectroscopy using stabilized optical frequency combs. *Phys. Rev. Lett.*, 100:013902, Jan 2008.

[113] B. J. Bjork, T. Q. Bui, O. H. Heckl, P. B. Changala, B. Spaun, P. Heu, D. Follman, C. Deutsch, G. D. Cole, M. Aspelmeyer, M. Okumura, and J. Ye. Direct frequency comb measurement of OD + CO $\rightarrow$ DOCO kinetics. *Science*, 354(6311):444–448, oct 2016.

[114] William P Putnam, Phillip D Keathley, Jonathan A Cox, Andreas Liehl, Alfred Leitenstorfer, and Franz X Kärtner. Few-cycle, carrier–envelope-phase-stable laser pulses from a compact supercontinuum source. *J. Opt. Soc. Am. B*, 36(2):A93, 2019.

[115] Jonathan R. Birge, Richard Ell, and Franz X. Kärtner. Two-dimensional spectral shearing interferometry for few-cycle pulse characterization. *Opt. Lett.*, 31(13):2063, jul 2006.

[116] Jonathan R Birge, Helder M Crespo, and Franz X Kärtner. Theory and design of two-dimensional spectral shearing interferometry for few-cycle pulse measurement. *JOSA B*, 27(6):1165–1173, 2010.

[117] Chris Iaconis and Ian A Walmsley. Self-referencing spectral interferometry for measuring ultrashort optical pulses. *IEEE Journal of quantum electronics*, 35(4):501–509, 1999.

[118] Jonathan Birge. *Methods for Engineering Sub-Two-Cycle Mode-Locked Lasers*. PhD thesis, Massachusetts Institute of Technology, 2008.

[119] Andrea Schirato, Giulia Crotti, Mychel Goncalves Silva, Danielle Cristina Teles-Ferreira, Cristian Manzoni, Remo Proietti Zaccaria, Paolo Laporta, Ana Maria de Paula, Giulio Cerullo, and Giuseppe Della Valle. Ultrafast plasmonics beyond the perturbative regime: Breaking the electronic-optical dynamics correspondence. *Nano Letters*, 2022.

[120] Brock Doiron, Yi Li, Andrei P Mihai, Lesley F Cohen, Peter K Petrov, Neil M Alford, Rupert F Oulton, and Stefan A Maier. Comparison of the ultrafast hot electron dynamics of titanium nitride and gold for plasmonic applications. In *Plasmonics: Design, Materials, Fabrication, Characterization, and Applications XV*, volume 10346, page 1034604. SPIE, 2017.

[121] Nicholas A Güsken, Alberto Lauri, Yi Li, Andrea Jacassi, Takayuki Matsui, Brock Doiron, Ryan Bower, Anna Regoutz, Andrei Mihai, Peter K Petrov, et al. Ir hot carrier based photodetection in titanium nitride oxide thin film-si junctions. *MRS Advances*, 5(35-36):1843–1850, 2020.

[122] DN Nikogosyan. Beta barium borate (bbo). *Applied Physics A*, 52(6):359–368, 1991.